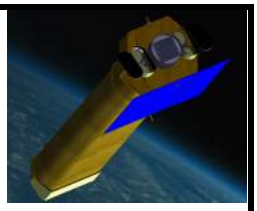

NHXM Final Auxiliary Items Phase B designs

Accordo attuativo della convenzione quadro ASI-INAF per:

"Supporto scientifico alla realizzazione della missione New Hard X-ray Mission: Fase B"

PREPARED BY:	**A. Argan**		
APPROVED BY:	**G. Tagliaferri**		
SIGNED FOR INAF-OABr	Dr. G. Tagliaferri	date:	25-08-2011

The document was edited from inputs provided by the co-authors listed in the next page

CO-AUTHORS LIST

Marco Barbera
Stefano Basso
Ronaldo Bellazzini
Valentina Bianchin
Stefano Bianchi
Luca Bombelli
Alessandro Brez
Andrea Bulgarelli
Osvaldo Catalano
Andrew Chen
Marta Civitani
Alfonso Collura
Vincenzo Cotroneo
Enrico Costa
Giancarlo Cusumano
Mauro Dadina
Fabrizio Fiore
Valentina Fioretti
Carlo Fiorini
Mauro Fiorini
Fulvio Gianotti
Miriam Giorgini
Andrea Giuliani
Fabio Gastaldello
Nicola La Palombara
Giovanni La Rosa
Giuseppe Malaguti
Giusi Micela
Teresa Mineo
Massimo Minuti
Sandro Mereghetti
Fabio Muleri
Giovanni Pareschi
Enrico Piconcelli
Michele Pinchera
Lorenzo Raimondi
Mariachiara Rossetti
Alberto Segreto
Giorgia Sironi
Paolo Soffitta
Gloria Spandre
Daniele Spiga
Elisabetta Strazzeri
Andrea Tiengo
Massimo Trifoglio
Michela Uslenghi

TABLE OF CONTENTS

CHANGE RECORDS

ISSUE	DATE	CHANGE RECORDS
1	**12/07/2010**	**First issue**
2	**21/07/2010**	**The document has been completely revised**

LIST OF ACRONYMS

AC	Anti-Coincidence
ADC	Analog-to-Digital Converter
AIT	Assembly Integration Testing
AIV	Assembly Integration Verification
AOC	Attitude and Orbit Control
APS	Active Pixel Detector
APID	APplication IDentifier
ASIC	Application-Specific Integrated Circuit
BEE	Back-End Electronics
BGO	Bismuth Germanate
CALDB	Calibration DataBase
CCOE	Central Check-Out Equipment
CE	Control Electronics
CdTe	Cadmium Telluride
CNC	Computer Numerical Control
CR	Cosmic Rays
CRC	Cyclic Redundancy Check
CsI	Cesium Iodide
CXB	Cosmic X-ray Background
DAC	Digital-to-Analog Converter
DEPFET	Deep P-type Field Effect Transistor
DP	Detector Platform
DPU	Data Processing Unit
EGSE	Electrical Ground Support Equipment
FEE	Front-End Electronics
FEM	Finite Element Method
FIFO	First In First Out
FITS	Flexible Image Transport System
FOV	Field Of View
FPA	Focal Plan Assembly
FPGA	Field-Programmable Gate Array
FWHM	Full Width at Half Maximum
GEANT	GEometry ANd Tracking
GEM	Gas Electric Multiplier
GPD	Gas Pixel Detector

GS	Ground Segment
GSE	Ground Segment Equipment
HED	High Energy detector
HEO	High Earth Orbit
HEP	High Energy Polarimeter
HEW	Half Energy Width
HK	HouseKeeping
LED	Low Energy detector
LEO	Low Earth Orbit
LEP	Low Energy Polarimeter
LVDS	Low Voltage Differential Signal
MEP	Medium Energy Polarimeter
MIP	Minimum Ionizing Particle
MDP	Minimum Detectable Polarisation
MM	Mirror Module
MOGSE	Mechanical and Optical Ground Support Equipment
NHXM	New Hard X-ray Mission
PCB	Printed Circuit Board
PIC	Polarimetric Imaging Camera
PMT	Photomultiplier Tube
PVC	PolyVinyl Chloride
QE	Quantum Efficiency
QL	Quick-Look
ROI	Region Of Interest
SDC	Science Data Centre
SEU	Single Upset Event
SGS	Science Ground Segment
SIC	Spectral-Imaging Camera
SIS	Satellite Interface Simulator
SOC	Science Operations Centre
SRAM	Static Random Access Memory
SSC	Source Sequence Counter
SVM	Service Module
TBC	To Be Confirmed
TBD	To Be Decided
TBV	To Be Verified
TBW	To Be Written
TC	Telecommand
TEC	Thermal Electric Cooler
TGSE	Thermal Ground Support Equipment

TE	Test Equipment
TM	Telemetry
ToO	Target of Opportunity
VELA	VLSI ELectronic for Astronomy
VLSI	Very-Large-Scale-Integration

REFERENCE DOCUMENTS

[RD1] Accordo attuativo della convenzione quadro per *"Supporto scientifico alla realizzazione della missione New hard X-ray Mission: Fase B"* e relativo allegato tecnico, 2009

[RD2] Costa, E., Perola, C., Puglierin, G, *Feasibility study On High Energy Astrophysics: field of interest and perspectives for the national community,* Report commissioned by ASI to the Italian Scientific Community, 2004

[RD3] Piano Aero-Spaziale Nazionale 2006-2008, ASI, 2005

[RD4] SIX-SYS-TASI-0002 issue 1, *Hexit-Sat Technical Specification,* 2008

[RD5] SIX-PLN-TASI-0002 issue *4, NHXM Preliminary Development and Model Philosophy,* 2008

[RD6] SX-TS-PR-250-JOINT issue 2.2, Simbol-X mission requirements document, 2008

[RD7] NHXM Calibration Plan, issue 1, 2011

1. Scope of the document

This document describes the architecture and design concept of Auxiliary Items foreseen in the NHXM Scientific Instrument.

It has been prepared in the context of the "Accordo Attuativo della convenzione quadro ASI-INAF per il *Supporto scientifico alla realizzazione della missione New Hard X-ray Mission: Fase B*" with the contributions of the scientific collaboration involved in the project.

This document is a deliverable of the Final Meeting foreseen by the ASI-INAF agreement.

It's worth noticing that the "Auxiliary Items" considered in the current document consists of the MMs carrying the optics, the Spectral-Imaging Cameras and the X-ray Polarimeter with the relevant Focal Plane Detectors and, in addition, it consists of all the Ground Segment tools such as the Calibration GSE and the AIV GSE which play a fundamental role in the achievement of the scientific objectives.

2. General NHXM definition

The New Hard X-ray Mission (NHXM) presented here is based on four telescopes with a focal length of 10 m, achieved after launch by means of a deployable structure (see Figure 2-1).
The four mirror modules (MM) will, for the first time, extend from 0.3 keV up to 80 keV (goal 120 keV) the fine imaging capability today available only at E<10 keV. At the focus of three telescopes there are three identical spectro-imaging cameras, at the focus of the fourth there is the polarimetric camera hosting two alternating detectors covering the range 2-35 keV. With this configuration foe the first time it is possible to obtain simultaneously images, spectral energy distributions and polarization properties (degree and angle) of sources in the X-ray sky over such a large energy range and with very good sensitivity.

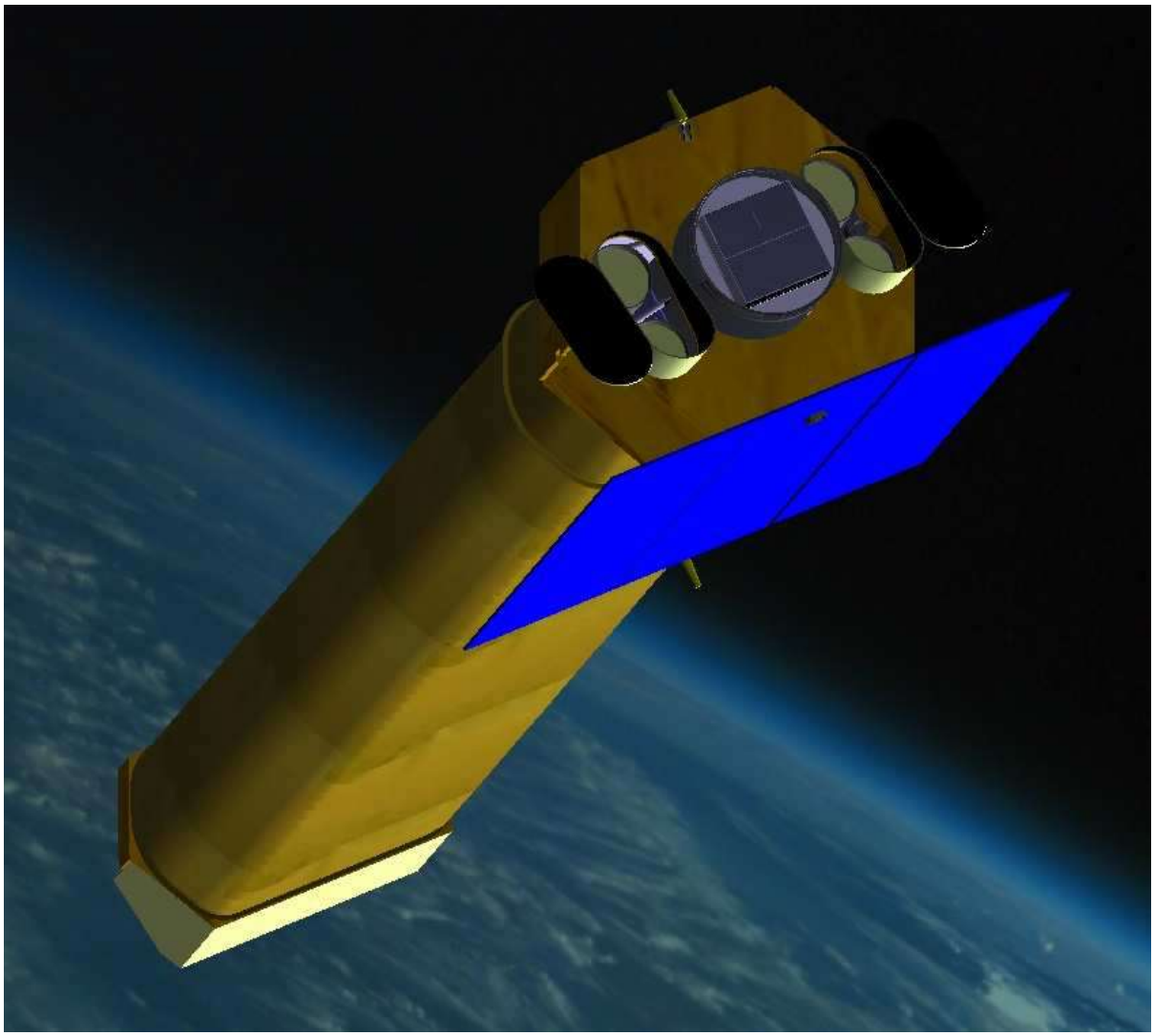

Figure 2-1: artistic view of the NHXM satellite. The four mirror modules are on the satellite platform (top right corner in this figure) and the focal plane cameras on the detector platform at the end of the deployable truss (lover left corner).

2.1 Scientific requirements

The NHXM scientific goals set the technical requirements listed in Table 2-1.

Parameter	Value
Energy band:	0.3 – 80(120 goal) keV
FOV (at 30 keV)	≥ 12 arcmin
On-axis sensitivity	≤ 10^{-14}c.g.s.(~0.5 μCrab), 10-40 keV, 3σ, 1Ms, Γ=1.6 power law spectrum
On-axis effective area	≥ 300 cm^2 at 0.5 keV ≥ 1000 cm^2 at 2-8 keV ≥ 350 (500) cm^2 at 30 keV ≥ 100 cm^2 at 70 keV ≥ 20 cm^2 at 100 keV (goal)
LED background	< 1×10^{-3} cts s^{-1} cm^{-2} keV^{-1}
HED background	< 2×10^{-4} cts s^{-1} cm^{-2} keV^{-1}
Angular resolution (HEW)	≤ 15”(10” goal) E<10 keV ≤ 20”(15” goal) E<30 keV ≤ 40” at E=60 keV (goal)
E/ΔE	40-50 at 6 keV 60 at 60 keV
Polarisation sensitivity	9.7% MDP in 100 ks for 1 mCrab (2-10 keV) & 1.8 mCrab (6-35 keV)
Wide Field X-Ray Monitor Sensitivity	2 mcrab in 50 ks at 5 σ (2-50 keV); triggering on a 0.5 crab source in 1s, providing the position in < 1min, FOV= 2.9 sr partially coded, 0.5 sr fully coded
Absolute pointing reconstruction	3” (radius 90%)
Mission duration	3 years + provision for at least 2 years extension

Table 2-1: NHXM scientific requirements

2.2 Mission profile

In the frame of the current ASI-INAF contract, the scientific Team has also responded to the ESA 2010 call for medium-size missions with a proposal developed on the wake of the NHXM mission. The main mission profile defined during the proposal preparation is also included in this document for completeness.

ThalesAleniaSpaceItaly (TAS-I) has studied with us the NHXM mission configuration, including the payload accommodation and satellite properties, in a dedicated industrial study. The NHXM satellite is made of the service module platform, accommodating the four mirrors modules, and the Instrument Platform (IP) accommodating the focal plane assembly. The IP will be put at the 10m focal length distance by a deployable truss, after the satellite is placed in orbit. Therefore, NHXM can be launched in a very compact configuration allowing for the use of a smaller fairing launcher.

The requirement of a very low and stable background count rate dictates the need for a LEO. As shown by the experience of two very successful hard-X-ray missions, BeppoSAX and Swift, a circular nearly equatorial (inclination <5°) orbit, at 600 km mean altitude with an orbital period of 95 min, guarantees a very stable and low background environment. This choice will ensure:

- remaining below the inner Van Allen radiation belt, avoiding passages within regions of trapped charged particles;
- short passages over the edge of the South Atlantic Anomaly;
- minimization of the “soft proton flares” problems, experienced by X-ray telescopes in HEO;
- ~10 min/orbit (2.5 hrs/day) visibility from an equatorial Ground Station.

Analysis of orbital perturbation (drag, gravity gradient, Sun pressure) has shown the mission feasibility at this orbit, making it optimal for the planned science.

A detailed trade-off study between scientific requirements, mass, telemetry, power budgets and launcher choice in this and previous ASI studies has shown the compatibility of the mission with the VEGA launcher (see Figure 2-2).

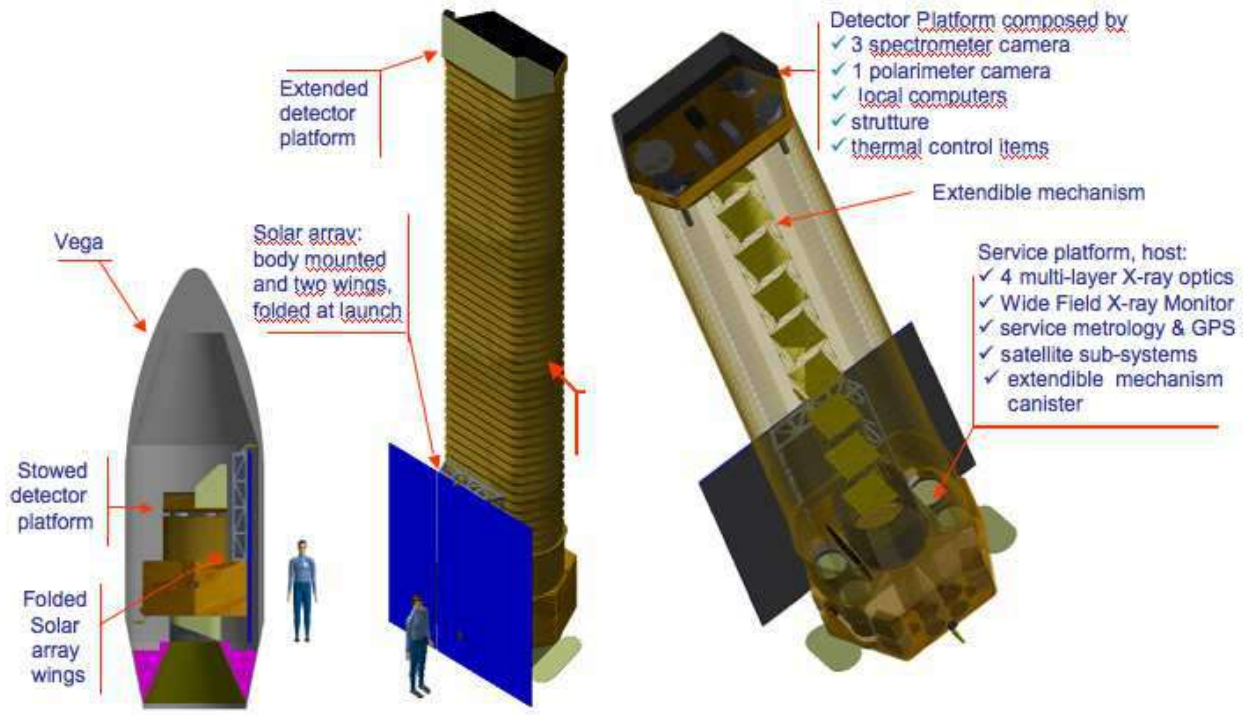

Figure 2-2: NHXM in the stowed and deployed position.

The selected orbit clearly demands an equatorial GS, for which we consider as baseline the Malindi GS (position -2.92°, 40.21°). The Kourou GS of ESA (+5.07°, 307.4°, 15 m dish) is another possibility. The use of both GS is envisaged during the launch and the early phases. The orbit and the specific GS capability permit the use of an S-Band RF link, with a telemetry down-link rate to the GS of ~2Mbps. This RF down-link rate sets the on-board data processing capability, the mass memory sizing and the observing strategy.

The payload subsystems that in principle will generate most of the telemetry are the WFXRM, if operated in "photon-mode" (i.e. the information is stored and down-linked for every single event), the polarimeters and the CCDs. For the WFXRM the data will be accumulated, analysed and compressed in "images" on board, that will be recorded every 5 minutes. The "photon-mode" acquisition will be activated for 5 minutes only on specific source triggers. A large amount of telemetry is also generated by the polarimeter when observing bright sources and downlinking all track information (see payload section). This situation can be accommodated within the downlink capability in two ways: i) by a dedicated onboard large mass memory (5 GB) and scheduling the observation of weak sources (the majority) after a bright source; ii) by onboard track reconstruction, downlinking only the main photon parameters. A similar situation applies to the CCDs, for which we will adopt the same strategy as for the polarimeters.

When a new bright source is detected by the WFXRM, its position is passed to the AOC in ≤1min and, if feasible, the satellite autonomously repoints to this target, on a time scale of ≤1 hour after the trigger. The new source will be observed for a pre-defined amount of time depending on a priority value set by the onboard software (max 10 ks, longer exposures will need human intervention). After that the satellite will return to its previous schedule. This capability, on a much more demanding scale, has already been proven by the Swift satellite. This is not our main driver, but still is one of the parameters considered in designing the mission. To maximise the observing efficiency, we will schedule 2-3 targets per orbit, selected to minimise slews.

The payload includes:

- *4 MMs with good imaging capability in the band 0.3-80 (0.3-120 goal) keV,*
- *3 MMs are coupled with 3 sensitive SICs with two detection layers each, plus an effective anticoincidence system;*
- *1 MM is coupled with two polarimetric detectors sensitive in the band 2-35 keV, composing the PIC;*
- *1 WFXRM sensitive in the 2-50 keV band to find active and transient sources.*

We used fully representative instrument responses to verify that this payload satisfies the science case. In Figure 2-3 we report the mission broadband flux sensitivity.

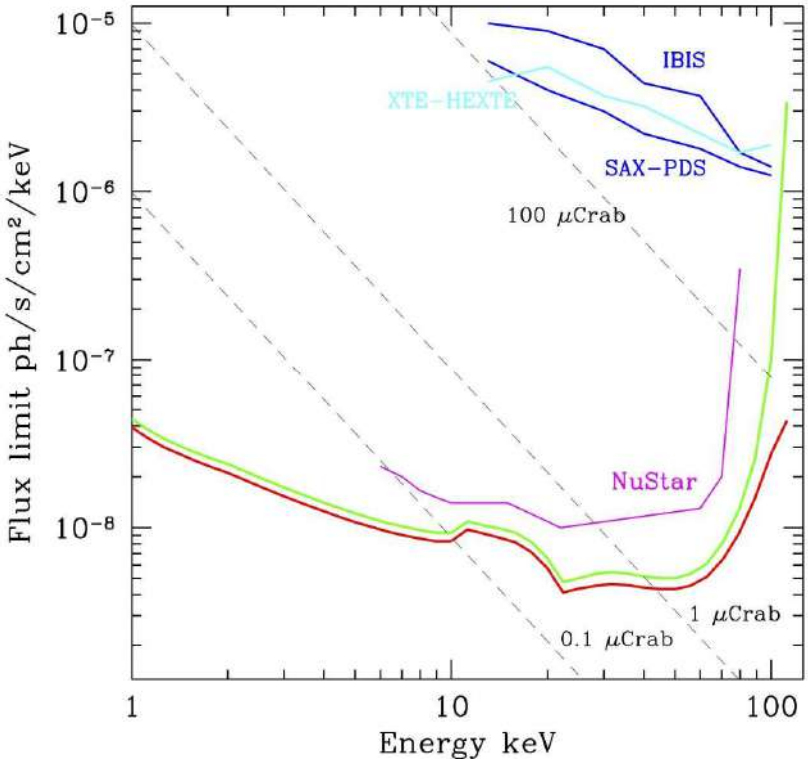

Figure 2-3: NXHM flux sensitivity

In the ESA proposal we also studied a NHXM GS system architecture and data flow, minimizing interfaces and identifying a single official SGC archive under ESA-SOC responsibility, making available all scientific NHXM data to the Guest Observers and Scientific Community at large. We include this configuration also here, noting that the role of ESA could be played by ASI in case of an ASI mission (see Figure 2-4).

We proposed a share of responsibility and interfaces between an Agency SOC and the NHXM Consortium SDC, based on the extensive expertise of NHXM Consortium members acquired in a number of past and present astronomy/astroparticle satellites (e.g. *Beppo*Sax, XMM-Newton, INTEGRAL, Swift, AGILE, Fermi, Herschel, Planck, NuSTAR, AMS and Gaia), in the field of X-ray data analysis software development, ground pipeline data processing management, mission planning support, and the essential Hardware team support for instrument calibration and monitoring.

Under the proposed share of responsibility the SOC made available in a timely manner all L0 and Auxiliary data required for the core processing to the NHXM-SDC. The satellite data are down-linked using an S-Band transponder with a downlink rate of ~2Mbps. In the hypothesis of a single Ground Station antenna, the expected maximum volume of acquired raw data is about 2.5 GB/day.

The NHXM-SDC is responsible for the scientific data processing, in-flight calibration and production of L1, L2 and L3 data products to be routinely delivered to the SOC for official archiving and distribution. The NHXM-SDC is also in charge of the Payload scientific performance and trend monitoring. The NHXM-SDC is responsible for defining and developing all the software tools for the production of the scientific data products and the CALDB. All the produced software and CALDB data are delivered to the SOC. The NHXM-SDC is also responsible for the Quick-look data analysis and scientific alert generation (ATels, GCNs).

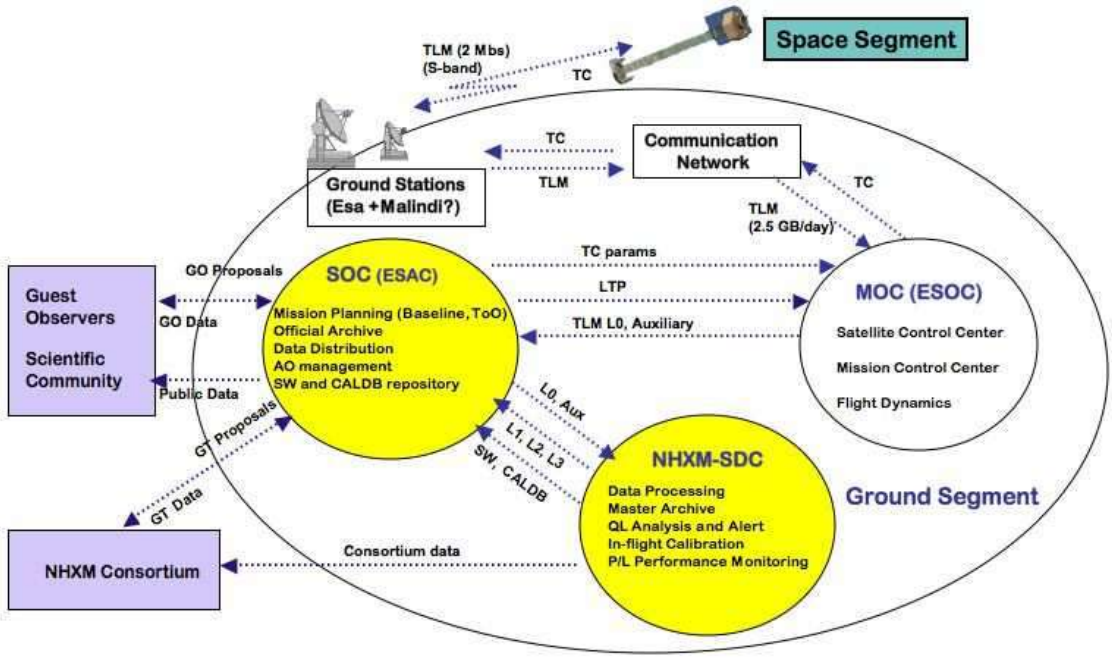

Figure 2-4: Overview of the NHXM Ground Segment architecture and data flow. In yellow: the Science Ground Segment (SGS), composed by the Science Operations Centre (SOC) and the Science Data Centre (NHXM-SDC).

SOC will be responsible for the NHXM Mission Planning (including baseline planning and ToO management), data archiving and distribution, Announcement of Opportunity management, software and CALDB repository. The NHXM Mission Consortium members, taking into account the acquired experience in past and present high-energy satellites can provide support for the scientific Mission Planning under the SOC responsibility.

3. Mirror Module

3.1 General Description

The NHXM mirrors will be electroformed NiCo shells with Wolter I profile. The adopted technology has been successfully used for the gold coated X-ray mirrors of the Beppo-SAX, XMM-Newton and Jet-X/Swift satellites (although for these mission the mirror shell were made in pure nickel (Ni), while for NHXM they will be made in a nickel-cobalt alloy, NiCo, that has better stiffness and yield properties. This technology has been developed and consolidated in the past two decades in Italy by the INAF Brera Astronomical Observatory in collaboration with the Media Lario Technology Company. For the NHXM mirrors, a few important modifications are foreseen: 1) the use of multilayer reflecting coatings, allowing us to obtain a larger FOV and an operative range up to 80 keV and beyond; 2) the NiCo walls will be a factor of two thinner than the XMM Ni-mirror shells, to maintain the weight as low as possible. With respect to the first point, once the gold-coated NiCo mirror shell has been replicated from the mandrel, the multilayer film will be sputtered on the internal surface of the shell by using a two-targets linear DC magnetron sputtering system. This process has been developed and tested for monolithic pseudo cylindrical shells at Media Lario, where a multilayer coating facility has been developed and installed as part of the Phase A contract of Simbol-X. Engineering models with two integrated shell have already been developed and tested at the Panter-MPE X-ray calibration facility. Figure 11 shows two images taken at 0.93 keV and in the band 30-50 keV. Note how the image quality is extremely good also at the higher energies. The structure of the spider arms can be seen. The HEW at 0.93 keV is about 18 arcsec, while that one at 30 keV is ~25 arcsec, not very far away from the requirements. This somewhat higher value is due to a higher mirror surface roughness, with respect to the one required by the mission.

3.2 Baseline Optical Design

The mirror module unit of the NHXM telescope comprises 4 identical modules, consisting of 70 coaxial and confocal Wolter-I mirror shells in Nickel-Cobalt electroformed alloy, with a ***10 m focal length*** and Pt/C graded multilayer coatings to extend the effective area up to 80 keV. The angular resolution of the telescope has to be better than 20 arcsec HEW for E < 30 keV. The properties of the mirror modules are hereafter reported.

- ***Mirror diameters***: the 70 shells have a *154.5 – 391 mm internal diameter* at the parabola-hyperbola intersection plane (see Figure 3-1). All diameters are reported in detail in Table 3-1.
- ***Mirror lengths***: in this baseline design, the length of the parabola equals that of the hyperbola, and is constant for all mirror shells: *300 mm for the parabola and 300 mm for the hyperbola*, for a total shell length (as measured along the optical axis) of 600 mm. This choice is motivated by the need of simplifying the manufacturing process of mandrels, mirrors, and support structures while maintaining the mutual mirror shell obstruction to a very low level (a few % at most) over the entire field of view, which has to be 12 arcmin in diameter.
- ***Incidence angles for a source on-axis***: *0.11 to 0.28 deg*, going from the innermost to the outermost shells (see also Table 3-1). They are only slightly larger than those of SIMBOL-X. The shells with the shallowest angles are devoted to the reflection of the hardest part of the X-ray band.
- ***Mirror walls thickness***: *0.13 to 0.34 mm*, going from the innermost to the outermost shells (see also Table 3-1). The mirror thickness is in a constant ratio with the shell diameters in order to endow all the shells with the same mechanical stiffness.
- ***Radial spacing of shells***: a *1.1 to 1.97 mm gap* at the intersection plane, from the smallest shells outwards. This results in a constant angular aperture of 6 arcmin, left in order to minimize the mirror shell obstruction up to a 6 arcmin off-axis., i.e., over the field of view of the mirror module. A more accurate computation (Figure 3-2) shows that this choice actually causes no vignetting up to 5 arcmin. At a 6 arcmin off-axis, the mirrors start to be vignetted, but the effective area loss due to the obstruction is only of a few %.

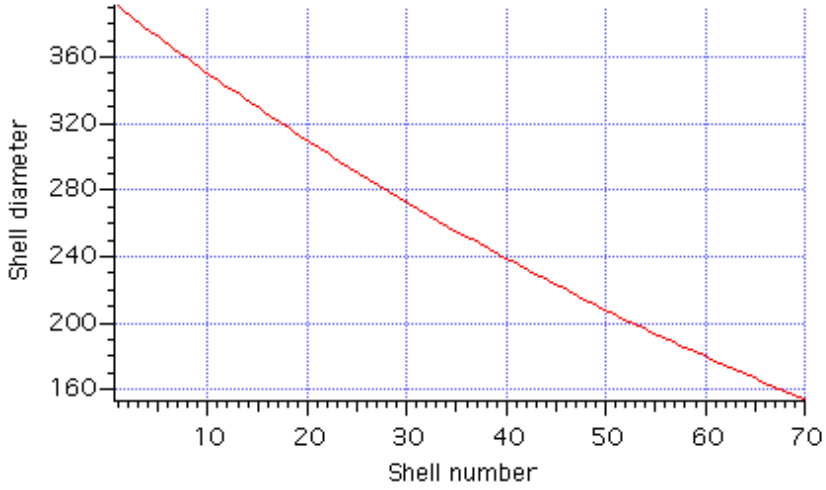

Figure 3-1: the distribution of shell diameters in each mirror module

- ***Mirror masses:*** *0.34 to 2.18 kg*, from the innermost shell to the outermost (see also Table 3-1).

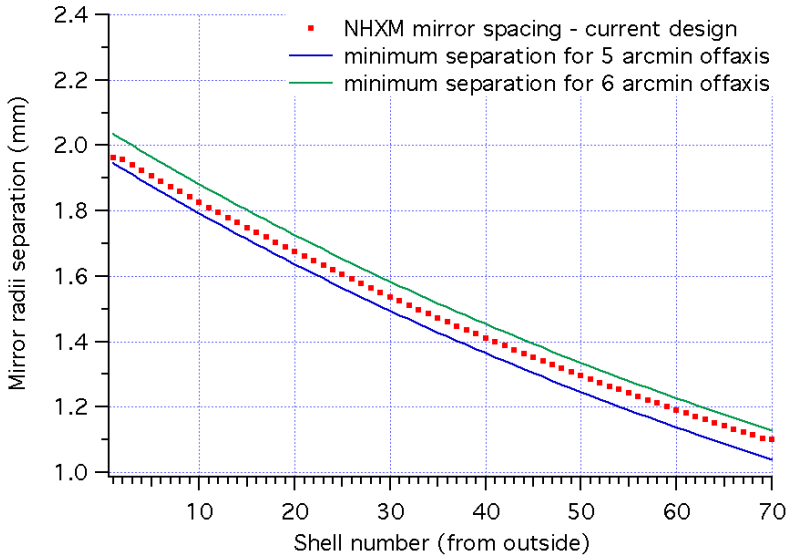

Figure 3-2: minimum spacing between the shells to avoid the mirror vignetting at 5 and 6 arcmin off-axis. The actual design falls in between of the two, but also at 6 arcmin off-axis the vignetting remains of a few percent.

- ***Spider obstruction***: *a uniform 10% effective area shading* for each mirror shells, with 18 spider spokes. This implies that the spider spokes have to be wedged, with a minimum thickness of 2.7 mm at the smallest shell diameter up to 6.8 mm at the shell with the largest diameter. This in turn determines the allocable space to settle the magnetic bars of the electron diverter without introducing further vignetting sources.

Nshell	Dmax (mm)	Dmed (mm)	Dmin (mm)	Thickness (mm)	Angle (deg)	Area (cm^2)	Mass (kg)

1	393.9	391.0	382.2	0.338	0.280	18.01	2.187
2	389.3	386.4	377.7	0.334	0.277	17.59	2.136
3	384.7	381.8	373.2	0.331	0.273	17.17	2.086
4	380.1	377.3	368.8	0.327	0.270	16.77	2.037
5	375.6	372.8	364.4	0.323	0.267	16.37	1.988
6	371.1	368.4	360.1	0.319	0.264	15.99	1.941
7	366.7	364.0	355.8	0.315	0.261	15.61	1.895
8	362.3	359.6	351.5	0.311	0.258	15.23	1.850
9	358.0	355.3	347.3	0.308	0.254	14.87	1.806
10	353.6	351.0	343.1	0.304	0.251	14.51	1.763
11	349.4	346.8	339.0	0.300	0.248	14.17	1.720
12	345.1	342.6	334.9	0.297	0.245	13.83	1.679
13	340.9	338.4	330.8	0.293	0.242	13.49	1.638
14	336.8	334.3	326.8	0.289	0.239	13.16	1.599
15	332.7	330.2	322.8	0.286	0.236	12.84	1.560
16	328.6	326.2	318.8	0.282	0.234	12.53	1.522
17	324.6	322.1	314.9	0.279	0.231	12.23	1.485
18	320.5	318.2	311.0	0.275	0.228	11.93	1.448
19	316.6	314.2	307.2	0.272	0.225	11.63	1.413
20	312.6	310.3	303.3	0.269	0.222	11.34	1.378
21	308.7	306.5	299.6	0.265	0.219	11.06	1.344
22	304.9	302.6	295.8	0.262	0.217	10.79	1.310
23	301.1	298.8	292.1	0.259	0.214	10.52	1.278
24	297.3	295.1	288.4	0.255	0.211	10.26	1.246
25	293.5	291.3	284.8	0.252	0.209	10.00	1.214
26	289.8	287.6	281.2	0.249	0.206	9.75	1.184
27	286.1	284.0	277.6	0.246	0.203	9.50	1.154
28	282.4	280.3	274.0	0.243	0.201	9.26	1.124
29	278.8	276.8	270.5	0.240	0.198	9.02	1.096
30	275.2	273.2	267.0	0.237	0.196	8.79	1.068
31	271.7	269.7	263.6	0.233	0.193	8.57	1.040
32	268.2	266.2	260.2	0.230	0.191	8.35	1.014
33	264.7	262.7	256.8	0.227	0.188	8.13	0.987
34	261.2	259.3	253.4	0.224	0.186	7.92	0.962
35	257.8	255.9	250.1	0.221	0.183	7.71	0.937
36	254.4	252.5	246.8	0.219	0.181	7.51	0.912
37	251.0	249.1	243.5	0.216	0.178	7.31	0.888
38	247.7	245.8	240.3	0.213	0.176	7.12	0.865
39	244.4	242.6	237.1	0.210	0.174	6.93	0.842
40	241.1	239.3	233.9	0.207	0.171	6.75	0.819
41	237.9	236.1	230.8	0.204	0.169	6.57	0.797
42	234.6	232.9	227.7	0.202	0.167	6.39	0.776
43	231.5	229.7	224.6	0.199	0.165	6.22	0.755

Nshell	Dmax (mm)	Dmed (mm)	Dmin (mm)	Thickness (mm)	Angle (deg)	Area (cm^2)	Mass (kg)
44	228.3	226.6	221.5	0.196	0.162	6.05	0.735
45	225.2	223.5	218.5	0.193	0.160	5.88	0.715
46	222.1	220.4	215.5	0.191	0.158	5.72	0.695
47	219.0	217.4	212.5	0.188	0.156	5.57	0.676
48	216.0	214.4	209.5	0.186	0.153	5.41	0.657
49	212.9	211.4	206.6	0.183	0.151	5.26	0.639
50	209.9	208.4	203.7	0.180	0.149	5.12	0.621
51	207.0	205.5	200.8	0.178	0.147	4.97	0.604
52	204.1	202.5	198.0	0.175	0.145	4.83	0.587
53	201.1	199.7	195.2	0.173	0.143	4.70	0.570
54	198.3	196.8	192.4	0.170	0.141	4.56	0.554
55	195.4	194.0	189.6	0.168	0.139	4.43	0.538
56	192.6	191.2	186.9	0.165	0.137	4.30	0.523
57	189.8	188.4	184.1	0.163	0.135	4.18	0.508
58	187.0	185.6	181.4	0.161	0.133	4.06	0.493
59	184.3	182.9	178.8	0.158	0.131	3.94	0.479
60	181.5	180.2	176.1	0.156	0.129	3.82	0.464
61	178.8	177.5	173.5	0.154	0.127	3.71	0.451
62	176.2	174.8	170.9	0.151	0.125	3.60	0.437
63	173.5	172.2	168.3	0.149	0.123	3.49	0.424
64	170.9	169.6	165.8	0.147	0.121	3.39	0.412
65	168.3	167.0	163.3	0.145	0.120	3.29	0.399
66	165.7	164.5	160.8	0.142	0.118	3.19	0.387
67	163.1	161.9	158.3	0.140	0.116	3.09	0.375
68	160.6	159.4	155.8	0.138	0.114	2.99	0.364
69	158.1	156.9	153.4	0.136	0.112	2.90	0.352
70	155.6	154.4	151.0	0.134	0.111	2.81	0.341

Table 3-1: properties of all mirror shells in the present design of the NHXM mirror module.

- ***Pt/C multilayer recipes:*** the multilayer coatings are of the ''graded'' type, i.e., with a variable d-spacing throughout the stack for the reflectivity to cover a wide X-ray energy band. More exactly, the d-spacing becomes thinner as one moves from the surface toward the substrate. The multilayer recipe follows the well-known trend of a power-law, d(k) = a/(b+k)c, where a,b,c, are parameters to be optimized by maximizing a given figure of merit while keeping the number of needed bilayers as low as possible. Because the reflectivity changes with the incidence angles, the multilayer recipes also vary from group to group of shells. In Table 3-2 we report the result of the opimization. The power law parameters are expressed along with the equivalent parametrization d_{min}, d_{max}, c (the power law exponent). Note that the number of required bilayers also vary in the different groups of shells.

group number	min shell No.	max shell No.	min d-spac. (Å)	max d-spac. (Å)	power-law exp.	Pt thickn. ratio	number of bilayers
1	1	8	26.53	186.17	0.161	0.42	131
2	9	17	24.68	146.69	0.223	0.42	169
3	18	25	25.05	208.97	0.197	0.4	192
4	26	34	26.68	167.29	0.191	0.43	198
5	35	42	27.87	232.95	0.192	0.43	178
6	43	50	29.42	202.55	0.192	0.38	176
7	51	58	32.81	216.98	0.187	0.37	127
8	59	65	36.45	206.75	0.185	0.37	91
9	66	70	36.82	214.99	0.189	0.39	100

Table 3-2: multilayer stack parameters optimized for groups of mirror shells.

- ***Angular degradation on defocusing***: in order to avert an angular resolution degradation, the focal lengths of all shells must coincide within ±12 mm. If the dispersion becomes large, the focal plane depth is increased, at the expensed of an increase of the HEW. Once determined the best focal plane, the detectors can be accommodated at 2 cm distance, with the best focus in the center. The HEW at the detector planes only increases of 1 arcsec, a tolerable worsening of the imaging quality. The variation of the HEW with the distance from the focal plane is displayed at 1 keV and 30 keV in Figure 3-3, under the conservative assumption that all the mirror shells have the same focal length – a situation that minimizes the focal depth.

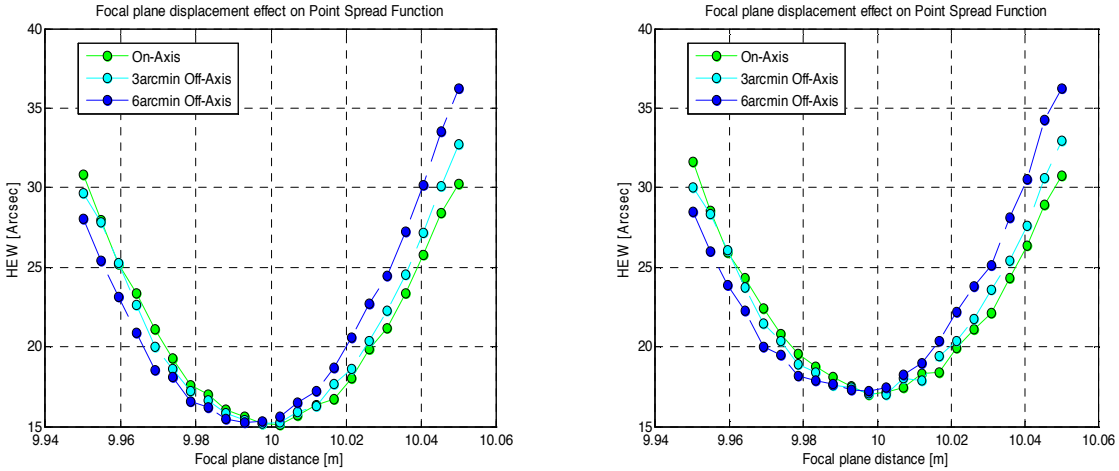

Figure 3-3: degradation of the angular resolution HEW due to the displacement of the detector from the best focal plane. (left) 1 keV and (right) 30 keV.

- ***Effective areas on-axis and off-axis:*** the effective area values up to 80 keV are computed using the reflectivity of the multilayer recipes in Table 3-2, assuming a 4 Å roughness rms, a value consistent with the roughness tolerance for the HEW increase due to X-ray scattering. The predicted effective area on-axis (Figure 3-4) fulfills the requirement of a > 1000 cm^2 at 1 keV (and even the 1500 cm^2

goal), 350 cm^2 at 30 keV and 100 cm^2 at 70 keV on-axis, with the three imaging modules. In Figure 3-4 we also plotted the effective area off-axis for a NHXM module, for an off-axis angle of 2, 4, 6 arcmin. The effective area decrease is partly due to X-rays that undergo only one reflection on the parabolic surface, partly to the variation of the multilayer reflectivity over the surface, and only to a much lesser extent to the mutual vignetting of mirror shells.

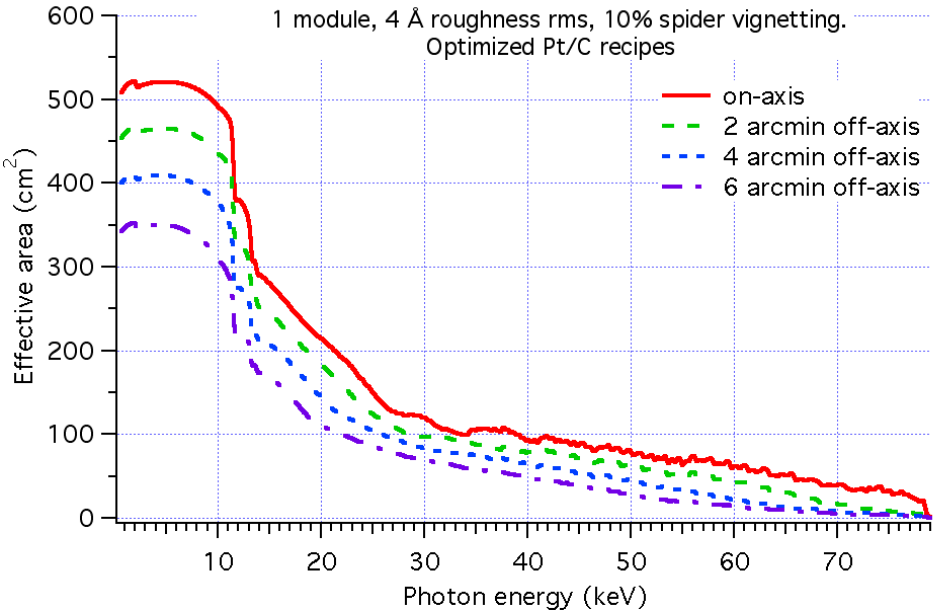

Figure 3-4: the on-axis and off-axis efective area of a NHXM mirror module.

- ***Field of view:*** from the decrease of the effective area with the off-axis angle we obtain an estimate of the field of view, i.e. the angular diameter of off-axis angles at which the effective area is halved with respect to the on-axis case. We so find a field of view > 12 arcmin up to 40 keV, and decreasing as the X-ray energy is increased: 9 arcmin at 50 keV, 4 arcmin at 70 keV.
- ***Mechanical stability:*** a Finite Element Analysis has been performed on the Mirror Module structure (Figure 3-5), which foresees, in addition to the spiders, the case and the supporting structures, an additional ring between the spider spokes to endow the system with an additional stiffness. This is necessary to bring the first resonant frequency of the system beyond 50 Hz. Adding more stiffening elements at some key location will be considered along the project development. The additional ring, nevertheless, causes a vignetting of some mirror shells, therefore we have two possibilities:

1. to suppress the few mirror shells vignetted by the ring,
2. to modulate the diameters distribution, leaving clear the area covered by the ring

The 1st solution is simpler, at the expense of some loss of effective area. If the intermediate ring is reasonably as thick at the spider at the 35th shell, it will obscure almost exactly 3 shells, with a 4% effective area loss on axis (Figure 3-6). The resulting effective area is still within the requirement.

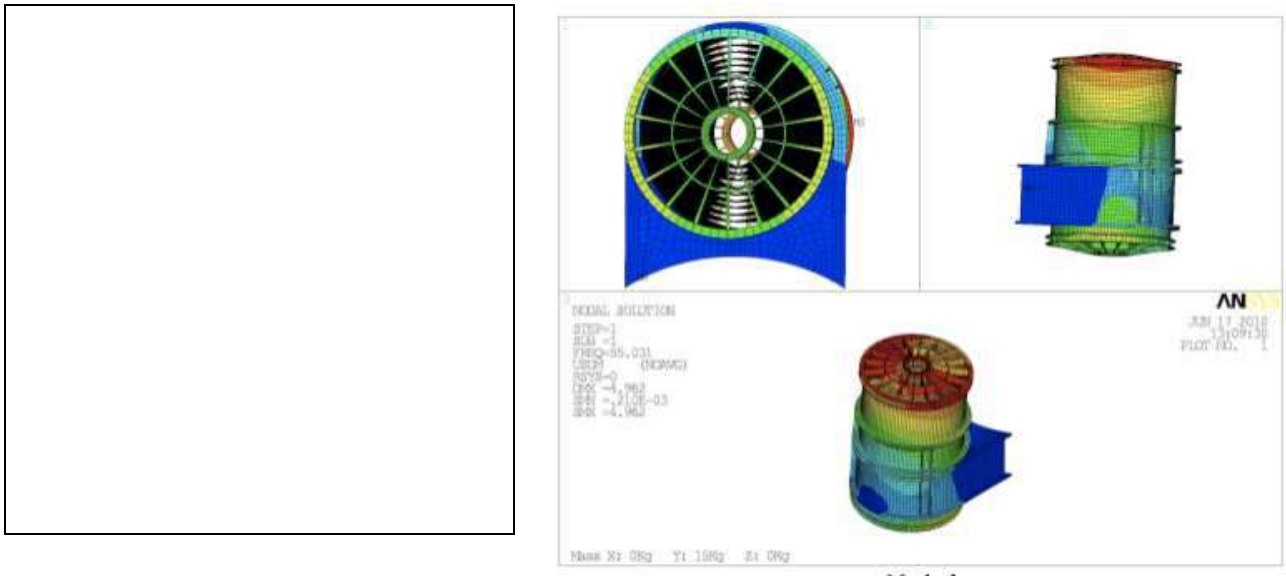

Figure 3-5: (left) the mirror module view (right) vibrational FEA simulation of the module.

The 2nd solution would allow compensating the loss of effective area on axis, but at the expense of a slight reduction of the angular aperture between shells and a consequent slight increase of the vignetting off-axis. Actually, if the ring is not too wide (e.g. 4 mm) and the diameter distribution is changed by uniformly distributing the gap required by the central ring, the effective area on-axis remains almost unchanged, while the effective area at 6 arcmin decreases only by a few percent (Figure 3-7). The second solution then seems more viable.

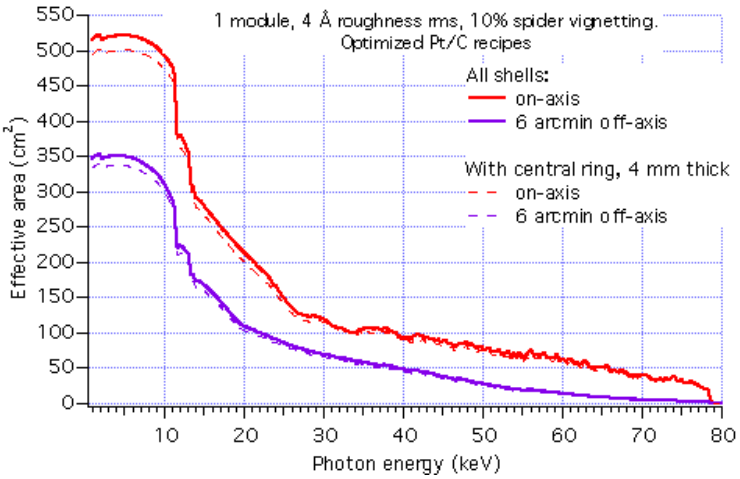

Figure 3-6: mirror vignetting introduced by the suppression of the three central vignetted shells. The effective area loss is visible at low energies, but the area is still within the specification.

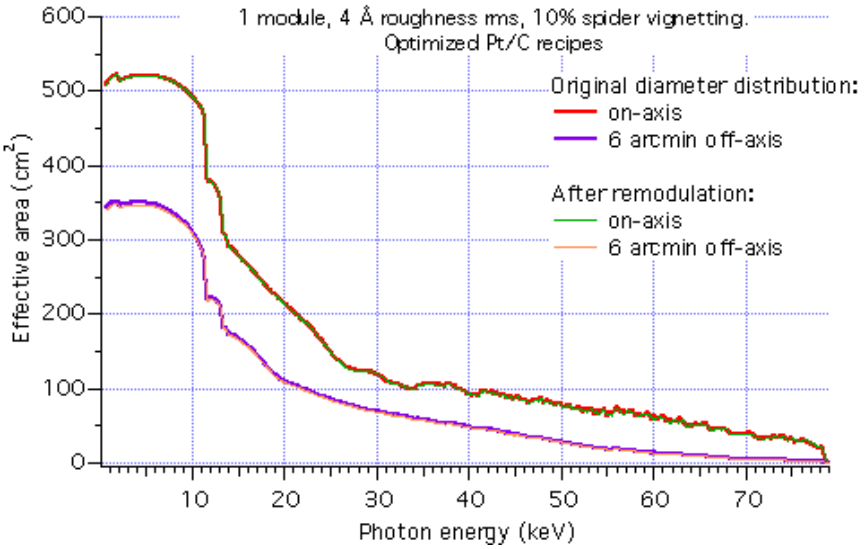

Figure 3-7: mirror vignetting introduced by remodulation of the diameter distribution to leave clear the radii covered by the central ring of the spiders.

3.3 Goal Optical Design

The goal configuration is obtained from the baseline configuration by filling the internal hole of each MM with an additional 20 mirror. The achieved effective area is shown in Figure 3-8. The additional shells will be fabricated via direct replication of multilayers (e.g. Pt/C/Ni) from TiN-coated superpolished mandrels (a technology developed at CfA in collaboration with NASA/MSFC and DTU). These shells would add 5 kg to each MM. It should be noted that the baseline presents a very good effective area in the 0.3-10 keV region (>1600 cm^2) and > 350 cm^2 at 30 keV. The FOV is >12 arcmin (50% vignetting) up to 50 keV. In the goal configuration the mirror sensitivity is extended up to 120 keV.

Nshell	Dmax (mm)	Dmed (mm)	Dmin (mm)	Thickness (mm)	Angle (deg)	Area (cm^2)	Mass (kg)
71	153.1	151.9	148.5	0.131	0.1088	2.731	0.334
72	150.6	149.5	146.1	0.129	0.1072	2.643	0.323
73	148.1	147.1	143.7	0.127	0.1053	2.558	0.313
74	145.7	144.6	141.4	0.125	0.1036	2.475	0.303
75	143.3	142.3	139.1	0.123	0.1019	2.394	0.293
76	140.9	139.9	136.7	0.121	0.1002	2.315	0.283
77	138.6	137.6	134.5	0.119	0.0986	2.239	0.274
78	136.3	135.2	132.2	0.117	0.0969	2.164	0.265
79	133.9	132.9	130.0	0.115	0.0952	2.091	0.256
80	131.6	130.7	127.7	0.113	0.0936	2.020	0.247
81	129.4	128.4	125.5	0.111	0.0920	1.951	0.239
82	127.1	126.2	123.3	0.109	0.0904	1.884	0.230
83	124.9	124.0	121.2	0.107	0.0888	1.818	0.222

84	122.7	121.8	119.0	0.105	0.0872	1.755	0.214
85	120.5	119.6	116.9	0.103	0.0857	1.693	0.207
86	118.3	117.5	114.8	0.101	0.0841	1.632	0.199
87	116.2	115.3	112.7	0.099	0.0826	1.573	0.192
88	114.1	113.2	110.7	0.098	0.0811	1.516	0.185
89	111.9	111.1	108.6	0.096	0.0796	1.461	0.178
90	109.9	109.0	106.6	0.094	0.0781	1.407	0.172

Table 3-3: properties of the additional mirror shells

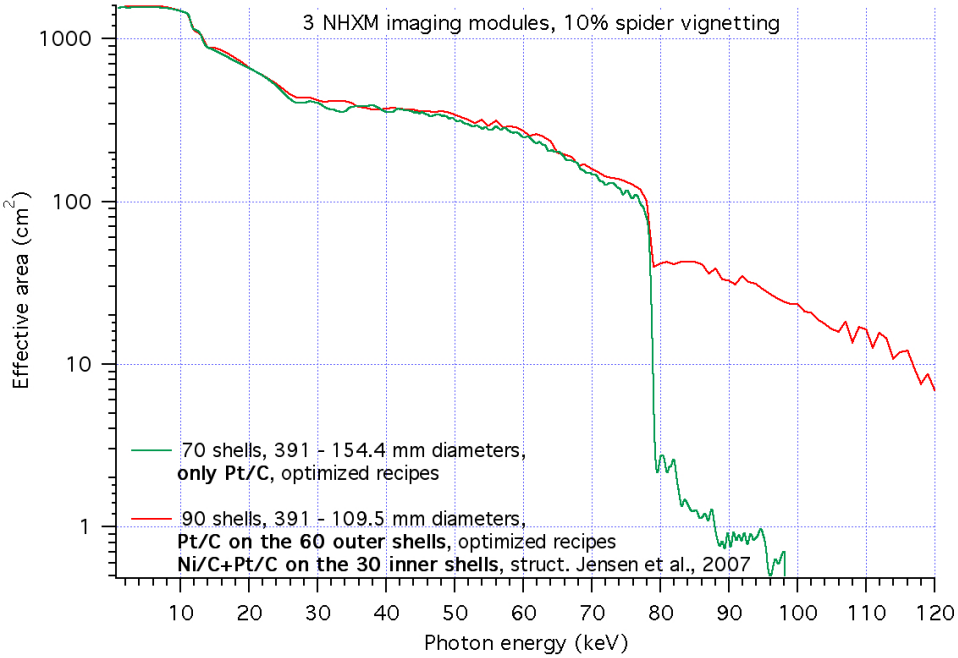

Figure 3-8: A_{eff}. (3 MM): baseline (green), goal (red).

3.4 Experimental results achieved on the optics

Test of multilayer coating performances: a number of W/Si and Pt/C multilayer coating samples (periodic, graded) were deposited onto Silicon wafer substrates and tested at INAF/OAB using the BEDE-D1 diffractometer to check their reflectivity performances in hard X-rays up to 50 keV. Most characterizations were done at the fixed energy of 8.05 keV varying the incidence angle (W/Si in Figure 3-9, Pt/C in Figure 3-10) to infer the stack structure and the roughness of the interfaces that cause the degradation of the focusing via X-ray scattering. This has been done by accurately fitting the measured X-ray reflectivity trend with a theoretical model by varying thickness, density, and roughness values until an optimal matching is reached. The results are very satisfactory since the intended multilayer recipe is accurately reproduced and the roughness value inferred from the fit (4 Å) is within the tolerances assumed to compute the theoretical effective area of the NHXM modules.

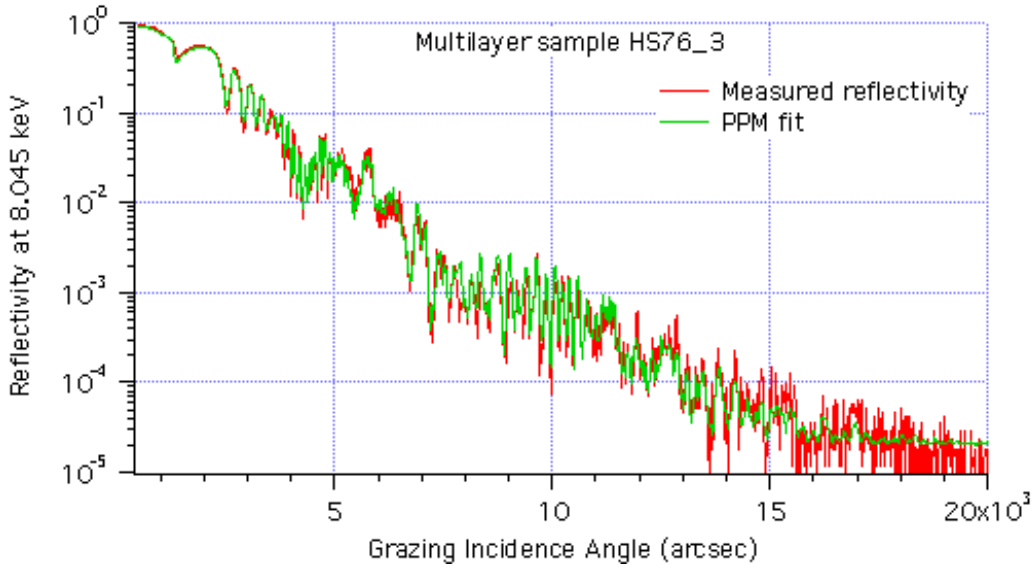

Figure 3-9: the measured reflectivity (red) of a W/Si graded multilayer sample deposited for this project. Also plotted is the reflectivity model (green), assuming a 4 Å roughness rms.

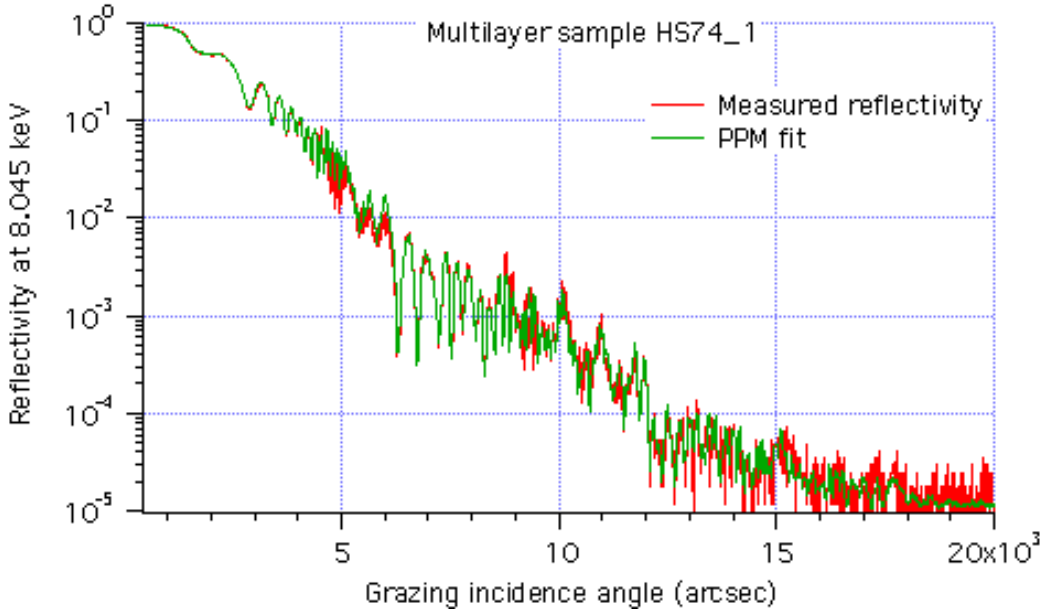

Figure 3-10: the measured reflectivity (red) of a Pt/C graded multilayer sample deposited for this project. In green we also plot the inferred reflectivity model, assuming a 4.5 Å of roughness rms.

The reflectivity performance of the multilayer coatings in hard X-rays has been also directly measured at INAF/OAB, using the same diffractometer in energy-dispersive setup. With this measurement, performed at a fixed incidence angle, it is possible to measure the reflectance of the coating at 5 to 50 keV. For both kinds of coating (W/Si in Figure 3-11 and Pt/C in Figure 3-12), the measurements are in excellent agreement with the theoretical predictions and confirm the very good interfacial smoothness of the multilayer. The measurements are performed at the incidence angles that X-ray strike the parabolic and the hyperbolic segments of mirror

shells that will be tested at PANTER. The two angles are different because of the X-ray divergence due to the finite distance of the calibration source.

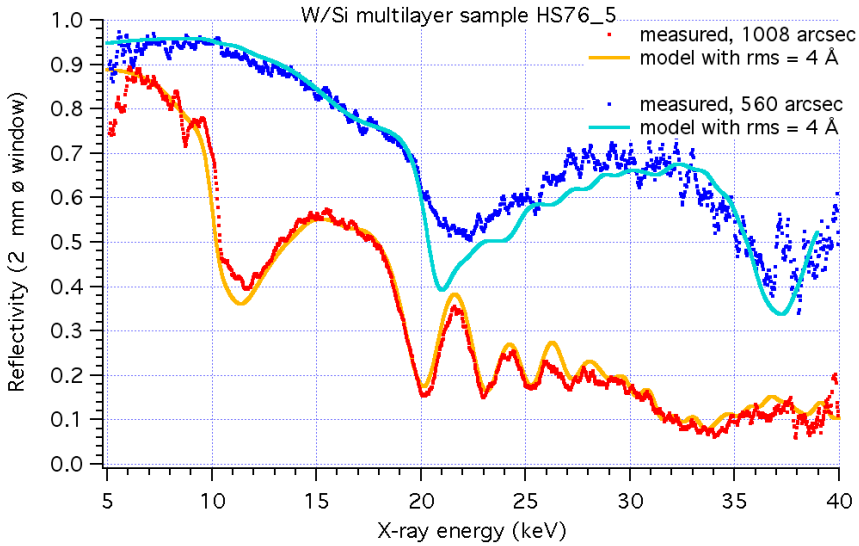

Figure 3-11: the measured reflectivity of the W/Si multilayer sample of Figure 3-10, at the two fixed incidence angles on the two surfaces of a mirror shell at PANTER, at 5 to 50 keV. Also in this case, data match a model with 4 Å of roughness rms.

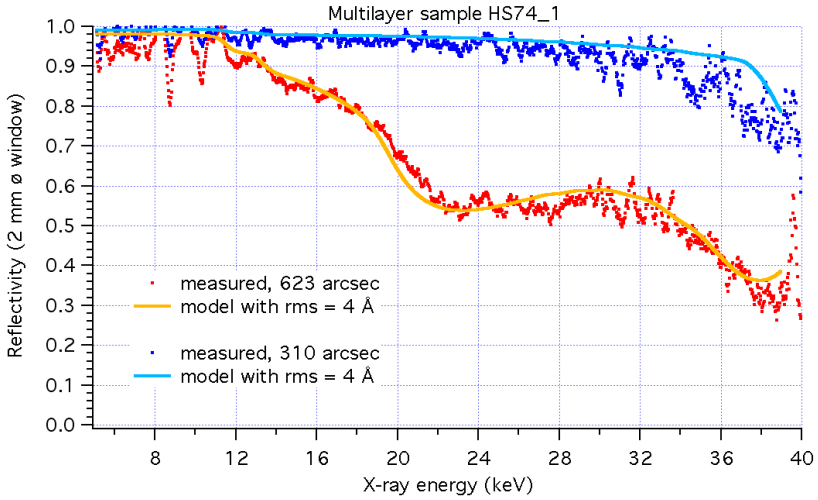

Figure 3-12: the measured reflectivity of the Pt/C multilayer sample of Figure 3-10, at the two incidence angles on the two surfaces of a mirror shell at PANTER, at 5 to 50 keV. Also in this case, data match a model with 4 Å of roughness rms.

Roughness measurements on multilayer-coated samples: samples deposited onto silicon wafer samples are very useful for stack calibration purposes and to assess the roughness intrinsically introduced by the deposition process, but the Gold substrate onto which the multilayer coating will be deposited is likely to be rougher. Since the multilayer inherits the roughness of the substrate, the coating might have a worse performance than on reflectivity calibration samples. It is therefore very important to measure the roughness of the Gold substrate,

and the roughness of the finally deposited multilayer on the mirror shell, to check its compliance with the roughness tolerances that keep the HEW degradation due to X-ray scattering within the prescribed limits. In Figure 3-13 we display some images of the surface of a W/Si graded multilayer-coated mirror shell, taken with the Atomic Force Microscope (AFM) at INAF/OAB. This mirror shell has been tested at PANTER in hard X-rays, therefore roughness can be directly correlated to the measured performances. The image on left is a 10 μm wide scan and shows a topography dominated by small peaks of a few nm height, resulting from the replication of small pores on the mandrel. The image on right shows a 2 μm wide magnification of the surface, dominated by the nanostructure of the Gold layer, entirely copied by the multilayer. The rms of the two maps are 3.6 and 1.8 Å Vs. 2.5 Å and 1.5 Å of roughness tolerance. The slight excess of roughness will be responsible for a HEW of the shell slightly exceeding the angular resolution specification in hard X-rays (< 20 arcsec below 30 keV), but still very close to it (23 arcsec at 30 keV, measured at PANTER).

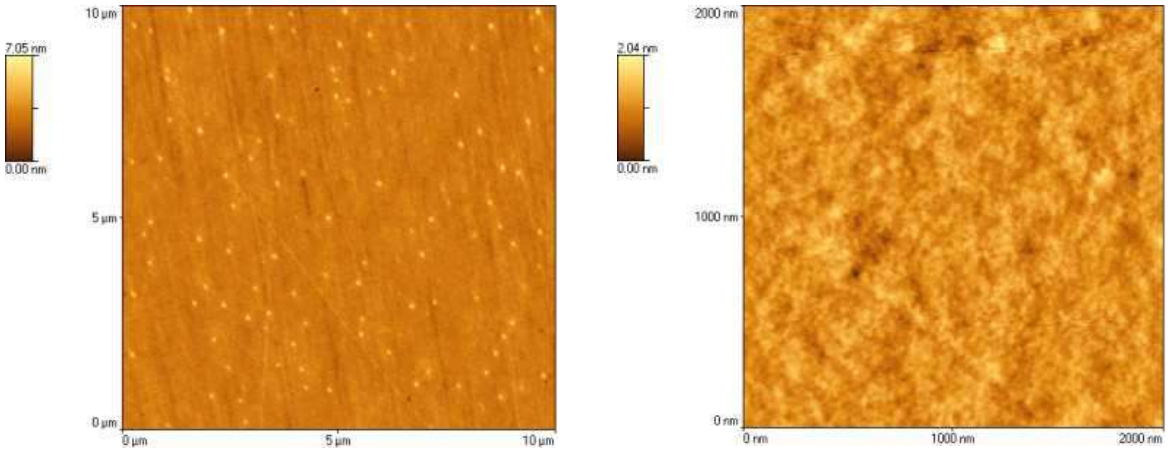

Figure 3-13: some AFM maps measured on the W/Si multilayer-coated shell tested at PANTER and Spring-8. (left) 10 µm wide scan, rms 3.6 Å. (right) 2 µm wide scan, rms 1.8 Å.

Full illumination tests at PANTER: multilayer-coated shells were tested in soft and hard X-rays to check the feasibility of a mirror shell with the thickness, focal length, diameter and length typical of the NHXM mirror shells, still maintaining a angular resolution HEW below 20 arcsec at energies below 30 keV. Tests were performed at PANTER in full-illumination setup (Figure 3-14) illuminating the mirror shell with a distant (121 m) and powerful X-ray source on-axis, and collecting the focal spot on an imaging detector. The tests were conducted in both monochromatic and energy-dispersive setup. The mirror module tested included a mirror shell with W/Si multilayer coating (the same whose AFM images are displayed at Figure 3-13). The result achieved with the TRoPIC CCD detector is shown in Figure 3-14, right. The focal spot is regular and well defined, with *a HEW of 18.5 arcsec at 1 keV and 22 arcsec in the energy band 20 – 35 keV*. This value is only slightly larger than the 20 arcsec below 30 keV prescribed for the NHXM optics, probably because of the roughness in the 10 μm range that slightly exceeded the roughness tolerance. Also off-axis measurements were conducted (Figure 3-15, left) to check the performances of the optic over the field of view. At 3 arcmin off-axis and 1 keV, the HEW is larger than the on-axis one only by a few arcsec (20 arcsec at 1 keV and 23 arcsec at 30 keV), with a focal spot still very regular and almost aberration-free. The intra-focal image off-axis (Figure 3-15, right) reveals the asymmetry in the contribution of the different sectors to the effective area, as expected from the theory. The intra-focus image highlights the roundness errors in the shell fabrication, resulting in a weakly hexagonally shaped focal spot.

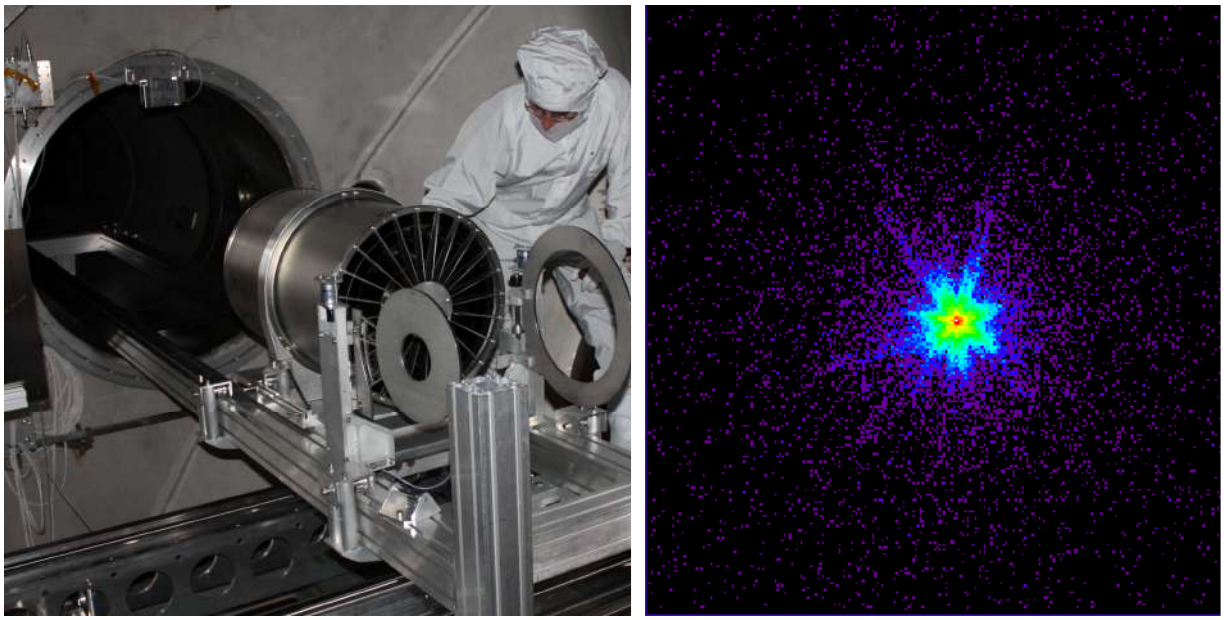

Figure 3-14: a mirror module prototype, including a W/Si multilayer-coated mirror shell, tested at PANTER. The focal spot seen in the TRoPIC CCD detector in a X-ray energy band of 20-35 keV. The HEW is 22 arcsec, very close to the specification (< 20 arcsec for E < 30 keV).

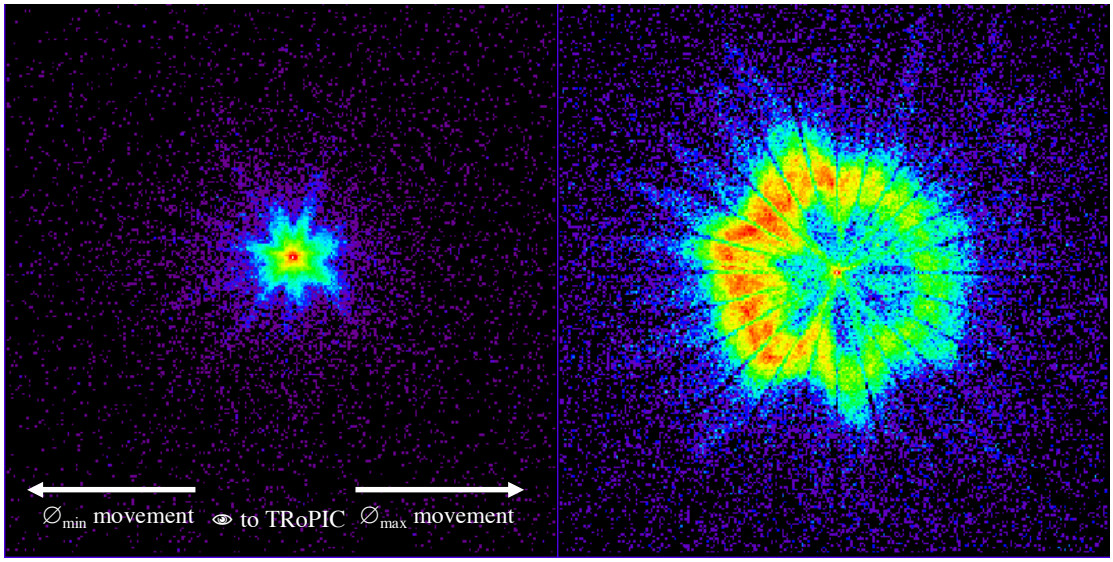

Figure 3-15: the +3 arcmin off-axis focal spot of the MS297 as seen by TRoPIC with the source at 35 kV (20 – 35 keV). (left) in focus, (right) 25 cm intra-focus. The asymmetry in the intensity distribution is not a defect; rather, it is introduced by the off-axis setting.

The HEW results are shown in detail inFigure 3-19, compared to the results achieved in pencil beam setup. The effective area values, as measured from the PSPC and TRoPIC exposures, are shown in Figure 3-16 (on axis) and in Figure 3-17 (3 arcmin off-axis). The experimental results are compared with the expected curves in the PANTER configuration of a source at 121 m distance, assuming different values of coating roughness. Note that

the effective area trends are different for the on-axis and off-axis setup (smoother for the latter), but in both cases the experiment matches the prediction very well, assuming a 4-5 Å of equivalent roughness rms, in agreement with AFM measurements (Figure 3-13). At low energies, the measurement even exceeds the prediction. Due to the finite distance of the source, vignetting effects at low energies were not detected.

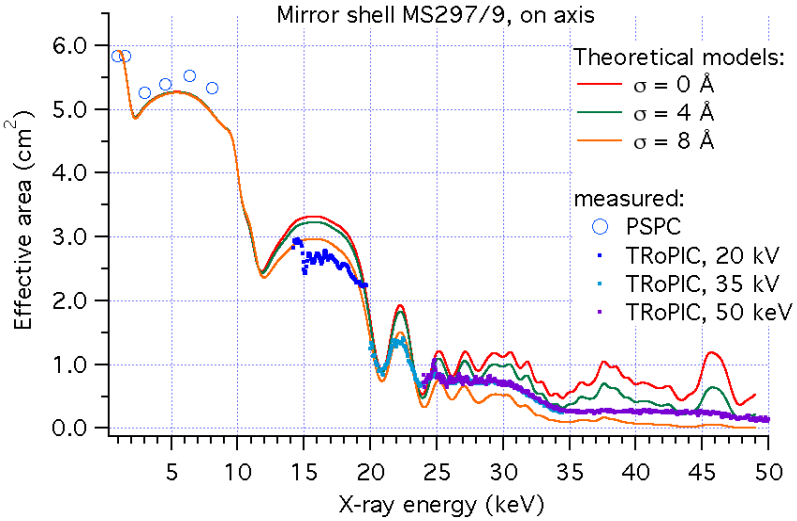

Figure 3-16: the on-axis effective areas of the MS297, as measured with the PSPC in monochromatic setup, and with TRoPIC in energy-dispersive setup.

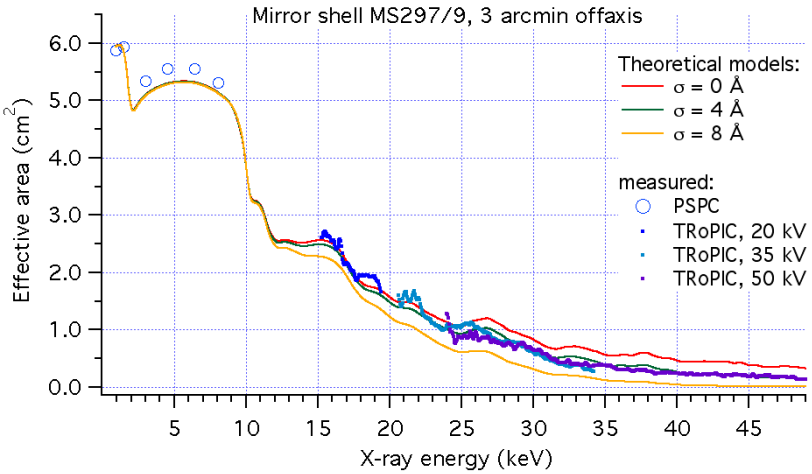

Figure 3-17: the 3 arcmin off-axis effective areas of the MS297, as measured with the PSPC in monochromatic setup, and with TRoPIC in energy dispersive setup.

Pencil-beam tests at SPring-8: the full-illumination test achieved at PANTER enables only the measurement of the angular resolution of the 50% of the effective area: in fact, because of the finite distance of the source causes the rays reflected at the front-end of the parabolic surface to miss the reflection on the hyperbola.

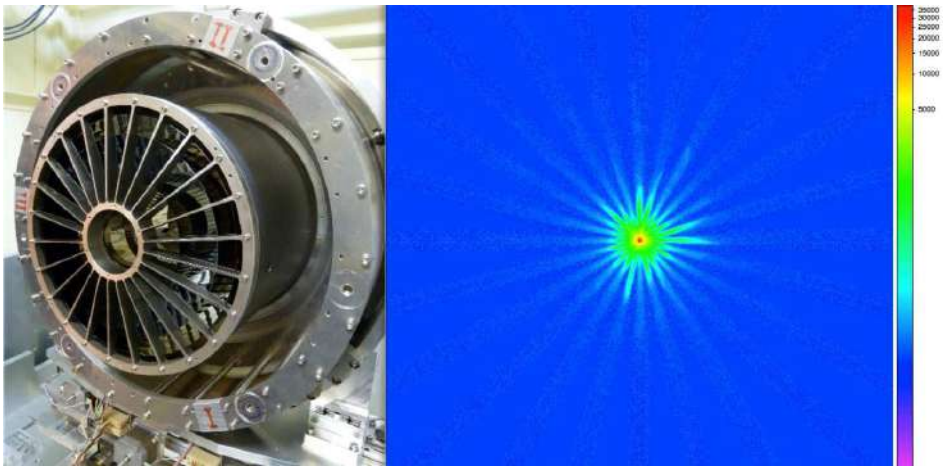

Figure 3-18: the same optical module, mounted at the X-ray synchrotron source SPring-8. The result of the reconstruction of the focal spot after exposure of all the sectors is shown. The resulting HEW is 25 arcsec, only slightly larger than the measured one at PANTER.

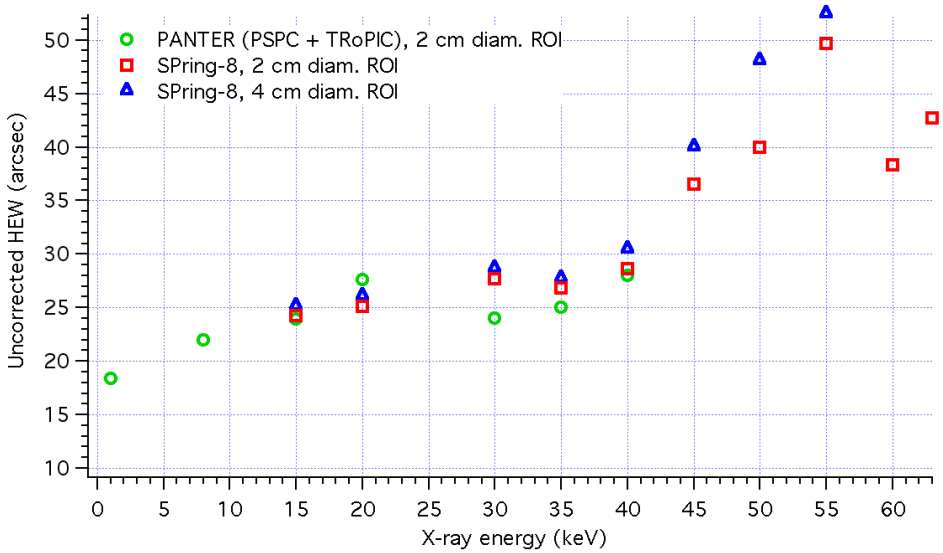

Figure 3-19: the HEW of the MS297R9, measured at PANTER and SPring-8. For the SPring-8 measurements, two ROIs were considered. The HEW, as expected, exhibits an increasing trend with the X-ray energy.

Therefore, the measurement at PANTER characterizes the entire hyperbolic surface and the half of the parabolic segment closer to the intersection plane. In order to overcome that limit, the W/Si coated mirror shell has been characterized also in pencil beam setup at the light synchrotron source SPring-8 (Japan). The setup allowed compensating for the finite distance effects by illuminating a different sector for every exposure. The focal spot was then reconstructed via software.

The reconstructed PSF is shown in Figure 3-19. The HEW at 30 keV, resulting from the reconstruction, is 26 arcsec, a bit higher than the measured result at PANTER, but still close to the specification. Moreover, it seems likely that the larger values of the HEW measured at SPring-8 are related to the different position of interference

fringes in the X-ray scattering distribution, hence they depend on the particular choice of multilayer coating in use. The HEW trend is increasing with the X-ray energy because of the X-ray scattering, as expected from the theory, and in general agreement with the one measured at PANTER. The differences may rely on the different optical quality of the first half of the parabolic mirror, which is not seen at PANTER, and on the different region of interest adopted at Spring-8, owing to the larger size of the detector.

3.5 Pre-collimator

The stray–light is the contamination by X-ray sources and/or by the diffuse X-ray background located outside the NHXM FoV (6 arcmin radius) whose light goes through the nested concentric mirrors and arrives onto the focal plane detector without undergoing the focusing double reflection (red curve in the Figure 3-20). This undesirable light light increase the background and could decrease the sensitivity of the telescope limiting its performance for very faint and/or extended sources. A careful study through a simulation code has been performed to evaluate the stray–light contamination and the eventual need of a pre-collimator.

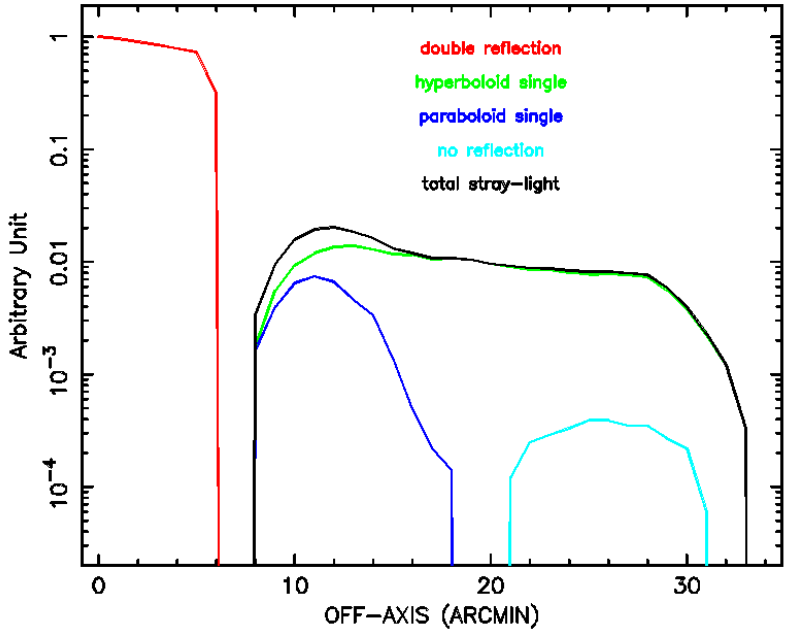

Figure 3-20: The NHXM focal plane contamination due to a point source positioned between 8-33 arcmin off-axis

The Figure 3-20 shows how a point source contaminates the NHXM focal plane if the position of this source is between 8 and 33 arcminute off-axis. Different colours refer to different components of the stray-light:

- not reflected by the inner mirror surfaces at all (direct photons, *light blue curve)*
- reflected by the paraboloid but not by the hyperboloid (single reflection, *blue curve)*
- not reflected by the paraboloid but by the hyperboloid only (single reflection, *green curve)*.

In order to reduce the stray-light we have studied the implementation of an X-ray baffle. We have optimized the

design of this baffle to maximize its efficiency to stop the stray-light and to minimize any degradation in the performance of the mirrors in terms of vignetting.

The design of the NHXM X-ray baffle follows the baseline of the one already developed for the XMM telescope. It consists of a complex X-ray baffle mounted above the entrance pupil of the telescope and accurately positioned in front of the mirrors. A sketch of the baffle design is shown in Figure 3-21. Each mirror is equipped with a concentric ring above the entrance aperture (*first sieve plate*) and a second ring (*second sieve plate*) of equal shape above the first one.

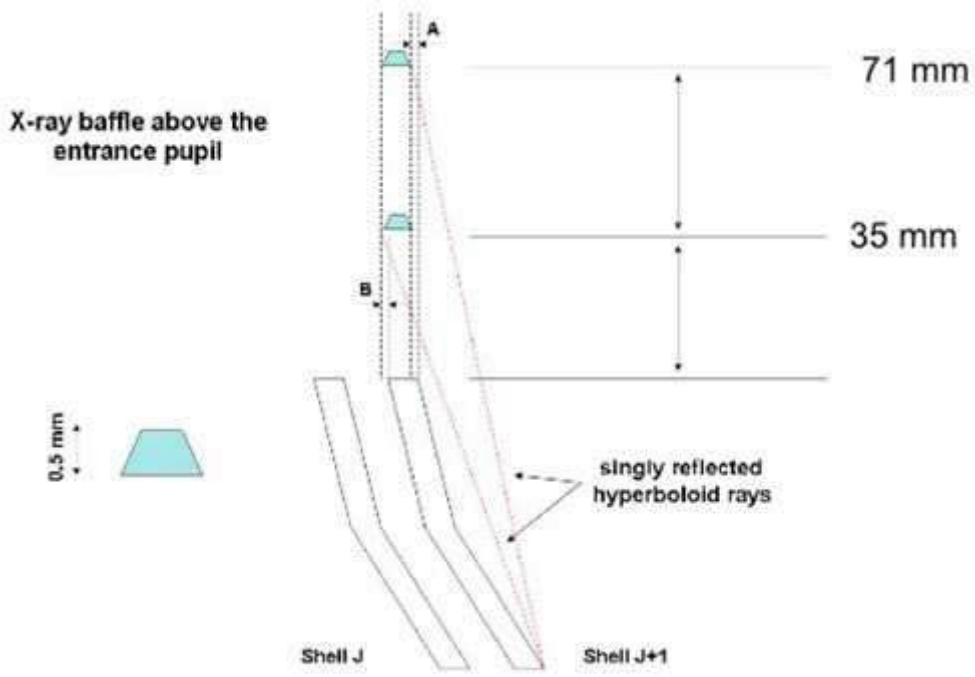

Figure 3-21: A sketch of the baffle design

The height that optimizes the stray-light suppression varies from shell to shell depending on the slope of the mirror. We adopt a design with rings mounted at the same height for all shells. The heights of the two sets of rings is therefore optimised via simulations. To prevent on-axis effective area reduction due to an unwanted stopping of double reflection rays (red curve), the inner radius of each ring will be 50 micron larger than the inner radius of the mirror. Along the optical axis direction each ring is 0.5 mm thick. The radial size of the rings varies between ~0.3 mm and ~0.1 mm while the separation between a ring and the adjacent one varies between ~2.1 mm and ~1.2 mm.

As an example we set the position of the first sieve plate 3.75 cm above the optics entrance pupil and the second sieve plate 7.1 cm above the first one. The X-ray baffle capability to block the stray-light is shown in Figure 3-22 (dashed lines represent the stray-light components with the implementation of the baffle precollimator).

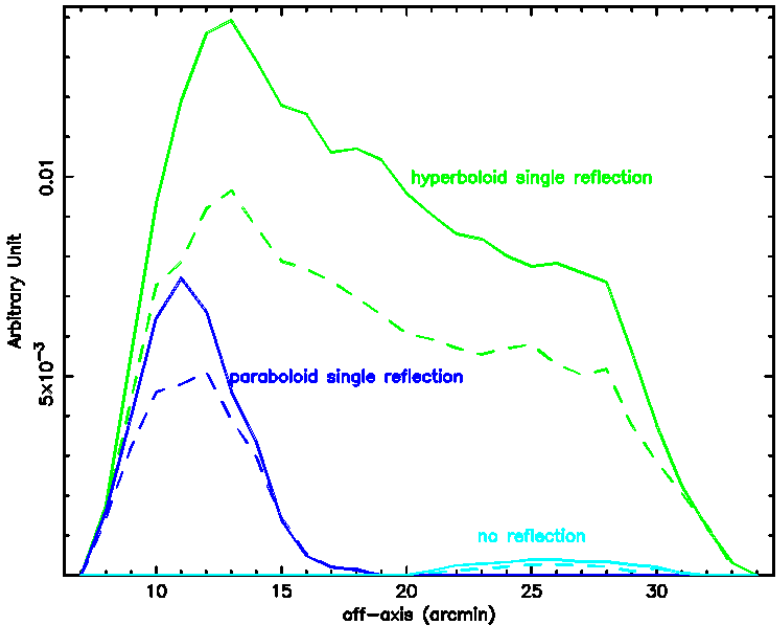

Figure 3-22: The X-ray baffle capability to block the stray-light (dashed lines represent the stray-light components with the implementation of the baffle precollimator

The stray-light stopping efficiency could increase by a factor of 2-3 by optimizing the position of the two sieve plates above the optics entrance pupil.

To evaluate the stray-light contamination due to the diffuse X-ray background we consider the model reported by Gruber, D. E., Matteson, J. L., Peterson, L. E., & Jung, G. V. (*Ap. J.* 520 124 1999). The optimized precollimator design is able to produce a 50% reduction of this background. Figure 3-23 compares the background expected from stray-light without the baffle implementation (column 3) and with the implementation of the precollimator design.

Energy (keV)	No Baffle Stray-light (count s^{-1} cm^{-2} keV^{-1})	Baffle Stray-light (count s^{-1} cm^{-2} keV^{-1})
LED		
0.5-3	6.9×10^{-4}	3.8×10^{-4}
3-5	1.7×10^{-4}	8.4×10^{-5}
5-10	6.9×10^{-5}	3.3×10^{-5}
10-15	2.1×10^{-5}	9.7×10^{-6}
0.5-15	1.7×10^{-4}	9.2×10^{-5}
HED		
10-25	1.1×10^{-5}	5.0×10^{-6}
25-35	2.3×10^{-6}	9.6×10^{-7}
35-70	4.6×10^{-7}	3.2×10^{-7}
5-70	8.3×10^{-6}	4.2×10^{-6}

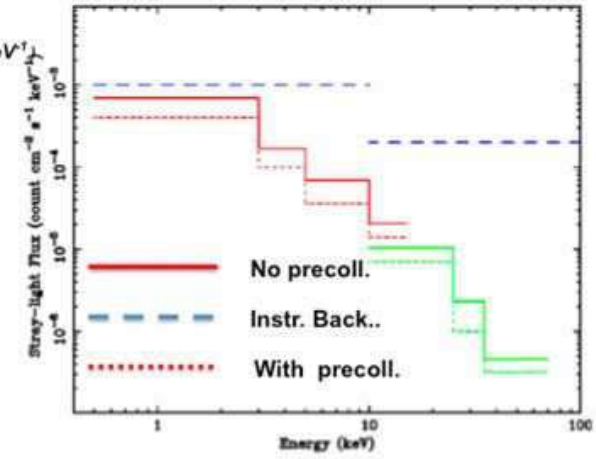

Figure 3-23: Raytracing simulation results.

As can be seen the pre-collimator is quite effective in reducing the background at low energies, but above ~10 keV its contribution to lowering the background is not very important. Therefore given the added complexity of its implementation, in the baseline configuration we do not foresee to implement pre-collimators in front of the NHXM mirrors.

3.6 Thermal blancket

Although the thermal models show that it is possible to maintain the telescope module in the required temperature range without using thermal shields, up to 70% more heating power is necessary in this case. Considering that this power is a significant fraction (up to 60% with no shields) of the total power budget of the mission, the usage of thermal shields is in fact highly desirable.

Since the deployable will be “enwrapped” by a thermally insulating bellows, it is sufficient to place one thermal shield at the front entrance of each telescope. It will also protect the mirrors and the focal plane assembly from contamination, allowing using the detectors in the “open” position, i.e. with no further filters.

The thermal shield baseline design consists of a thin plastic film coated by an “evaporated on” layer of aluminum. The plastic choosen is polyimide, a mechanically strong polymer widely tested in previous X-ray missions offering good X-ray transparency and UV rejection at wavelengths > 3500 Å.

As shown in Figure 3-24, IR radiation at 10μ (≈20 C blackbody) is efficiently reflected (>95%) by a 10-Å layer of Al. However at least 100 Å are necessary to ensure deposition uniformity.

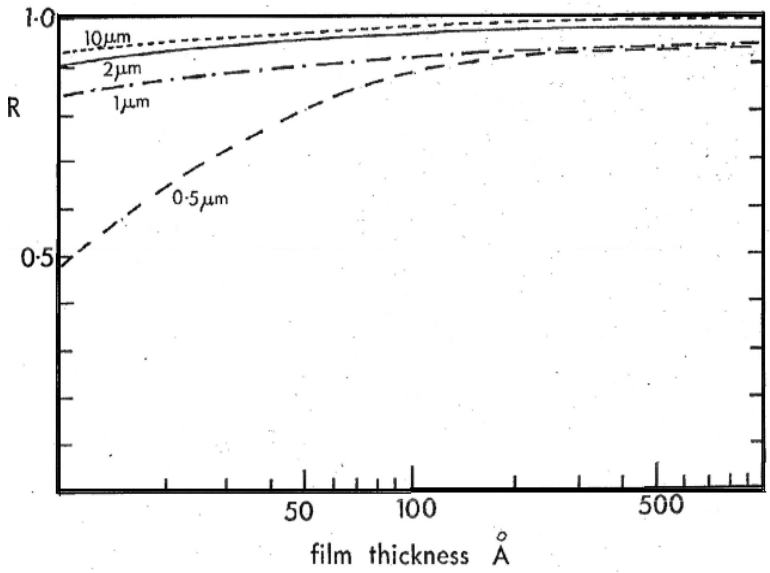

Figure 3-24: Reflection coefficient of Aluminum as a function of the film thickness at various IR wavelengths.

Figure 3-25 shows the X-ray transmission (panel a) and the UV transmission (panel b) of a thermal shield with 2000 Å of polyimide coated by 100 Å of Al. The thickness of the Polyimide has been chosen on the basis of previous space experience (namely XMM-Newton) and taking into account the size of each of the subcells in which the shield will presumably be divided. It is however necessary to make mechanical, acoustic and vibrational tests to ensure surviving to launch shocks.

It should be noted that the proposed design is meant to ensure thermal shielding maximizing X-ray transparency. This is the best choice if a filter wheel will be available at the focal plane instrumentation. If for any reason the filter wheel will not be adopted, the thickness of Al and Polyimide must be increased in order to improve the UV/Visible light rejection.

Figure 3-26 shows X-ray (panel a) and UV (panel b) transparency of a thermal shield with 4000 Å Polyimide and 1000 Å Al. A possible compromise solution with no filter wheel and gives an indication of what would be the behavior of a 2000Å Poly + 100Å Al thermal shield plus a 2000Å poly + 900Å Al filter at the focal plane.

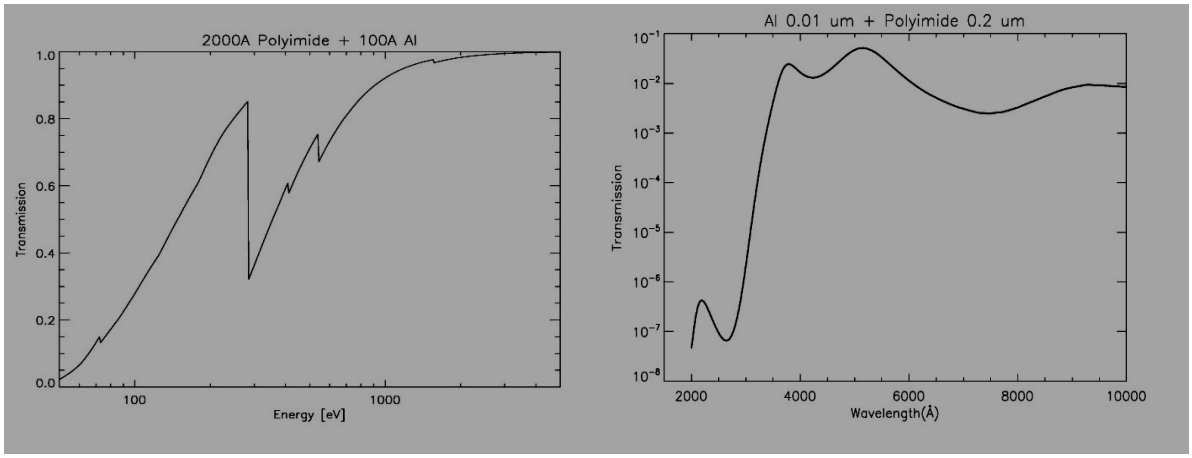

(a) (b)

Figure 3-25: X-ray transparency (panel a) and UV transparency (b) of the baseline design (2000 Å Polyimide+100Å Al) thermal shield

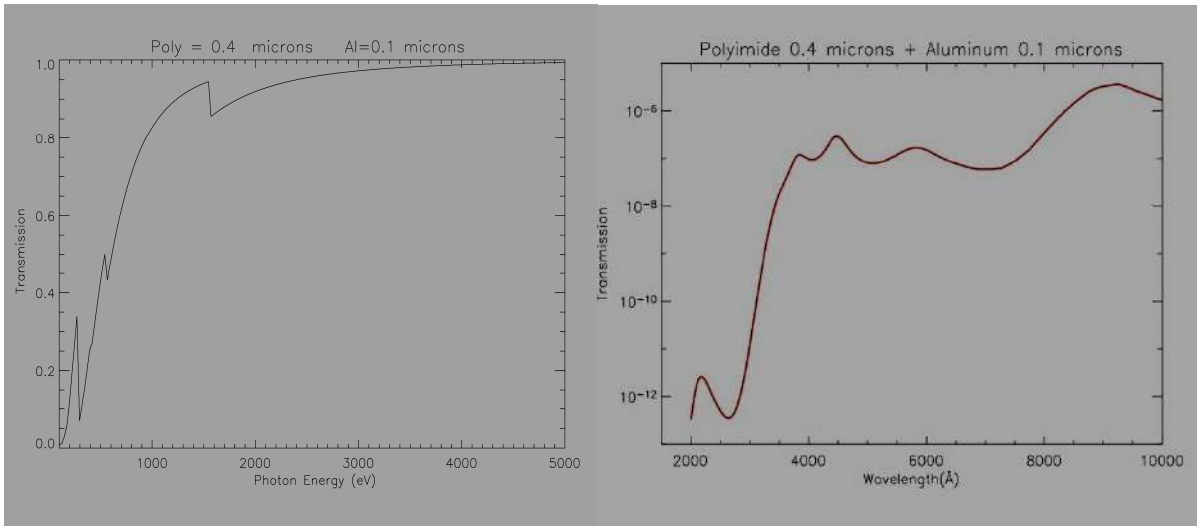

(a) (b)

Figure 3-26: X-ray transparency (panel a) and UV transparency (b) of a thicker thermal shield (4000 Å Polyimide+1000Å Al)

3.7 Magnetic Diverter

The presence of charged particles and their contribution to the background of focusing X-ray telescopes are a well-known issue. For the LEO orbit of NHXM, it is the electron background that has to be effectively prevent from reaching the detectors, because protons are trapped by the Earth radiation belts. Because electrons are 2000 times lighter than protons, it is not necessary to develop a magnetic diverter with a field as strong as that of SIMBOL-X. A possible design consist in aligning 3 magnetic bars on a radial structure that mimics the spider spokes to avoid mirror vignettings, with an increasing thickness of 2, 4, and 5 mm moving outwards. The height

of the magnets is 3 cm and their radial width is 3.5 cm, leaving 1 cm clear in between for fixtures, that have to hold firmly the magnets to avoid breakings or – even worse – the sticking of pieces of magnets to the mirrors. The safest solution seems to be inserting the magnetic bars inside the bulk of the radial structure at a 10 cm distance – at least -from the minimum diameter of the mirror shells. The magnets are aligned with centers at 9.5, 14 and 18.5 cm from the optical axis, and in order to provide a sufficiently intense magnetic field, they are in a Neodymium-Boron-Iron alloy (magnetization ~ 1.36 T), with the magnetic moments in the azimuthal direction. The resulting azimuthal field is effective in directing electrons outwards, as can be seen from a Montecarlo simulation (Figure 3-27).

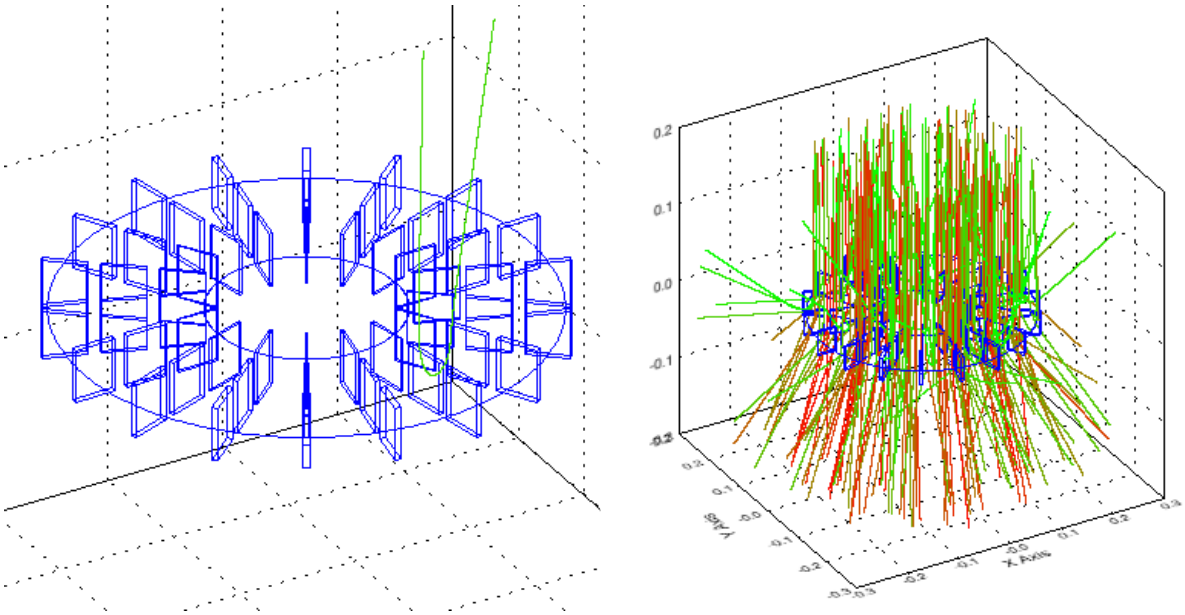

Figure 3-27: (left) structure of the electron diverter of NHXM. The Z scale is stretched. (right) action simulation of the electron diverter on an electron beam of 10 keV to 2 MeV kinetic energies, at the optic exit. No electron reached the detector. The softer electron trajectories are in green, in red we represent the trajectories of the electrons with higher Energy.

3.8 Interfaces

3.8.1 Mechanical Interface

The mass budgets for the baseline configuration and the goal configuration are summarized in Table 3-4 and Table 3-5.

Table 3-4: Baseline configuration: mass budget for a single MM.

ITEM	***Mass [kg]***
Spiders	13.43
Case	14.89
Mirror shells	73.03
X-ray pre-collimator	10.00
Magnetic diverter	5.00
Baffle/thermal cover	5.00
Adapter	4.03
Bolts & rivets	2.00
GRAND TOTAL	**127.38**

Table 3-5: Goal configuration: mass budget for a single MM.

ITEM	***Mass [kg]***
Spiders	13.43
Case	14.89
Mirror shells	78.00
X-ray pre-collimator	10.00
Magnetic diverter	5.00
Baffle/thermal cover	5.00
Adapter	4.03
Bolts & rivets	2.00
GRAND TOTAL	**132,38**

3.8.2 Thermal Interface

The Mirror Modules temperature must be stabilised within 1 °C along the radius and 2 °C along the shells.

4. Spectral-Imaging Camera

4.1 General Description

With the name Spectral-Imaging Camera (SIC) we intend one of the three identical detection units foreseen for the NHXM mission. In order to match the energy range covered by the mirror module (0.2 - 80 keV), the SIC must be able to cover this wide energy band with high detection efficiency. This is obtained by combining a fully depleted Active Pixel Detector (APS) and a CdTe (Cadmium Telluride) pixel detector stacked in a way that soft X-rays are absorbed in the APS while hard X-rays passing though the APS are absorbed in the CdTe crystal, as schematically depicted in Figure 4-1.The distance between the two detectors is set so that the optics focal plane lies halfway between the detectors. A large number of other components are assembled inside the SIC. These components need to be enclosed in a special housing or mechanical cage. The mechanical cage is designed to accommodate the LED and the HED detectors, the active and passive shielding, the thermal connections, the vacuum system and it is interfaced to a filter wheel and a collimator. The SIC, moreover, is electrically and mechanically interfaced to the LED Back-End electronics and to the HED Back-End electronics, that are outside the main body of the SIC, and finally interfaced to the satellite Detector Platform. During this study two alternative SIC configurations have been considered.

4.2 SIC first configuration

Figure 4-2 shows the preliminary conceptual sketch of the SIC. This configuration has been preferred because conjugates scientific and practical design requirements.

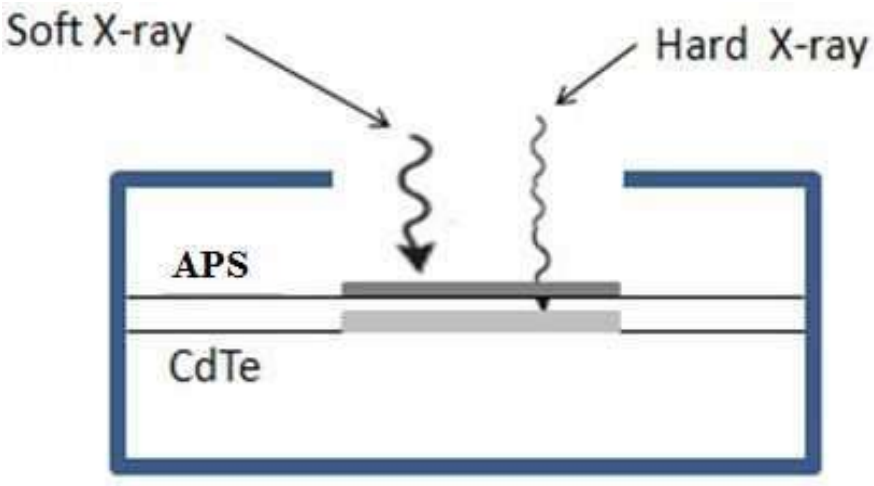

Figure 4-1: APS – CdTe focal plane based detectors

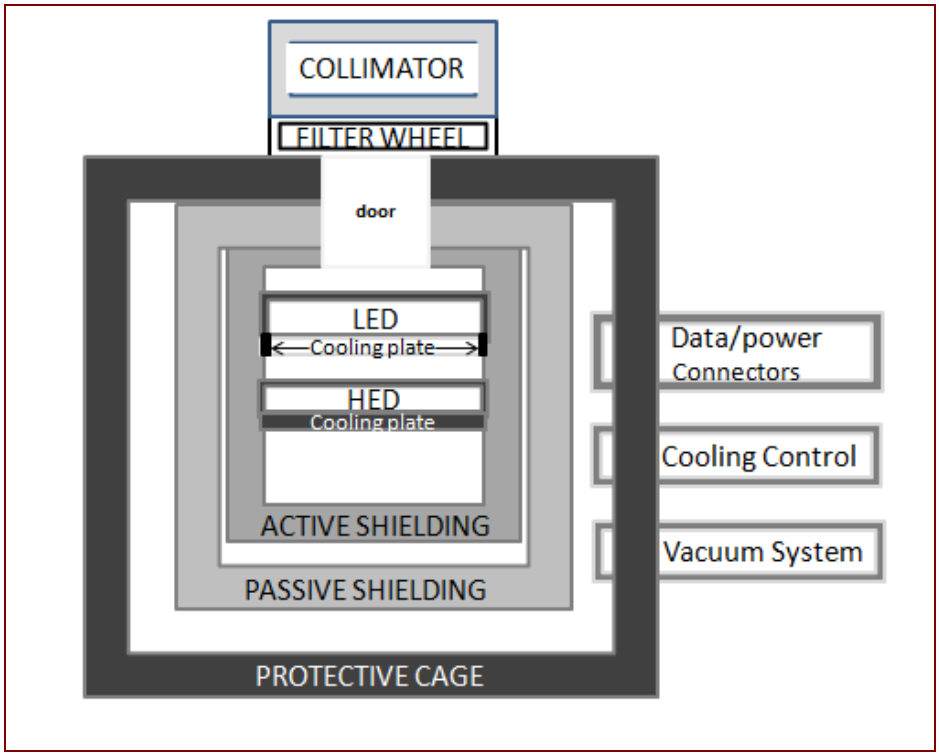

Figure 4-2: Conceptual design of the SIC. The shown configuration drives the mechanical drawing of the various components constituting the SIC

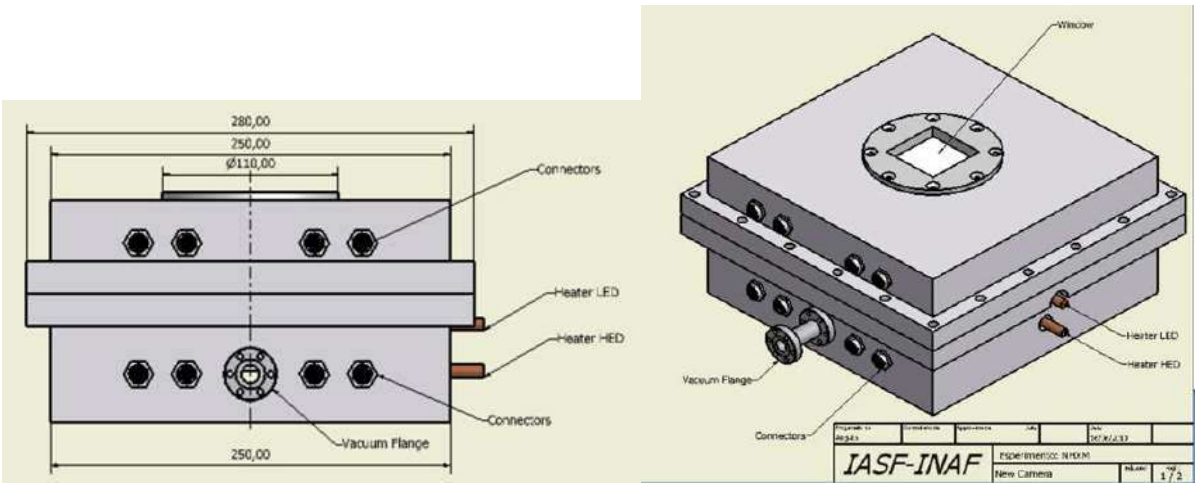

Figure 4-3: Preliminary 3D design and cross-section of the SIC

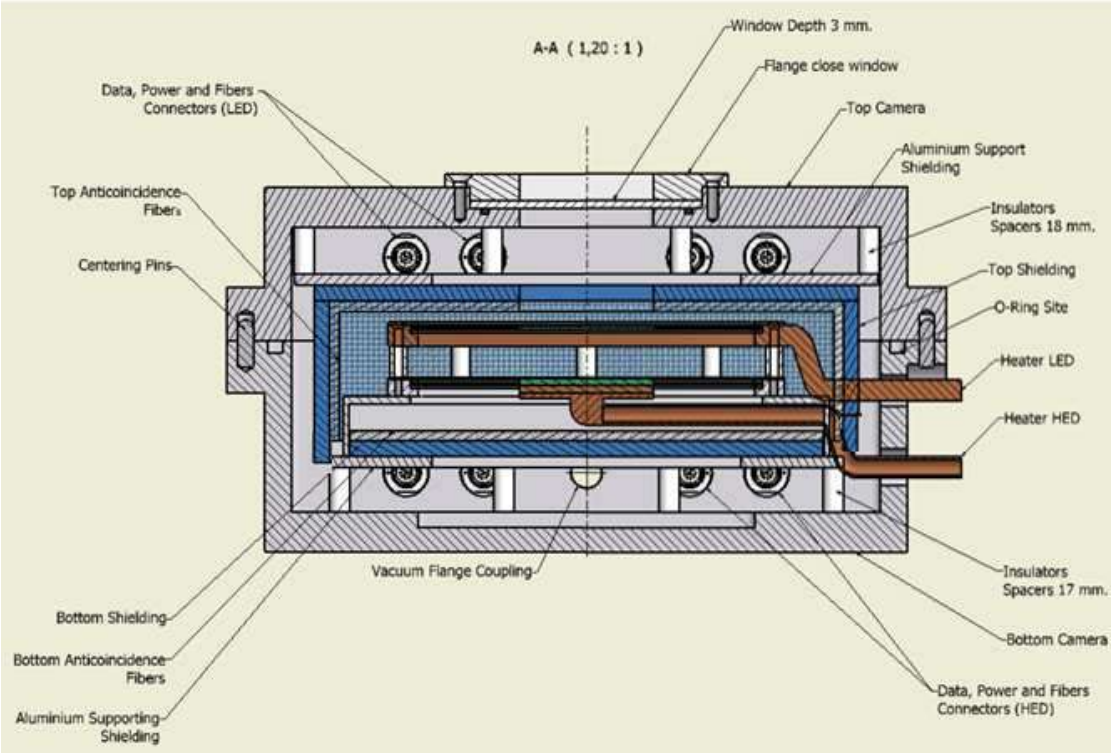

Figure 4-4: Cross-section of the SIC

The mechanical design of this SIC is shown in Figure 4-3 while its cross-section is shown in Figure 4-4.

The protective cage is made by aluminium. The cage is mechanically divided in two parts, referred in the figure as, 'top camera' and 'bottom camera'. The final size of this small camera is not only dictated by the X-sensors requirements but also by the availability of miniaturized components necessary for operation. The front door with its opening and closing mechanisms (operable repeatedly at ground, one-shot in orbit), the filter wheel with in-flight calibration source and the escape-release gas filling valve, are the elements that determine the final size of the camera and then the resources (mass, watts) that will be needed for its operation. The mechanisms outlined above, should allow the camera to be operated safely at ground, to be opened in a clean environment at ambient pressure or under vacuum. The mechanical structure of the cage is conceived to be operated at 1 differential atmosphere pressure. The aluminium cage is formed by two parts, the 'bottom camera' and the 'top camera', with in between an appropriate gasket, held together by bolts and thermally insulated by plastic spacers. The walls of the camera host the data/power connectors as well as the inlet/outlet connectors. A five position filter wheel is mechanically interfaced to the top of the camera. A filter wheel is mechanically interfaced to the top of the camera to provide five identified positions; a calibration source, a blanked off to serve as a shutter, an open position and two positions available for UV filtering. The filter wheel is then mechanically interfaced with the collimator. The collimator, 1 meter long and 75 mm diameter wide, is necessary to limit the detection of unwanted background particles and X-ray photons except for the solid angle corresponding to the optics focused beam. Passive and active shielding surrounds the detection unit. The function of the passive shield is to reject most of the possible fluorescence lines photons while the role of the active shielding, constituted by plastic scintillating fibers, is to reject the charged particles. The passive shield is coupled with an array of plastic scintillating fibers of 1 mm of diameter (multilayer ribbons) as shown schematically in Figure 4-33. The ribbon fibers consist of a polystyrene core enclosed in a concentric layer of cladding made of acrylic plastic. The read-out ends of the fiber ribbons are bundled in pairs and optically interfaced to the pixels of linear array multianode photomultipliers.

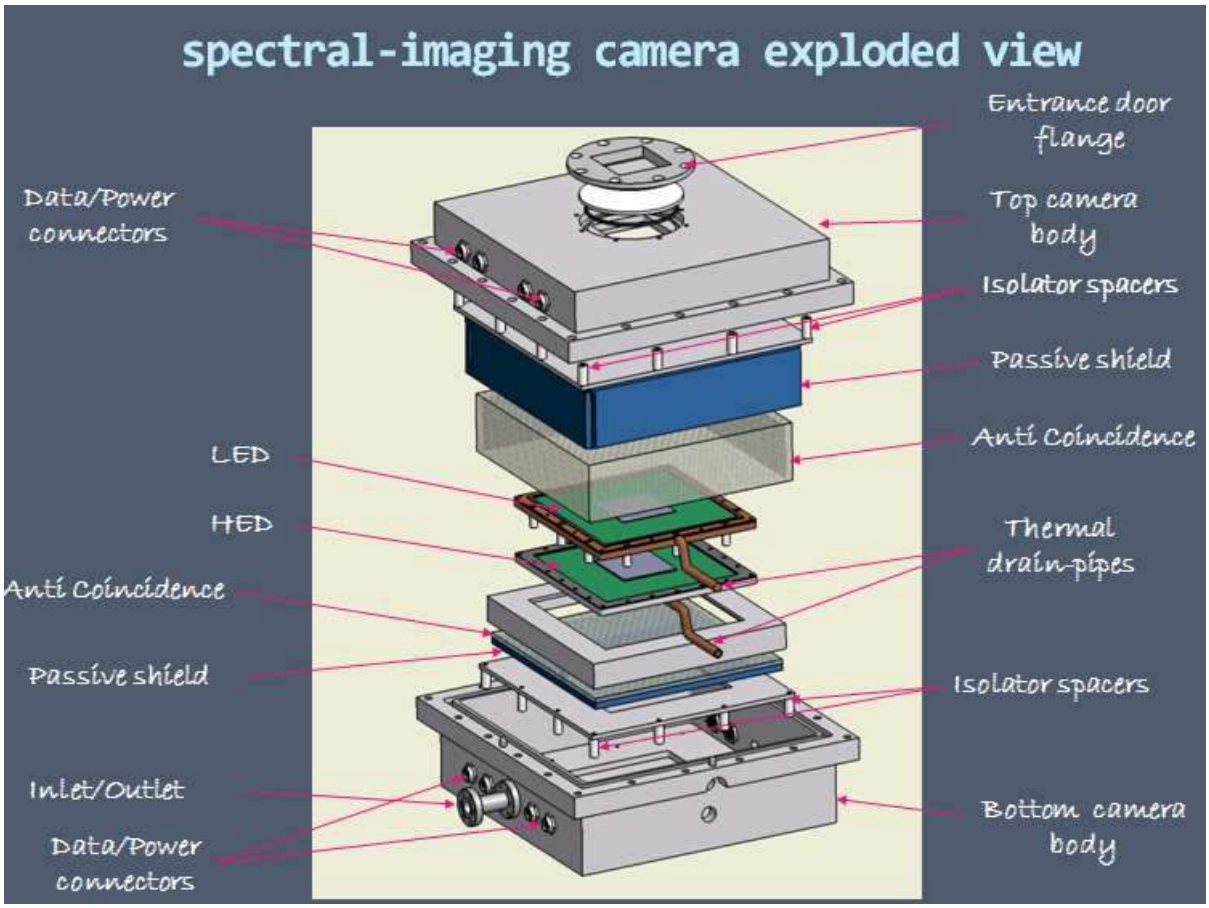

Figure 4-5: Exploded view of the camera

The fibers, in this configuration, represent a part of the anticoincidence system characterized by a position sensitive capability. The scintillating fibers do not create activation lines due to radioactive nuclides like the inorganic crystals and moreover, they produce very fast scintillation signals (typical decay time of the order of few ns). Figure 4-5 shows the exploded view of the SIC that summarizes the elements constituting the camera.

In the next configuration, for the active shielding, we studied a combination of fibers and inorganic crystal layers. In fact the latter seems more efficient in rejecting the high-energy photons (gamma-ray), that are the dominant background component for a low earth orbit as the one foreseen for NHXM.

4.3 SIC second configuration

X-rays focussed by the mirror enter the camera via an extended graded baffle tube (see sec. 4.2.3), which protrudes 900mm from the focal plane. The baffle is mechanically supported by a conical structure, mounted on the camera at the instrument platform interface plane. A door aperture sits in front of a filter wheel, which is mounted directly in front of the LED. The door is normally closed for ground testing. The main camera body can be evacuated to facilitate bench testing and to protect delicate filters from acoustic excitation during launch. The door is opened on orbit by venting a bellows via a HOP actuated valve. A stepper-motor controlled, four-aperture filter wheel is mounted directly in front of the LED and is mechanically supported by the door chamber

assembly (see Figure 4-6 and Figure 4-7). The filter wheel will provide an open and a closed position, one position with a medium filter and one with a calibration source.

The LED and HED detectors are hosted inside two very compact detector modules that will also provide an active and passive shielding to minimise the shielding mass by being in close proximity to the detectors (see Figure 4-8). The two modules will come together only at the end, allowing for independent development. The baseline configuration considers the LED and HED modules to be delivered as sealed chambers with windows and provision for venting on orbit. Sealed units result in clean interfaces and provide protection for the delivered detectors. An option for consideration would be to deliver the LED and HED units as unsealed assemblies.

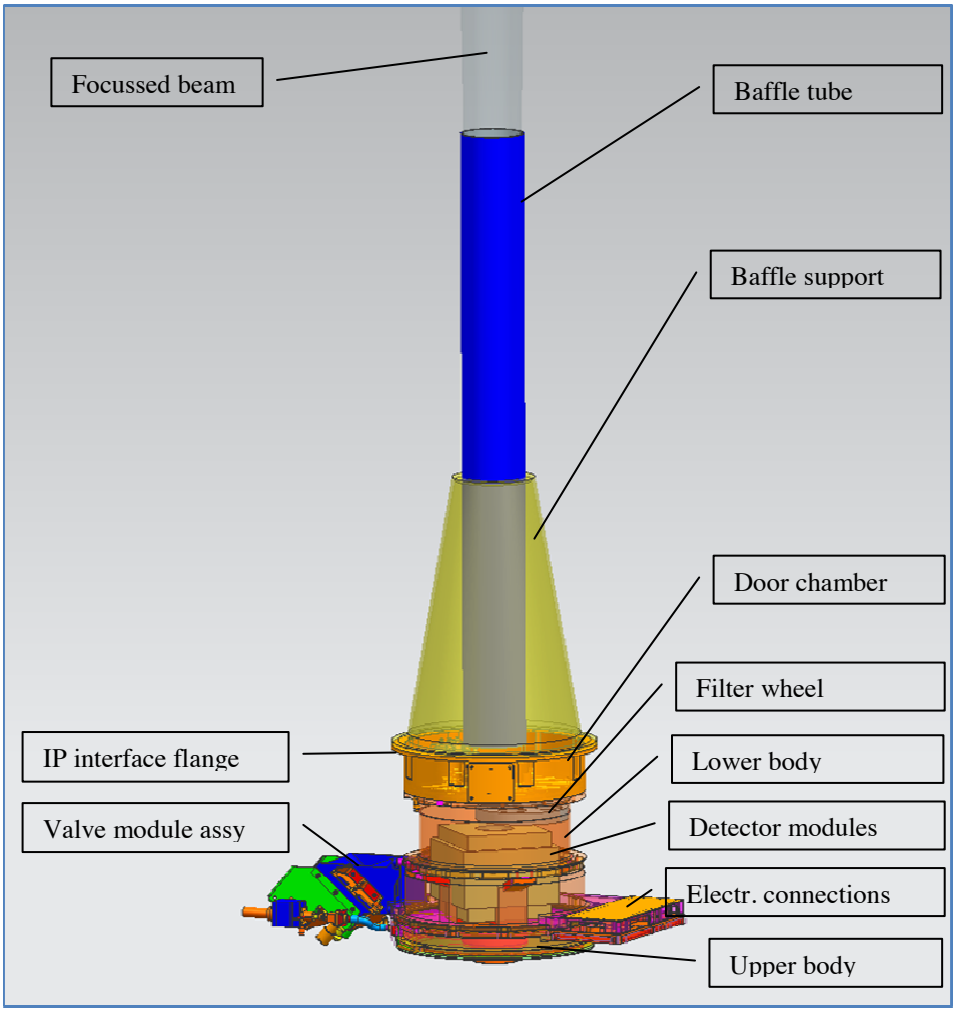

Figure 4-6 Overview of the SIC

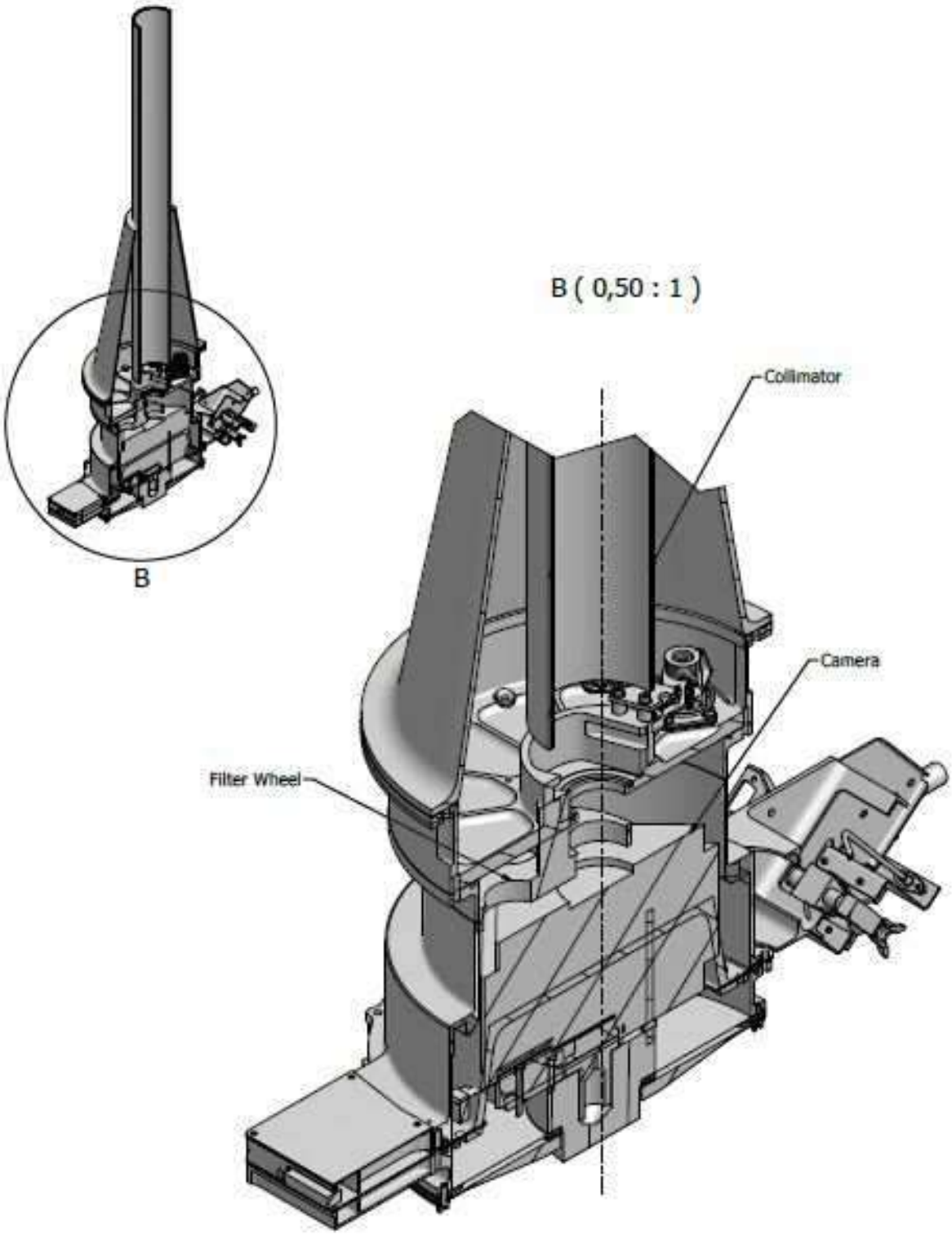

Figure 4-7 Cross section of the SIC

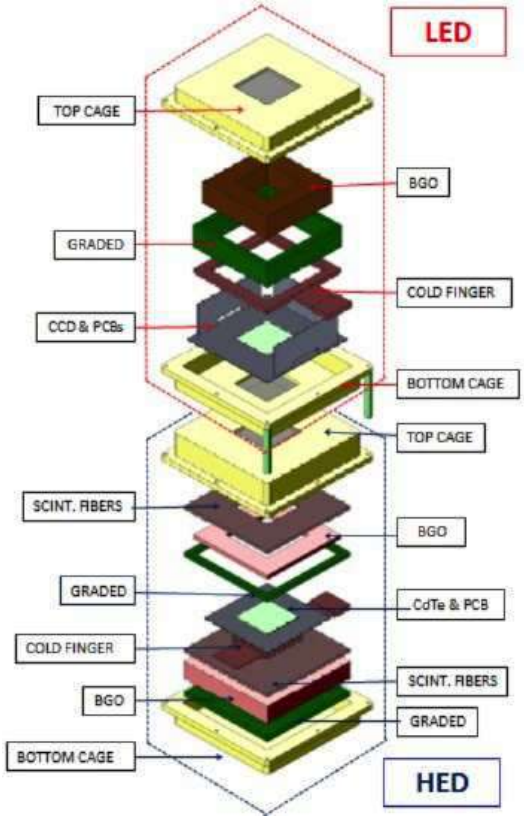

Figure 4-8 LED and HED modules exploded view

4.4 Low Energy Detector

A Low Energy Detector (LED) will be placed on the top of the focal plane assembly, with the role to detect the soft X-ray photons between 0.2 and 20 keV with a quantum efficiency higher than 95% and an energy resolution ΔE/E of 40-50 at 6-10 keV. During the NHXM study a baseline configuration for the LED has been identified and analyzed. In addition, an alternative configuration based on the CCD tecnology has been envisaged.

4.4.1 LED baseline configuration

The LED baseline configuration consists in an array of DEPFET (DEep P-type Field Effect Transistor) Active Pixels Detectors (APD). Such silicon sensor is developed at the Semiconductor Laboratory of the Max Planck Institute in Munich (Germany).

NHXM requires a pixel size lower than 350 μm x 350 μm in order to properly over-sample the optical spread function. For the LED a pixel size of 100 μm x 100 μm has been chosen to cover the desired field of view.

Moreover, the observatory's large collecting area of 1000 cm^2 at 5 keV necessitates that the imager support high frame rate (in the order of several thousand frames per second) to have a spectroscopic imaging systems performing single photon detection with a minimum pattern pile-up of the events.

4.4.1.1 Electrical Design

In Figure 4-9 is shown a first draft of the design of the LED, where all its component are placed.

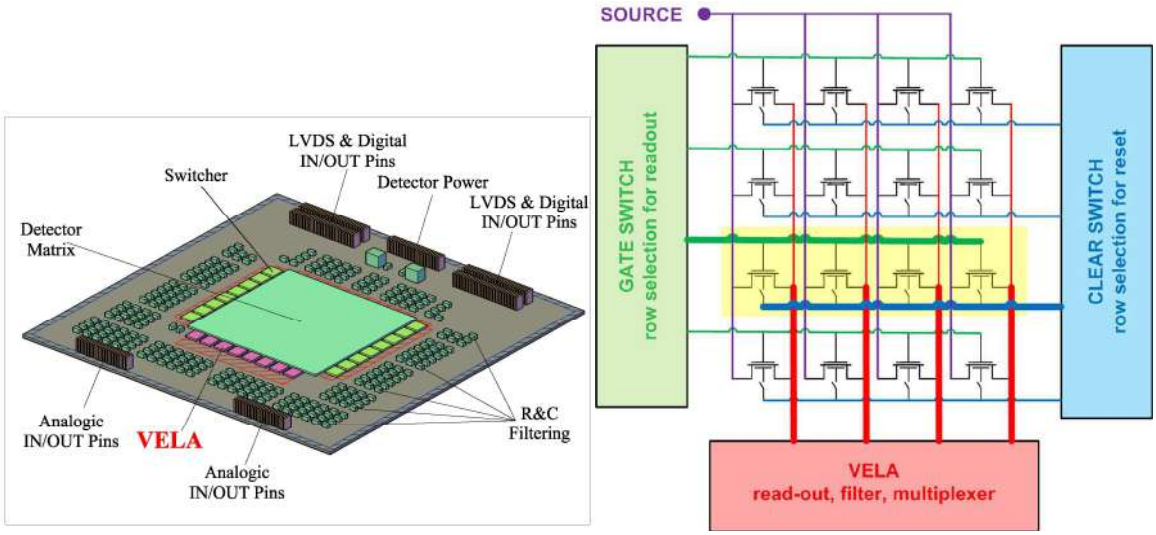

Figure 4-9: On the left side, LED Hybrid Ceramic first draft. On the rigth side, the block scheme for the operation of the DEPFET Matrix is represented.

At the centre is located the detector matrix, composed by 512x512 DEPFET detector, surrounded by 8x2 Switchers (in light green), the ASIC responsible for the switching of lines during readout, and 8 VELA chips (in pink), the ASIC responsible for the readout of the signals. The resistors and capacitances necessary to filter the signals and bias are disposed around the central area depending on their function. The input/output pins are split in two groups: on one side there are the pins for the analog signals, while on the other side there are the pins for LVDS and digital signals and also the pins used for the detector power.

The choice of a monolithic DEPFET matrix of 512x512 pixels for the LED is made to provide, at the same time, excellent energy resolution and high frame rate.

We report here a detailed list of the signal distribution divided by the component they are related:

SWITCHER

Pad	Description
A_HI	A_{high} - High voltage of channel A, analog I/O – max GNDA+20V
A_LO	A_{low} - Low voltage of channel A, analog I/O – max GNDA+5V, it must be lower than A_{high}
B_HI	B_{high} - High voltage of channel B, analog I/O – max GNDA+20V
B_LO	B_{low} - Low voltage of channel B, analog I/O – max GNDA+5V, it must be lower than B_{high}
TEST	Test output
DI	Digital input CMOS – 1= VDDF, 0=GNDF, with pull down
DO	Digital output CMOS – 1=VDDF, 0=GNDF

GNDA	ground, analog I/O – 0V (reference)
VDDA	HV, analog I/O – max 20V
VDDF	Digital power supply, analog I/O – from 0 to 20V
GNDF	Digital ground, analog I/O – from 0 to 20V
LOAD	(in the Control register latch), input CMOS – 1= VDDF, 0=GNDF, with pull down
CCK	Configuration clock, input CMOS – 1=VDDF, 0=GNDF, with pull down, active high
RESET	Counter and counter's control block reset signal, input CMOS – 1=VDDF, 0=GNDF, with pull up, active high
HARD_RESET	Control bits reset signal, input CMOS – 1=VDDF, 0=GNDF, with pull up, active high
D_D1	Dummy_Direct1
D1	Direct 1 - Digital input CMOS – 1=VDDF, 0=GNDF, with pull down, Direct1 controls the B channel
D_D0	Dummy_Direct0
D0	Direct0 - Digital input CMOS – 1=VDDF, 0=GNDF, with pull down, Direct0 controls the A channel
D_RAMCK	Dummy_RAM Clock
RAMCK	RAM counter clock if Sync bit is 0 (asynchronous mode), input CMOS – 1=VDDF, 0=GNDF, with pull up, active high
D_XCK	Dummy_Main chip Clock
XCK	Main chip clock, given to matrix and RAM counters, input CMOS – 1=VDDF, 0=GNDF, with pull up, active high

DEPFET

Pad	Description
DRAIN	-
GUARD	-
MOS	-
R1/CH_SEP	channel separation
INNER_SUB	inner substrate
TEMP_GUARD	temperature guard ring (for the temperature diode)
TEMP_P	temperature p - temperature diode anode
BS_INNER_GR	back side_inner_guard ring
BS_VOLTAGE	back side_voltage

VELA

Pad	Description
VDD_D	Digital positive power supply, +1,7V
VSS_D	Digital negative power supply, -1,7V
GND	ASIC ground
SUB_P	Substrate of digital parts, -1,7V
AMP1_CASp	Reference voltage for filter: gate voltage of the PMOS in the mirror
REF_DACs	Reference voltage for bias master reference: provides DAC FSR for bias currents, -250mV
CS_G	Internally generated DAC reference, carried out from the ASIC for filtering reasons
VDD_SC	Positive power supply for input active cascode, reserved because it requires clean supply
VSS_SC	Negative power supply for input active cascode, reserved because it requires clean supply
AMPN_REF	External reference voltage for current memory cell, 0V
IN_TEST	Analog test voltage input
VSS	Analog negative power supply, -1,7V
VDD	Analog positive power supply, +1,7V
VSSS	negative power supply for current memory cell, till -20V
TEST_OUT	Analog output of the current memory cell
OUT+	Differential buffer positive output
OUT-	Differential buffer negative output
VSS_BUFF	Buffer negative power supply, -1,7V
VDD_BUFF	Buffer positive power supply, 1,7V
GND_BUFF	Buffer ground
S_CLK+	LVDS sequencer clock input
S_CLK-	LVDS sequencer clock input
TG+	LVDS Sequencer output trigger to check synchronization
TG-	LVDS Sequencer output trigger to check synchronization
CS+	LVDS SPI control chip select input
CS-	LVDS SPI control chip select input
CDO+	LVDS SPI control serial data output
CDO-	LVDS SPI control serial data output
CCK+	LVDS SPI control clock input
CCK-	LVDS SPI control clock input
CDI+	LVDS SPI control serial data input
CDI-	LVDS SPI control serial data input

MUX_OUT+	LVDS MUX serial data output
MUX_OUT-	LVDS MUX serial data output
MUX_CLK+	LVDS MUX clock input
MUX_CLK-	LVDS MUX clock input
MUX_IN+	LVDS MUX serial data input
MUX_IN-	LVDS MUX serial data input

Front-end Electronics

In order to fully exploit the speed capability of the DEPFET array, a readout architecture based on the VELA circuit has been chosen, which implements a drain current read-out.

It is important to highlight that during the signal integration the drain current may be turned off and only switched on for the signal readout. In this way, DEPFET can be grouped together in a matrix arrangement, with the possibility of random pixel access, allowing the application of flexible readout operation at temperatures foreseen to be in the range -60 ÷ -40 °C.

VELA is a CMOS circuit, whose structure is schematically shown in Figure 4-10, developed to operate the DEPFET pixels in a drain current readout configuration in order to implement an extremely fast readout (2 μs per row and below) and preserve the excellent noise performance of the detector. An I_{BIAS} memory cell is required to subtract the pixel bias current at the virtual ground of the filter to enable to process only the signal, which is almost two orders of magnitude smaller than the bias current, and to amplify it as much as possible in the first stage.

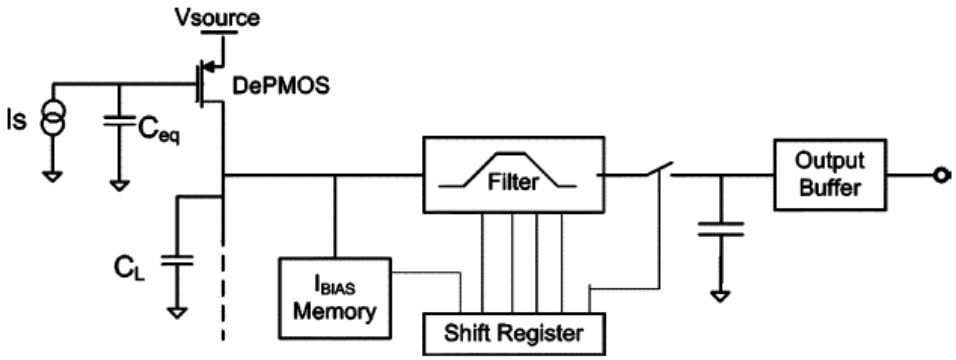

Figure 4-10: Simplified structure of VELA read-out.

The filter implemented realize a trapezoidal weighting function (Figure 4-11), which represents a good approximation of the triangular optimum filter for white series noise, dominant at processing times lower than 4 μs. VELA operates two integrations of the drain current: in the first one the signal and the baseline are read and their value is stored, while in the second one only the baseline is present and the integration result is then subtracted to the former. The necessity to have the flat-top is due to the time requested from the circuit to reset completely the detector and be ready for the second integration and its duration has been minimized to approximately 330 ns. It may be observed that the flat-top has to be minimized because, even if does not directly impact on the white noise, reduces the time available for the integrations and increases the contribution

of the 1/f noise. The first and second integration times depend on the speed requirements and for a processing time of 2 μs are 670 ns each, while another 330ns are needed to switch the row.

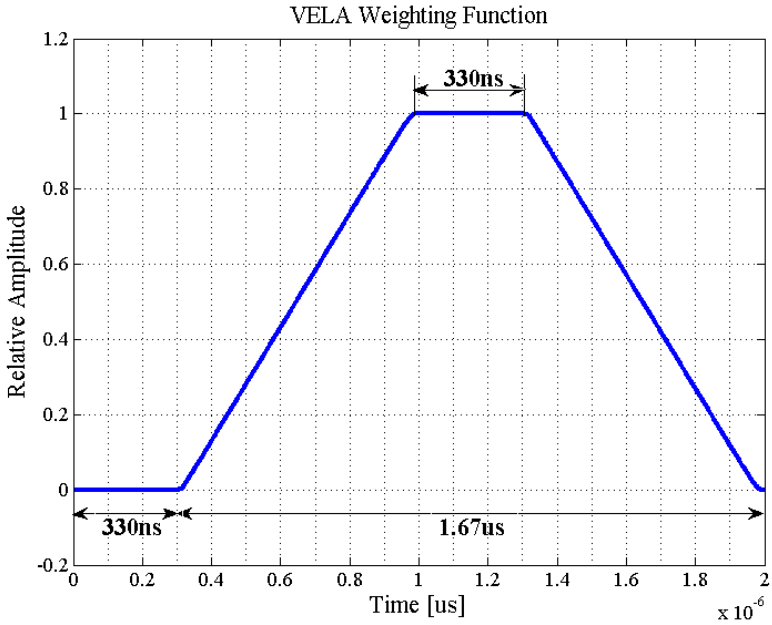

Figure 4-11: Simulated weighting function of VELA for a processing time of 2 μs.

Due to the fact that VELA is a drain current readout system, each DEPFET pixel will be operated in a "common source" configuration, so the sources of all pixels will be connected to a common voltage, while the drains will be grouped column-wise.

The detector matrix is read row by row in sequence and all the pixels in a row are read in parallel, therefore if the readout time is 2 µs, to read all the matrix of 512x512 pixels (Full Frame Mode) a frame rate of 1 thousand frames per second is obtained. If a higher frame rate is needed, VELA allows either to reduce the readout time to 1 µs (however increasing the noise in the measurement) or to read the matrix in "Window Mode", selecting only a channels subset and improving consequently the frame rate. The different frame rates achievable for different configurations are reported in the following Table. In windowing mode, it is foreseen to readout 64x64 pixels in order to completely acquire the point spread function of the mirror for a point like object. The achievable time resolution is easily compatible with the NHXM scientific requirement of 100 µs (driven by pulsar science requirements).

Foreseen LED detector readout with VELA		
Focal Plane Size (mm)	51.2	
Pixel matrix	512 x 512	
Pixel size (µm)	100	
DEPFET Polarization Current (µA)	300	
Readout time (µs)	1	2
Readout noise (electrons)	8.3	5
Full frame mode Frame rate (frame per second)	2k	1k
Window mode (64 channels out of 512) Frame rate (frame per second)	16k	8k

A single VELA chip integrates 64 analog shaping filters, 64 sample/hold stages (S&H), one analog multiplexer, and a fast differential output buffer.

The complete block scheme of the ASIC is shown in Figure 4-12.

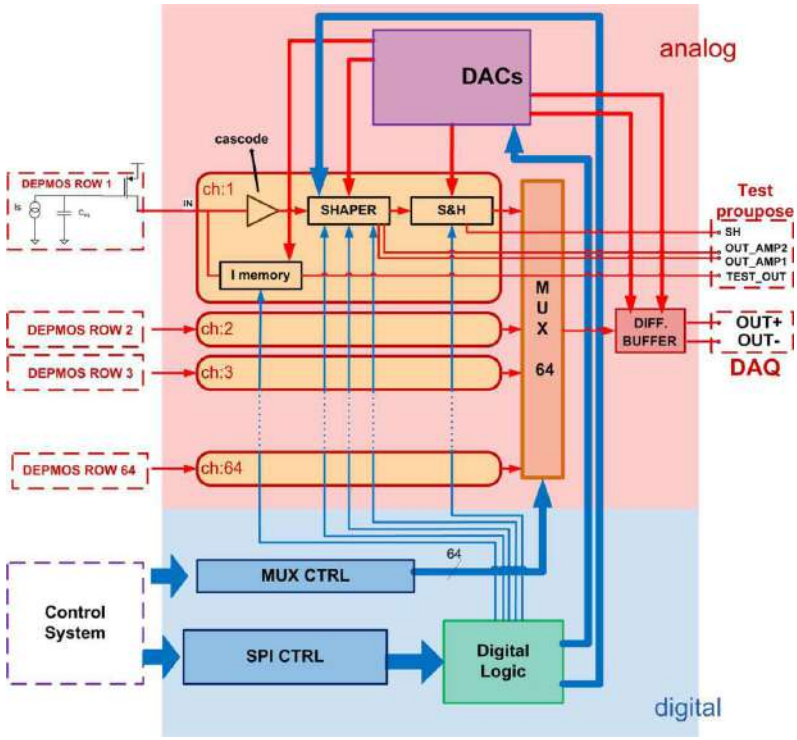

Figure 4-12: Block scheme of the complete VELA ASIC

Moreover, a digital section generates all the programmable control signals for the filtering stages. Every function of the circuit can be digitally controlled with SPI (Serial Peripheral Interface) commands. The analog gain can be selected and the readout speed can be remotely adjusted as well. Moreover, several testing features and debugging operations can be remotely performed in order to verify the proper functionality of all the integrated parts. Even the biasing condition of all the analog stages and thus the total power consumption of VELA can be adjusted using internal DACs.

Independent logic (named MUX CTRL) is designed to operate the multiplexer and the S&Hs. This logic implements additional features to the multiplexing operation like the possibility to choose between full-frame or window mode, described above.

The layout of VELA is shown inFigure 4-13. The circuit has been fabricated in 0.35 AMS CMOS technology; the chip size is 5.2 mm 4.6 mm. The pitch of the input PADs is 72, which is suitable to direct bond VELA to a standard DEPFET matrix of 75 pitch. VELA has a slightly smaller pitch in order to tile different ASICs; thus it is also possible to operate a bigger matrix array up to 1024 x 1024 pixels. The total power consumption of VELA is in the order of 0.5 W when the chip operates at the maximum speed, but it can be reduced by a factor of 2 when longer processing times are allowable.

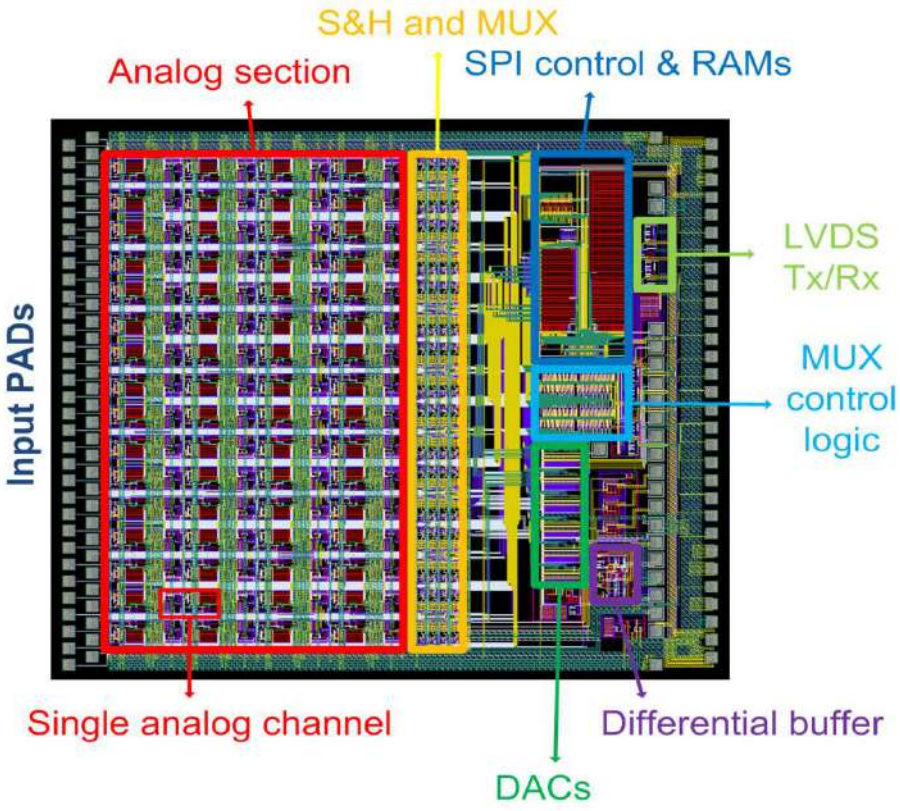

Figure 4-13: Layout of 64-channel VELA chip, the circuit has been realized in 0.35 µm AMS technology, chip size is 5.2 mm x 4.6 mm.

Each analog channel is connected to a dedicated sample/hold stage followed by a 64:1 multiplexer. At the end of the processing time, the output values of all the channels are simultaneously sampled by the respective S&Hs. During the readout of the next detector row, the multiplexer is operated in order to serialize the stored values and to provide them to the differential buffer.

In order to drive directly a differential line, the ASIC integrates an output driver based on 2 amplifiers with a common mode feedback, in order to convert the single ended input (coming from the multiplexer) into a differential output. A third amplifier is needed to provide the current required by the resistive feedback. Like the multiplexer and the S&Hs stages, the driver is designed to have a bandwidth of 100 MHz and a slew-rate of 100. The output buffer can drive a 50 Ω (or 120 Ω) terminated line and a capacitive load up to 10 pF. The power consumption is about of 20 mW.

After a settling time of 25 ns, the ADC can sample the amplitude and start the conversion. Since acquisition system discard all the pixel values which are comparable with the noise level, the needed accuracy in the output is in the order of $4 \cdot 10^{-4}$.

The SPI CTRL logic is mainly composed of two SRAM memory fields and of a slow control interface that programs the memory. The first memory bank (of 16 words) is used like a register file. It contains the information for the static settings of the ASIC, like the selectable gains and the DACs values. A second memory field (of 64 words) contains the timing sequence values for the switched-capacitor circuit in the analog channel. A sequencer circuit is associated with this RAM field. It addresses one word of the RAM, it reads the contained values, and it operates the switches inside the analog channels accordingly. At the next clock cycle of SCLK, the next RAM word is addressed. The SRAM fields are based on Dual Port DICE (Dual Interlocked Storage Cells) cells. The use of this structure is needed because they are immune to soft SEU (Single Upset Event) errors during the space mission.

Since dual port memory is implemented, the content of the memory can be readout nondestructively and rewritten during the operation time. In addition, it is possible to reset the timing sequence by resetting the address vector in the sequencer circuit. This is extremely useful to keep more ASICs synchronized. The input clock (SCLK) and all the other digital lines for SPI programming are transmitted using on-chip LVDS transmitters/receivers. This enables to reduce the interference on the analog lines.

4.4.1.2 Mechanical Design

For each component of the LED Hybrid Ceramic (Detector Matrix, Switchers, VELA chips, IN/OUT pins, filtering R&C) there was a first estimation of the area occupation. We report here some of the preliminary drawings:

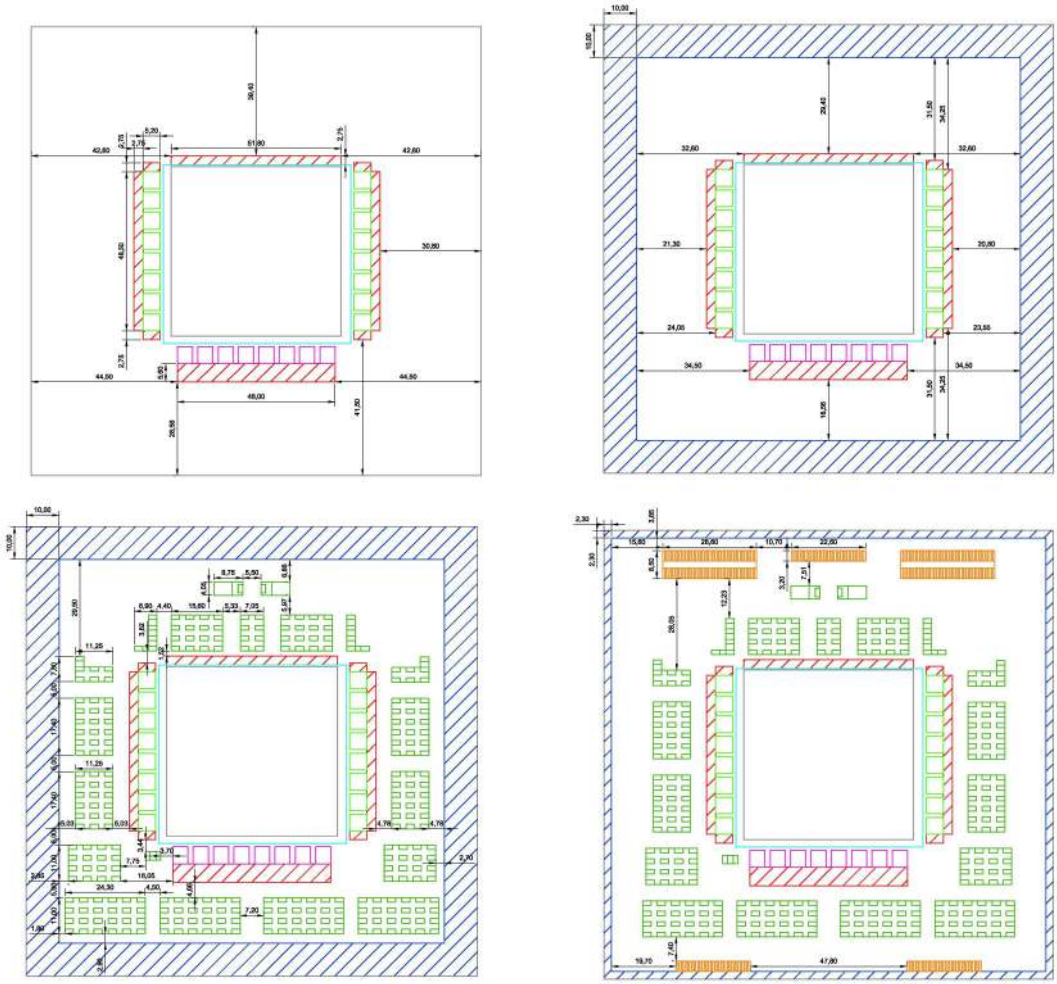

Figure 4-14: Drawings made for the components' positioning on the LED Hybrid Ceramic

The outer square area is 137x137 mm^2 and represents the LED Hybrid Ceramic foreseen total dimensions. The zones in red stripes are necessary to bound the VELA chips, the DEPFET Matrix and the Switchers. The zones in blue stripes are to be left free for connectors and clamps. In the last drawing, the connectors are positioned and the blue stripes reduced consequently.

4.4.1.3 VELA radiation tests

Radiation tests have been carried out on the VELA ASIC in order to evaluate the behaviour of the device on orbit. In order to study the effects due to the cosmic-ray flux, we irradiated the chip with heavy ions at the SIRAD radiation facility, which is specifically designed for bulk damage and single event effect studies in semiconductor devices and electronic systems. SIRAD is located at the +70° line of the Tandem-XTU electrostatic Van de Graaf accelerator of the INFN National Laboratory of Legnaro. The Tandem maximum operating voltage is 15 MV and available ions range from ^{1}H (30 MeV) to ^{197}Au (about 300 MeV).
The test setup for the VELA ASIC has been developed specifically for these measurements. It is based on two *ad-hoc* designed PCBs and a commercial data acquisition system (DAQ) from National Instruments, controlled from a PC with a LABVIEW-based software. A block diagram of the test setup is shown in Figure 4-15.

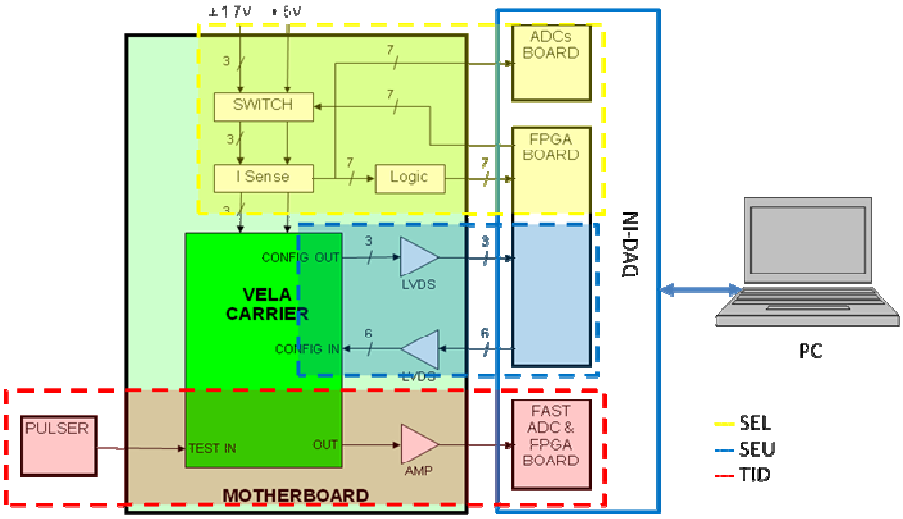

Figure 4-15 Block scheme of the experimental setup.

The DAQ system is based on a PXI-1073 chassis hosting:

1) a FlexRIO 7952R (a module based on a Xilinx Virtex-5 LX50 FPGA) with the NI6581 adapter (54 single-ended digital I/O channels up to 100 MHz): this module is used to generate and manage all the signals required for VELA control

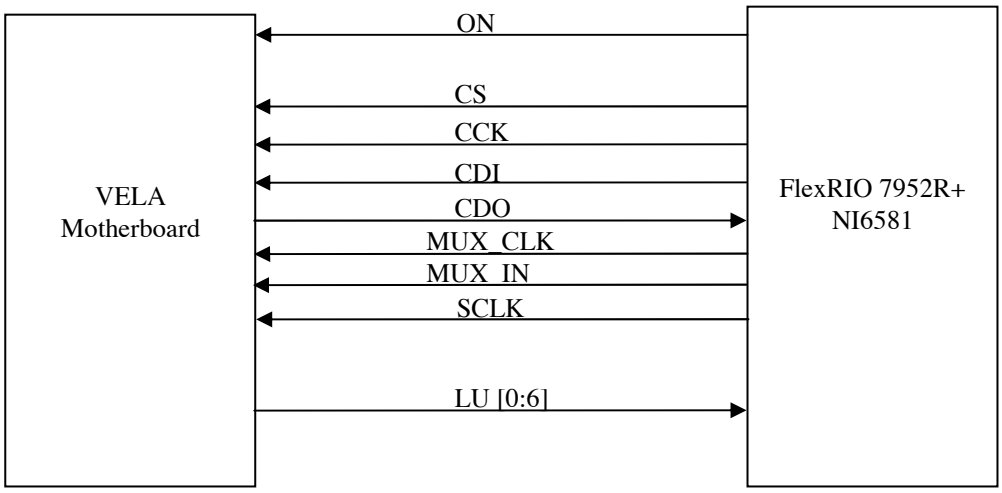

Figure 4-16: Signals connections between VELA motherboard and the DAQ.

2) a NI6224 (a 16 bit 250 Ks/s ADC board with 32 Analog Input): used for monitoring the VELA power supply currents (7 signals are independently recorded at 30Ks/s)
3) a second FlexRIO 7952R module with the NI5761 adapter (a 14 bit, 500 MHz bandwidth, up to 250 MS/s ADC with 4 input channels): foreseen for the acquisition of the analog output of the VELA

The functions implemented in the LabView-based software are the following:

a) VELA startup and configuration (via SPI interface)
b) SEU monitoring
- write/readout of the VELA configuration (via SPI interface)
- looking for flipped bits
- write a SEU log file for each event detected

c) Latchup (LU) monitoring
- set current threshold (via a dedicated 8-bit DAC)
- if one or more currents rises over threshold, switch off the device, wait for a user-selectable time (3s for all the tests carried out) and try to switch-on the device
- write a LU log file for each event detected

d) VELA controller: generation of the signals required for VELA readout and for triggering a waveform generator used to inject a pulse in the VELA TEST IN input, in order to simulate an x-ray photon event.

The main PCB (Motherboard) can accommodate a smaller board (Carrier) with the VELA device (Figure 4-17).

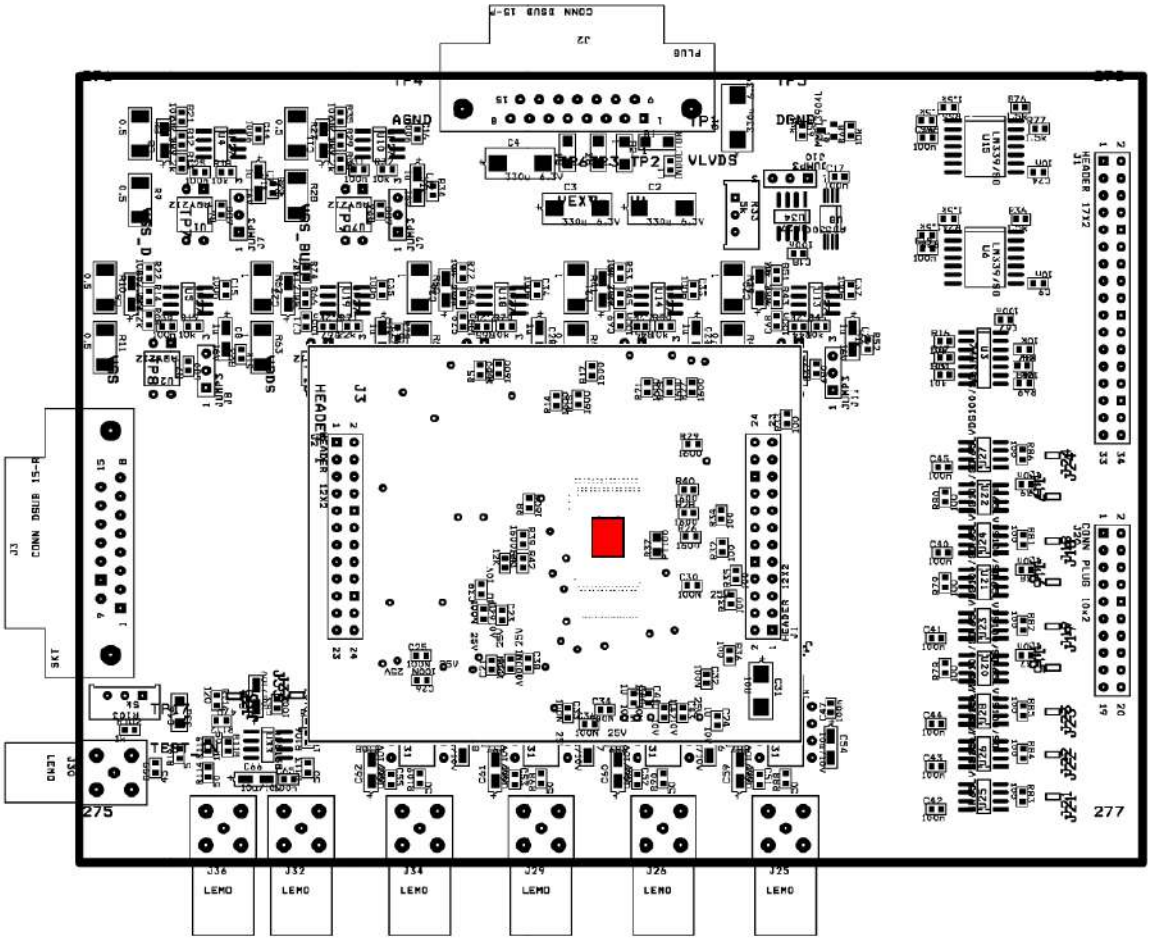

Figure 4-17 The layout of the Motherboard PCB with the Carrier PCB on it. The red rectangle indicates the position of the VELA ASIC.

The Motherboard contains some circuits to control the current from the power supply lines of VELA; if a latchup event occurs a signal is sent to the DAQ. The FPGA of the FlexRIO 7952R+ NI6581 module commands a digital signal to the input of an OptoMOS device on the Motherboard, used to interrupt the power supply line. The implementation in FPGA, instead of a software-based control, allows a much faster reaction, better protecting the device.

All the current values of the VELA power supplies are recorded using ADCs in order to control the time variations during a latchup event.

The following Figures illustrate the experimental setup installed on the SIRAD facility at the Legnaro INFN laboratory.

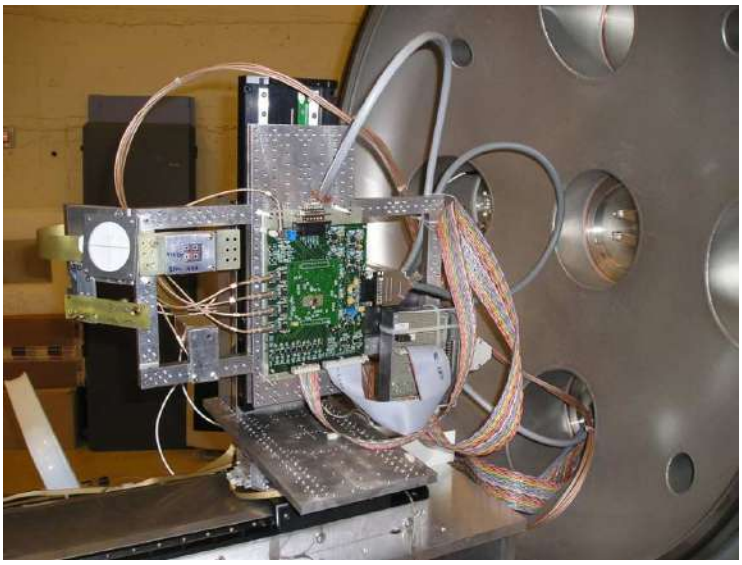

Figure 4-18 The Motherboard and the Carrier PCBs inside the vacuum tank. On the right are visible the connectors fixed on the door tank.

Figure 4-19 A close-up view of the the Motherboard and the Carrier PCBs. The flat cables at the bottom are used for digital signals (latch-up current triggers and LVDS VELA controls); the LEMO connectors on the left and top are VELA analog outputs and the test input respectively; the DB15 at the top of the Motherboard is used for the latch-up analog signals and the DB15 connector on the right is connected to the power supplies.

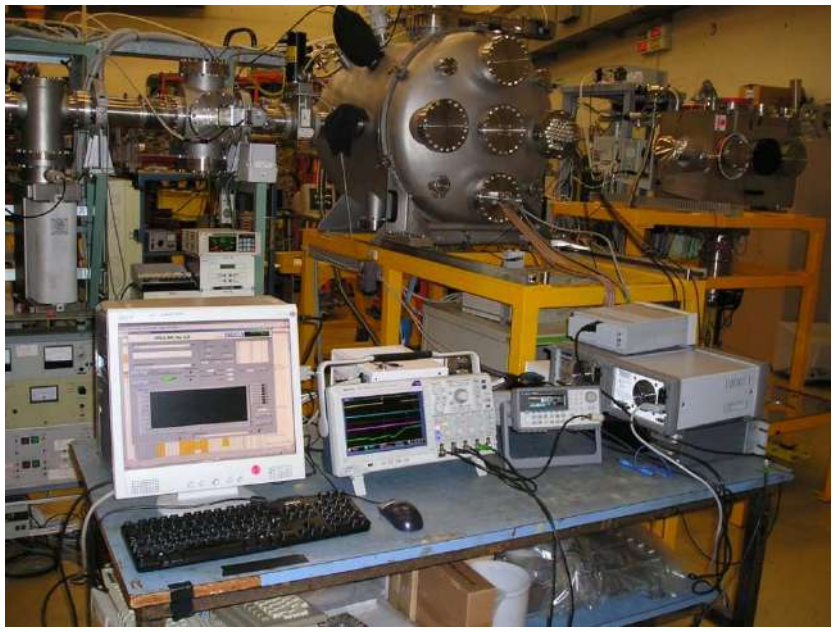

Figure 4-20 The measurement setup in front of the vacuum tank (on the background, already closed). On the table, from left, there are the PC with the LabView software, the digital oscilloscope for waveforms control, the PXI chassis (barely visible behind the oscilloscope), the signal generator and the power supplies.

We used incident particles with different atomic number and energy, in order to test the device with different values of Linear Energy Transfer (LET), also exploiting the possibility of tilting the sample to increase the number of data points. Two VELA chip has been used during the tests: the first one failed at the beginning of the measurements, likely due to the choice of a too high level for the current limitation which allowed damaging the device. All the measurements reported has been obtained with the second chip.
The number of latchup events has been derived by the number of time the latchup protection circuit was activated by one or more current lines crossing the threshold, corrected for the 3s dead time (all the data are reported in Table 4-1). We also observed some "anomalous events" in which one or more currents raised but reached a plateau below threshold.
Given the number of latchup N_{LU} for a LET, the latch-up probability and the cross section, respectively, are:

$$P_{LU} = \frac{N_{LU}}{\phi t S} \qquad \sigma_{LU} = \frac{N_{LU}}{\phi t}$$

where ϕ is the incident flux (monitored by photodiodes), t is the live time and S is the chip geometric surface. No latch-up event have been recorded during the two irradiation with 19F (LET 3.67 and 5.19 MeV cm^2mg^{-1}), only un upper limit can be derived for these LET values. The plot of the data is shown in Figure 4-21.

ion	MeV	angle (°)	LET (Mev cm2 mg-1)	exposure time (s)	incident flux (ions cm-2 s-1)	measured LU	anomalous events	effective LU	cross section (cm2)
19F	123,643	0	3,67	960	1,2782E+07	0	0	0,0	0,0000E+00
19F	123,643	45	5,19	3600	1,4499E+08	0	0	0,0	0,0000E+00
28Si	157	0	8,63	1440	6,5475E+07	178	0	282,9	4,3209E-06
35Cl	159,39	0	12,96	3600	9,6488E+06	135	0	152,1	1,5765E-05
35Cl	159,39	45	18,33	3600	6,4031E+06	140	18	158,5	2,4752E-05
58Ni	228,24	0	27,70	3600	1,5679E+06	98	6	106,7	6,8062E-05
58Ni	228,24	30	31,99	3600	2,6180E+06	243	29	304,7	1,1639E-04
58Ni	228,24	45	39,18	3600	2,1513E+06	260	13	331,9	1,5429E-04
79Br	240	0	38,14	3240	2,0160E+06	309	-1	432,8	2,1470E-04
79Br	240	45	53,95	1020	4,3004E+05	66	-1	81,9	1,9044E-04
107Ag	266	0	53,04	2340	4,6446E+05	117	6	137,6	2,9636E-04

Table 4-1rradiation test latch-up measures.

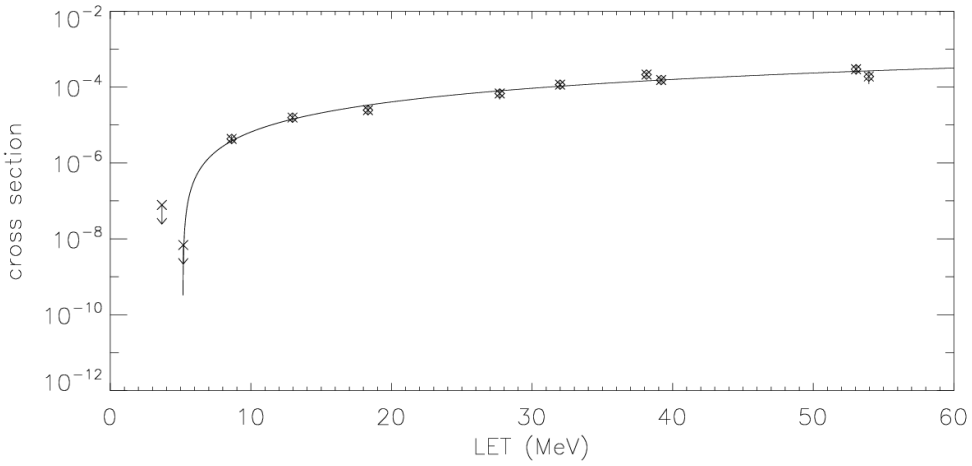

Figure 4-21Results of the latch-up measurements. The first two points are upper limits since no latch-up have been detected. The solid line is the fit of the data with a Weibull function.

The cross section data points have been fitted with a Weibull function:

$$\sigma_{LU} = \begin{cases} \sigma_{\infty}\left(1-\exp\left[-\left(\dfrac{LET - LET_{thr}}{W}\right)^{S}\right]\right) & LET \geq LET_{thr} \\ 0 & LET < LET_{thr} \end{cases}$$

where σ_∞ is the plateau cross section, LET_{thr} is the LET threshold, W and S are dimensionless parameters. The results of the fit are the following:

$$\sigma_\infty = (1.8 \pm 0.8) \cdot 10^{-3} cm^2$$
$$LET_{thr} = (5.2 \pm 0.1) MeV \cdot cm^2 \cdot mg^{-1}$$
$$W = (150 \pm 50) MeV \cdot cm^2 \cdot mg^{-1}$$
$$S = 1.64 \pm 0.04$$

Even if the expected latch-up rate during the NHXM mission is negligible, since the devices with LET threshold smaller than 10 MeV cm^2mg^{-1} can suffer proton-induced latch-up, it could be safer to consider the use of a latch-up protection system.

Instead, no SEU has been detected in all the measurements carried out (neglecting the errors produced next to latch-up events). This is in agreement with the particular design adopted for the memory cells (DICE, or Dual Interlocked Storage Cell, see *T.Calin, M.Nicolaidis, R.Velazco - IEEE vol.43, pp.2874,1996*), which make VELA insensitive to SEU events.

4.4.2 LED alternative configuration

The LED shall satisfy the requirements listed in Table 4-2. Based on them and on the level of readiness we select an e2v technologies, back illuminated, NIMO, CCD-230/231 with 30μm pixels (2048×2048 format). An aluminium coating can be applied to the device in order to filter out background light.

Table 4-2: LED specification

Parameter	Value
Energy Range	0.3-10 keV
Focal Plane Size	40×40 mm^2
Pixel size	100 - 200 μm
Energy resolution	120-150 eV at 6 keV
Background	< 1×10^{-3} cts $s^{-1}cm^{-2}$ keV^{-1}

This detector is already available as COTS with a depletion layer of 70μm, with an ongoing program to get deeper depletion (80-120μm, with a goal of 150μm). Therefore our baseline is a 120μm (goal 150μm) depletion layer device, with the following key characteristics:

- Back illuminated CCD – with high low- energy QE (see Figure 4-22)
- 10 full frames per second acquisition rate
- Frame-transfer, image area 6cm X 6cm
- Non-inverted mode operation (operating temperature ~-80°C)
- Readout noise of 3 electrons (rms)
- A store region to avoid image/spectral degradation during readout
- Multiple output nodes (high speed readout)
- 2-4 X on-chip column/row binning
- QE 98% at 6 keV and 59% at 10 keV

This low-energy detector will be thinned to ~150μm to ensure adequate transmission for energies above 10 keV. Windowing mode operation will enable high-speed readout, ~50-100 s^{-1}, avoiding pileup for bright sources (with a pixel size of 100μm we can observe a 100 mCrab source with less than 5% pileup).

We note that for the COTS CCD with a 70μm depletion layer the detection efficiency is already 88% at 6 keV and 40% at 10 keV and this option can be taken as a back-up solution.

Each detector module comprise; a CCD detector, a TEC-based thermal cooling system (the nominal operating temperature is -80 °C, although the possibility of having the CCD run at -60 °C can also be explored) and a store shield. Two low mass flexis with 37-way micro-D connectors are incorporated in the detector package to carry the drive and power signals from the CCD to the proximity readout electronics. The CCD connections can be wire bonded directly to the flex. The CCD carrier is bonded to a TEC using an adhesive with high thermal conductivity and (the warm side of) the TEC is bonded to a thermal heat sink plate. A BEE based on an AD-converter and FPGA circuit completes the LED assembly.

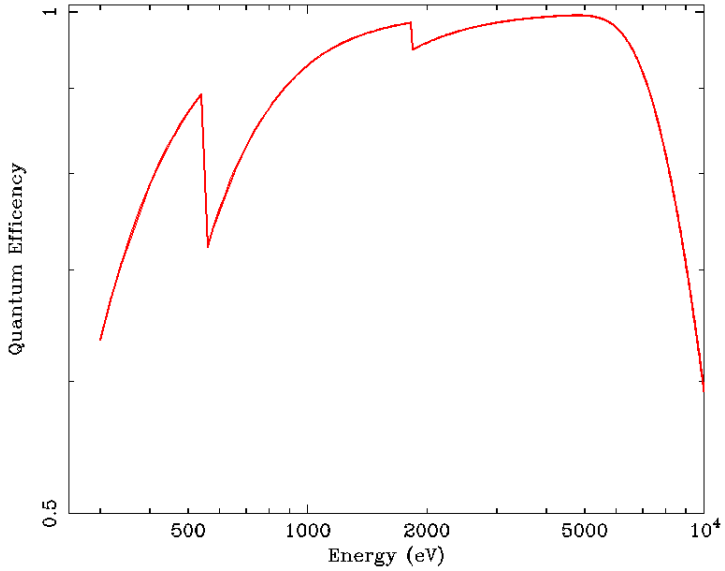

Figure 4-22: QE of the CCD with 120μm depletion layer

4.5 High Energy Detector

The Si active pixel sensor 1mm thick covers the energy range up to 12-20 keV. A Cadmium Telluride CdTe detector, 1-2mm thick, placed behind the LED, extends the energy range up to 120 keV, detecting the most energetic photons focalized by the mirror. The QE efficiency of a stack of one Si LED 1mm thick and of one CdTe sensor 2mm thick is well over 95% in the whole energy range of NHXM (Figure 4-23).

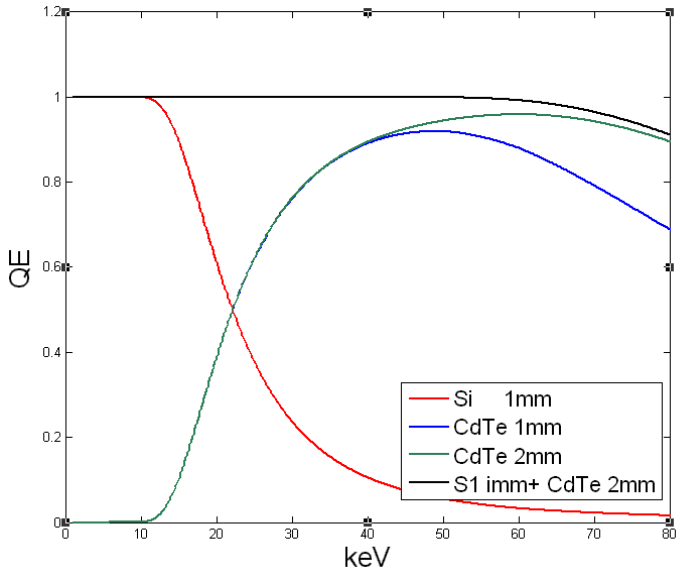

Figure 4-23 QE versus energy of 1 mm thick Si detector on top of a1- 2 mm thick CdTe detector

The physical characteristics of the CdTe are listed in Table 4-3. The mobility, the charge carriers lifetime, the energy gap are close to the Si values, but the density and the high Z make this crystal very interesting for energies >10keV. CdTe pixels sensors with Schottky contact have a very low leakage current ~10 nA/cm^2 which allows very good spectroscopy (980 eV FWHM @ 59.5keV has been measured by Tanaka et al. [4]). The Schottky CdTe is more tolerant to radiation than the classical ohmic type, already used for the ISGRI camera on board of the INTEGRAL satellite.

Reliability, radiation tolerance, low power consumption and low-noise read-out electronics, in combination with high quality CdTe crystals covered with small size pixels, are mandatory in the development of detectors for space applications. The CdTe pixel detectors are the baseline for several X-ray missions (INTEGRAL, IXO, ECLAIRs, NUSTAR, NEXT).

CdTe crystals with charge collecting electrodes in Aluminium with metal-semiconductor junction allows collecting electrons instead of holes, as in standard ohmic junction, resulting in higher performance of the device in terms of charge collection yield and speed.

To avoid gain instabilities due to polarization effects by trapped charge and to achieve the required spectral resolution the CdTe detectors will operate at T< -20°C.

Parameter	Value
Density:	5.8 gcm^{-3}
Z:	48 - 52
E_{gap}:	1.44 eV
W:	4.43 eV
Resistivity:	10^9 Ωcm
μ_e:	1100 $cm^2s^{-1}V^{-1}$
T_e:	3×10^{-6} s
μ_h:	100 $cm^2s^{-1}V^{-1}$
T_h:	2×10^{-6} s

Table 4-3: The main physical properties of CdTe

4.5.1 Detector Design

The NHXM CdTe pixel detector is a hybrid configuration detector obtained by bump-bonding a pixilated Schottky barrier CdTe crystal (2 mm thick) onto a pixel readout ASIC.

To cover the FOV of each NHXM spectral-imaging cameras (12' at 30 keV) the detector size should be 40×40 mm^2. The requested area will be realized with a 2×2 array of hybrid modules formed by a CdTe pixel detector bump-bonded to a custom ASIC with contact pads on the back side. The via interconnection technology adopted for the ASICs to bring contacts on the back side is shown Figure 4-24.a. A deep etch from the back side up to the Al pad on the front side realizes the via through the ASIC thickness. In this way the CdTe+ASIC modules can be bump bonded onto the printed circuit board (Figure 4-24.b) to form a 2x2 matrix (Figure 4-24.c) with very limited dead space (< 200 μm).

To over-sample the mirrors PSF (<15'', ~ 700 μm on the detector plane) a pixel size of 200 μm has been chosen for the CdTe sensor. This value results from a good compromise between a fine angular resolution, a good energy resolution (events confined within a pixel), a reduced level of electronics noise (proportional to the pixel area) and reasonable low number of read-out channels.

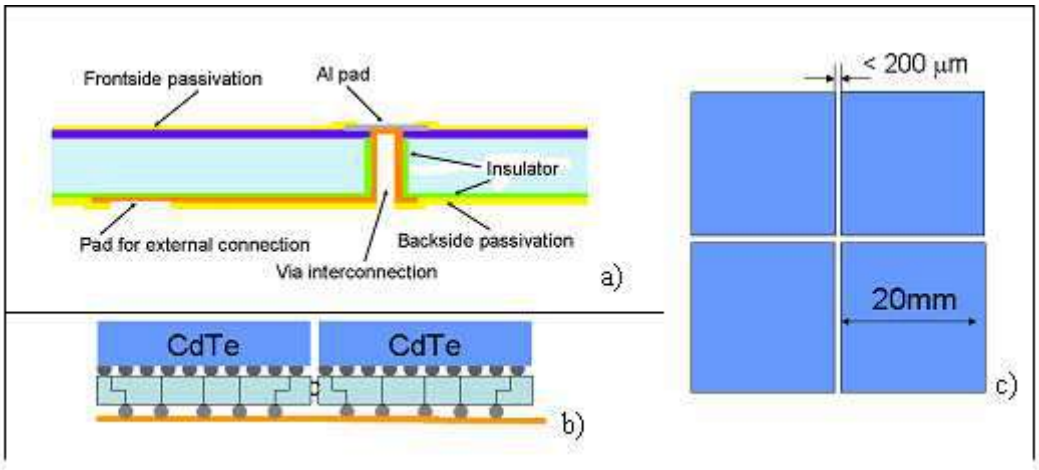

Figure 4-24: a) An interconnection via through the ASIC; b) Bump-bonded outline of the CdTe+ASIC modules; c) The 2×2 array of the CdTe hybrid modules for the NHXM spectral-imaging cameras.

4.5.2 Thecnological developments

A first CdTe+ASIC hybrid module has been realized at the INFN-Pisa laboratories. The module has been used to check the yield of the CdTe sensors production, the yield of the bump-bonding technology, the feasibility of a linear array (2×1) hybrid module.

Schottky CdTe crystals with the smallest available pitch (80μm) have been produced, according to our design and requirements (118604 hexagonal pixels over an area of (25x28 mm^2), by ACRORAD Co. Ltd (Okinawa), a Japanese company leader in manufacturing of CdTe semiconductors. Figure 4-25 shows a micro photography of a CdTe crystal edge. The crystal surface is brown while the dark blue region is the overlap of the SiO2 passivation on top of the crystal. The pad metallization is light blue. The 20μm bump bonding opening through the passivation, hardly visible in the photo, is marked with a dotted circle. At the crystal edges a guard ring stops the leakage current.

The hybrid module has been obtained by bump bonding the Aluminum pads of the crystal to the pixels of a dedicated ASIC (PIXI) of large area (25´28 mm2) developed in our laboratory. Each pixels of the custom ASIC incorporates a full electronic chain which includes a charge-sensitive shaping amplifier followed by a threshold discriminator and a 15-bit shift register. The top metal layer of the PIXI ASIC is patterned with a honeycomb layout of 600×800 pixels at 40 μm pitch, half the pitch of the CdTe sensor.

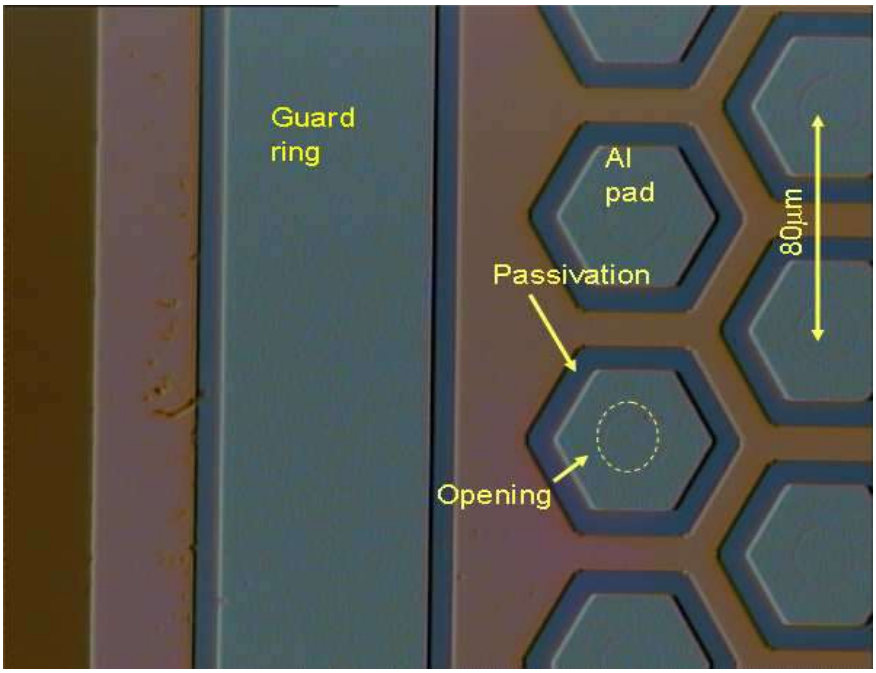

Figure 4-25: Micro photography of a Schottky CdTe crystal border

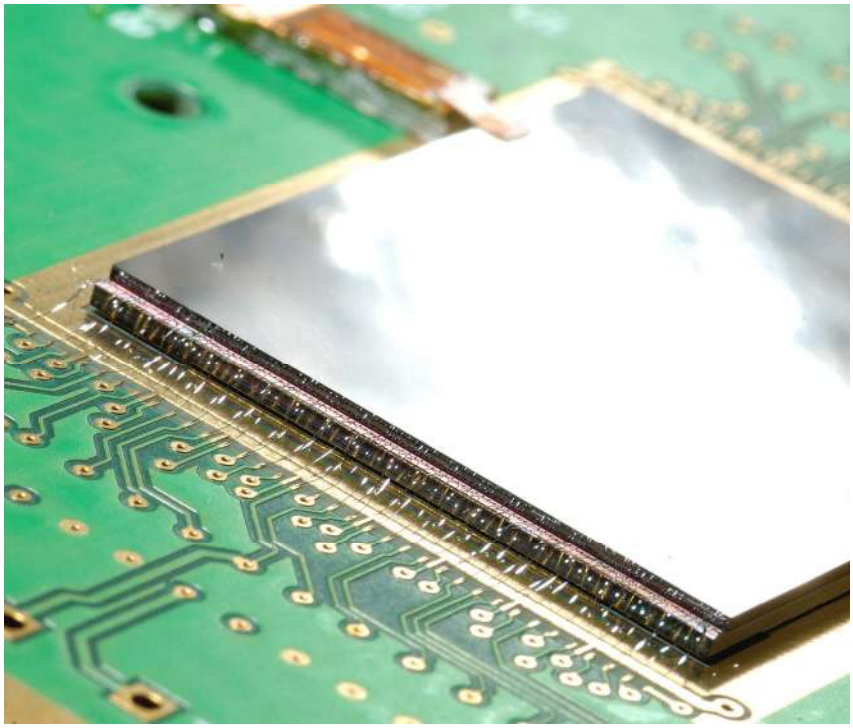

Figure 4-26: The CdTe crystal bump bonded to the custom VLSI ASIC (PIXI).

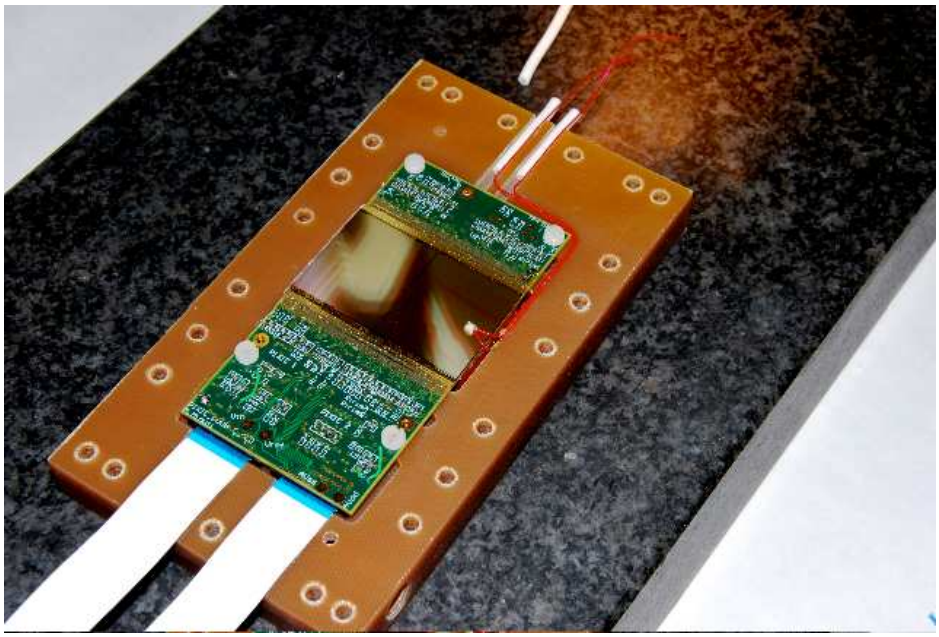

Figure 4-27: A 2×1 linear hybrid module mounted onto the motherboard PCB.

The bump-bond processing have been made by AJAT, a Finnish Microelectronics Company, specialized in this technology. The technological steps in the assembly of the CdTe hybrid module is particularly complex due to the large number of connections to be realized. The yield depends on the optimization of many parameters in the process and on the geometric characteristics of the two parts to be connected (planarity, thickness,….). Nevertheless, a fraction of good connections around 99% has been achieved. The ASIC here described has the distinctive feature to have the wire-bonding connections to the read-out and control electronics evenly distributed on two opposite sides only. This fact has allowed the implementation of a linear array of two detector modules, side by side (see Figure 4-27) with minimum dead space between them.

4.5.3 The CdTe pixel detector: first prototype

The performance of the CdTe pixel detector for the spectral-imaging cameras of NHXM has been tested on a first prototype based on the existing ASIC analog (XPOL) developed in the INFN-Pisa laboratories and used for the X-ray polarimeter.

XPOL is a self-triggering CMOS analog chip with hexagonal pads organized in a 300×352 matrix on the top metal layer. The pads are arranged according to a honeycomb layout at 50 μm pitch. Each pad is connected to a complete electronics chain (charge preamplifier, shaper, sample&hold) realized in the underlying layers of the chip. XPOL has been fabricated in 0.18 μm VLSI technology and has total active area of 15×15 mm^2 with a pixel density of 470/mm^2. It can work in asynchronous way and generates the information of the Region Of Interest (ROI) containing the channels over threshold that have set up the auto-trigger signal. The self-triggering function in fact includes an on-chip signal processing for the automatic localization of the event.

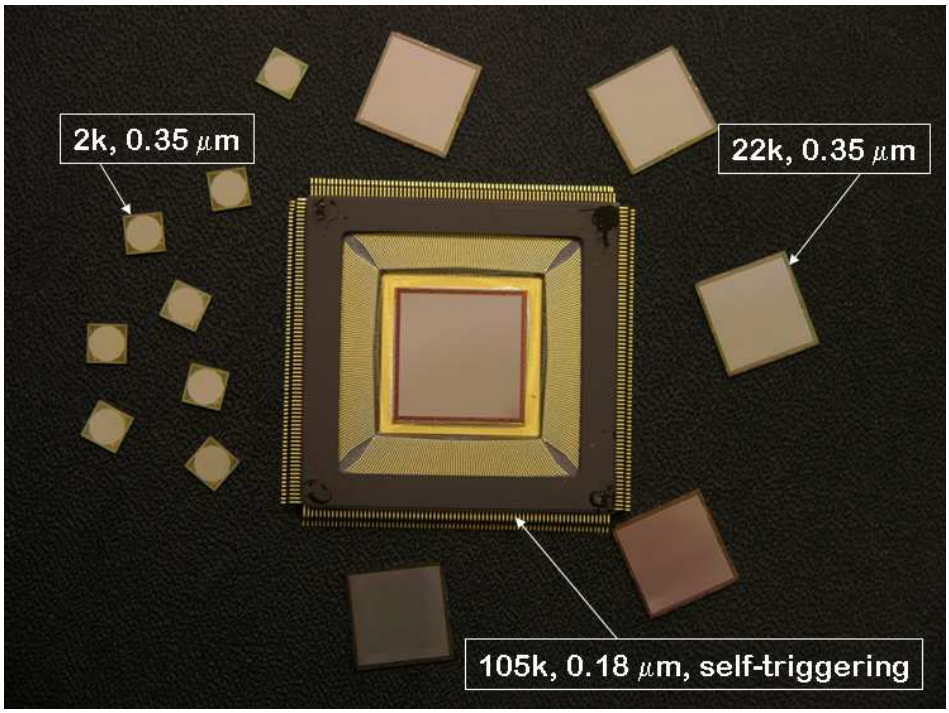

Figure 4-28: the XPOL ASIC in its ceramic package (304 pins) in comparison with the three previous analog chip generations

Pixel noise:	50 electrons ENC
Full-scale linear range:	30000 electrons
Peaking time:	3-10 ms, externally adjustable
Read-out clock:	up to 10MHz
Frame rate:	< 10 kHz (event window)
Parallel analog output buffers:	1, 8 or 16;
Trigger (4 pixel mini-cluster):	Self-trigger
Trigger threshold:	< 2000 e^-
Fill fraction:	92% metal to active area ratio

Table 4-4 The XPOL ASIC main characteristics

The XPOL read-out can be accomplished in single pixel direct addressing way or in sequential mode within 8 (or 16) maxi-clusters, within a self-trigger defined ROI (OR of all triggered mini-clusters) or within the full matrix of pixels. Figure 4-28 shows the XPOL ASIC together with the previous generations of analog ASICs developed in our INFN-Pisa laboratory. Table 4-4 lists the main characteristics of the ASIC. 1 mm thick CdTe crystals have been fabricated for us by ACRORAD. The CdTe design parameters are: active area of 15.03×15.27 mm2 to fit the dimensions of the XPOL ASIC, pixel pitch of 200 μm and matrix layout of 86×73 pixels. Only one XPOL pixel every 16 will be bump-bonded the CdTe pixels. In Figure 4-29 the matrix layouts of the CdTe crystal and XPOL are overlapped and the bump-bonding scheme (red dots) is shown.

The CdTe pixel detector is mounted on the readout board housing a FPGA that sends commands and control signals to the ASIC, reads the flash ADC and performs pedestal subtraction of the readout channels. A USB 2.0 interface is used for the connection to the main computer. The hybrid temperature (T< -20°C) will be controlled by a Peltier cooler and thermostated by a liquid cooler. A hermetic box filled with N_2 flow prevents the condensation. Figure 4-30 shows a schematic of the CdTe detector assembly. The results of the functional tests carried out on the detector are reported hereafter.

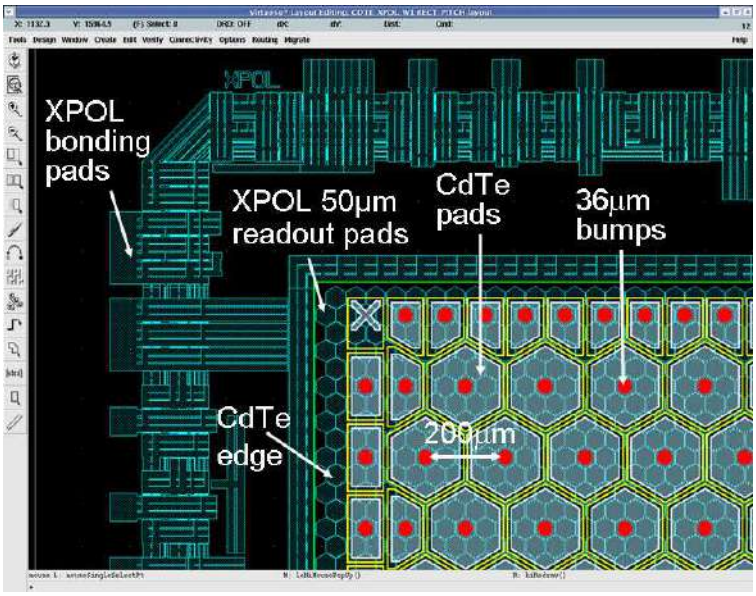

Figure 4-29 Bump-bonding scheme of the CdTe pixel detector

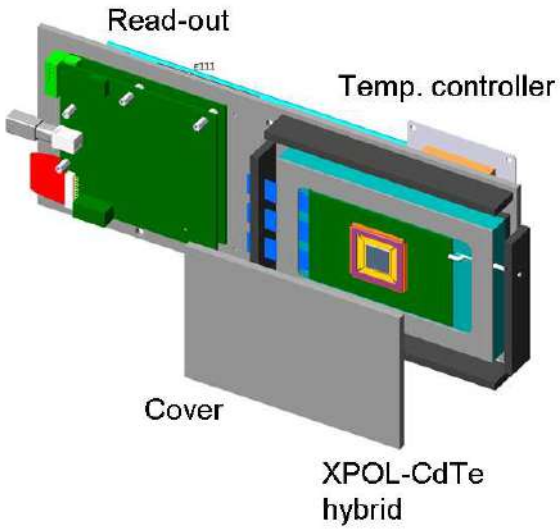

Figure 4-30 Schematics of the CdTe detector assembly

4.5.3.1 Prototype test results

The readout electronics used during the prototype test campaign has an USB computer interface. On the readout board there is a FPGA that sends the commands to the ASIC, reads the flash ADC and performs the direct pedestal subtraction of the channels.
The Thermal Control system is composed of the following items:

- PC water cooling system (Coolit) together with a multistage cascade Peltier;
- ON/OFF control of the Peltier using NI USB modules;
- an insulated hermetic box with N_2 flow prevents the condensation;

The above cooling system has been sized to reach a Tmin = -40°C. It's worth noticing that a Tmin< -50°C determining better performance can be reached using a phase change or a liquid chiller+Peltier.

The first tests has been carried out using an Am^{241} source.
Taking into account only the single-pixel events, we have measured at 60 keV a FWHM = 0.74 keV (see Figure 4-31) which is better than the energy accuracy requirement (1 keV).
This energy resolution corresponds to the quadratic sum of the ENC=50el rms of the electronics and of the CdTe statistical resolution assuming an electron-hole production energy W=4.45eV and a Fano factor f=0.15.
The XPOL electronics was designed as anodic pixel readout of a Gas Pixel Detector equipped with a Gas Electron Multiplyer operated at low gain with a typical 20% energy resolution. An injection signal can be sent to the amplifiers, but the coupling is not precise. Furthermore, we have observed a 10-20% non-linearity of the channels that cannot be corrected with the required precision using the Am241 source alone, which has a spectrum with a large gap between the 59.54keV peak (gamma full absorption peak) and the 36.37 peak (kα escape peak). Thus we have obtained an effective rejection of the events with some energy loss from the pixel, just asking no relevant signals from the channels around.
The single channels events are about 30% of the total events, the events with 2 channels are the more frequent (40%). The calibration errors cause a degradation of the energy resolution of the events with 2 channels over threshold (1.7keV) and with 3 channels (3.6keV). This result clearly indicates that the 0.2mm pitch we had to use in this assembly is too small. The HED pixel will be >0.3mm.
The instability of the 60keV peak was good, <0.1keV/day, even if the lab environment was not very stable. The 0.74keV energy resolution obtained for the single channel events and the good stability, prove that the pixel CdTe detector with an optimized electronics can reach the NHXM requirements..

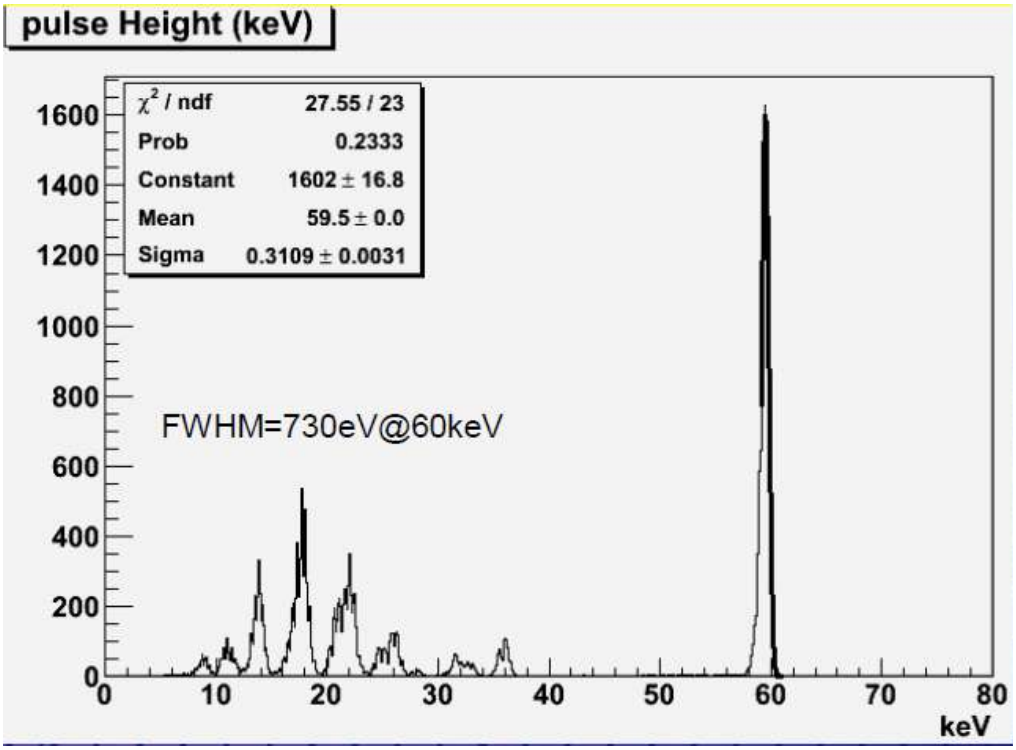

Figure 4-31: the energy spectrum of an Am241 source obtained considering only the 1-pixel events

4.5.4 Electrical Design

The architectural design of the electronics is very similar to the chain used for the polarimeter. The new ASIC will be a special edition of the XPOL ASIC, preserving the main characteristics (low noise, autotrigger capability, ROI) with specific adaptations (pitch, larger signal dynamics) The FE ASIC sends the hold signals to a Back End Electronics (BEE). The BEE digitized the signals, executes a zero suppression and send the data to the DSP. The BEE receives the commands from the DSP and communicates with the FE ASICs. The BEE assign the time stamp to the events. To limit the noise sources, the BEE must stay close to the CdTe detector.

The CdTe+ASIC power is estimated in 8Watt, the BEE needs 12Watts.

4.5.5 Mechanical Design

Particular care is needed to model the thermal load of this detector that operates at -20°C in close proximity to the Si detector that will operate in the -40°C,-60°C range. The two systems are separated by few cm but they must be thermally insulated to avoid large thermal power dispersions.

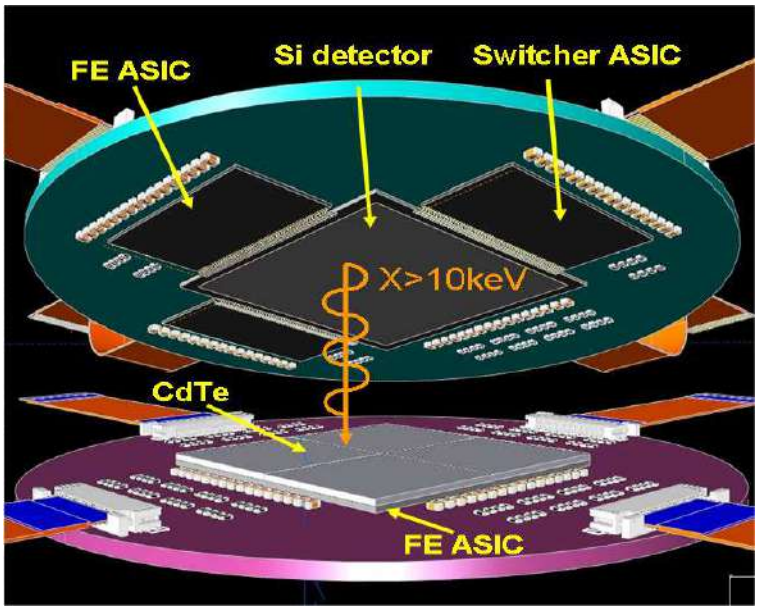

Figure 4-32: Exploded view of the hybrid detector system. The active pixel Si detector operating at -40°C,-60℃ is on top the CdTe pixel detector at -20°C working temperature

However the mechanics of the detector itself is quite simple: the CdTe hybrids are mounted on a ceramic PCB supported by a rigid frame that ensures the rigidity during the launch and the thermal path of the power dissipated by the ASICs. Figure 4-32 shows an artistic view of the LED over the HED.

The mass budgets are few hundreds grams for the detector and less than 2kg for the BEE.

4.6 Shielding System

The active shielding of the camera is formed by an envelope of organic scintillating ribbon fibers produced by BICRON and by an envelope of inorganic scintillator (TBD). The role of the active shielding is to reject the pass-through charged particles while the function of the passive shield is to absorb most of the photons and low energetic particles. Given the low inclination orbit and the mission scientific requirement of having a very low background, an active layer of inorganic scintillators would provide a better background rejection in particular above 10 keV. Therefore, the camera design combines the use of an inorganic anticoincidence layer to be coupled with the HED and scintillating fibers, necessary for the LED whose dead-time would be too big if coupled with inorganic scintillators, and can add some additional rejection capability to HED, beside that one coming from inorganic anticoincidence and pulse height.

4.6.1 Active Shielding

Figure 4-1 shows the schematic of a portion of the layout of scintillating ribbon fibers coupled with the passive shielding. These layers surround the camera as shown in Figure 4-3. The rationale for such configuration is to provide an anticoincidence system to the focal plane detectors with positional sensitivity capability. The MIP (Minimum Ionizing Particle) detectable energy can be estimated as follow.

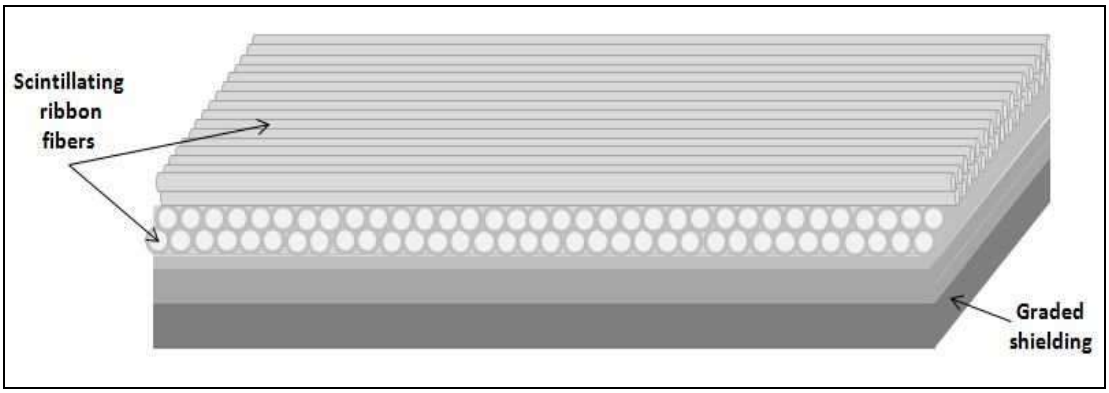

Figure 4-33: Schematic of a portion of the passive and active shielding. The graded shielding and the two orthogonal double-layer ribbon scintillating fibers surrounding the focal plane detectors. The fibers are the items closest to the detectors.

Let npe be the number of photoelectrons produced at the PMT photocathode, for the proposed configuration, it is determined by:

$$n_{pe}$$

where QE(λ) is the H9530-01 Hamamatsu MAPMT quantum efficiency, ES(λ) is the emission spectrum of the selected fiber, TE is the fiber trapping efficiency (~ 4%), TL is the minimum track length of the particle in the fiber calculated with a MonteCarlo code (0.36 mm), PY is the fiber photon yield (~ 8000 photons/MeV) and dE/dX is the lowest energy deposit in the polystyrene (2 MeV/cm).

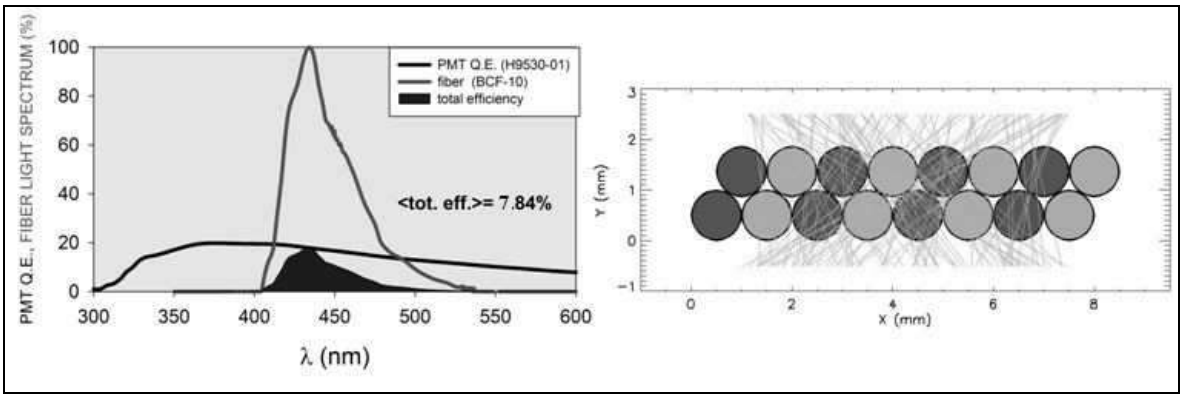

Figure 4-34: . On the left the average efficiency resulting by convoluting the PMT quantum efficiency and the fiber emission spectrum. On the right an example of the MonteCarlo simulation output for track length determination.

On the left of Figure 4-34 it is shown the average total efficiency of PMT QE convoluted with BCF-10 fibers emission spectrum. The resulting number of photoelectrons n_{pe}, about 2, is likely to be detected by using Single

Photon Counting front-end. As a consequence of that, the MIP (Minimum Ionizing Particle) detectable energy results as low as 200 keV.

To detect the light produced by the fiber when crossed by a particle we use a set-up shown in Figure 4-35 (conceptual scheme).

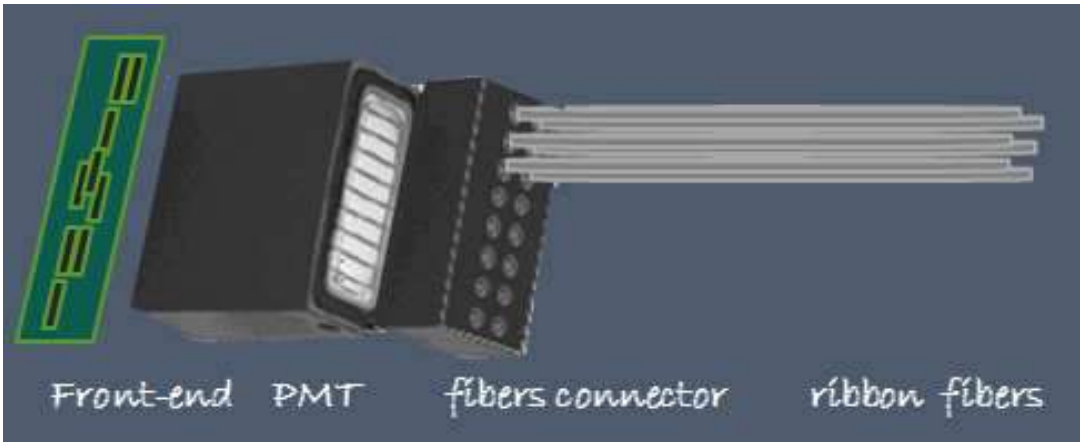

Figure 4-35: Fibers read-out conceptual scheme

The read-out ends of the fiber ribbons are bundled in pairs and optically interfaced to the pixels of linear array multi-anode photomultipliers by means of a plastic collector. A front-end electronics, based on single photon counting, discriminate the analog signals and convert them in digital signals. The digital signals are then send to a FPGA that determines the event-trigger and identify the pre-set region of interest that is constitute by the geometrical intersection of any track-like formed by two or more position on the fibers and the active area of the HED detector. The resolving time for such operations is estimated to be of the order of 50 ns.

4.6.2 Passive Shielding

For the passive shielding, a graded configuration composed by 1.5 mm of Tantalum, 2.2 mm of Tin, 0.48 mm of Copper, 0.27 mm of aluminium and 0.1 mm of Carbon has been used. However, depending on the final anticoincidence configuration (organic + inorganic), others materials and/or different thickness could be used and studied in order to minimize the mass.

4.6.3 Collimator

As already reported in section 4.1, the collimator dimensions are: 0.9-1 meter long and 75 mm diameter wide. Also the collimator will probably have an active shielding. Moreover, it could be convenient to have a collimator shape with a squared section (instead of a round section) in order to have maximum stiffness and minimum mass. Figure 4-36 shows the preliminary results of modal analysis carried out for a squared section collimator lined with passive shielding as defined in section 4.6.2.

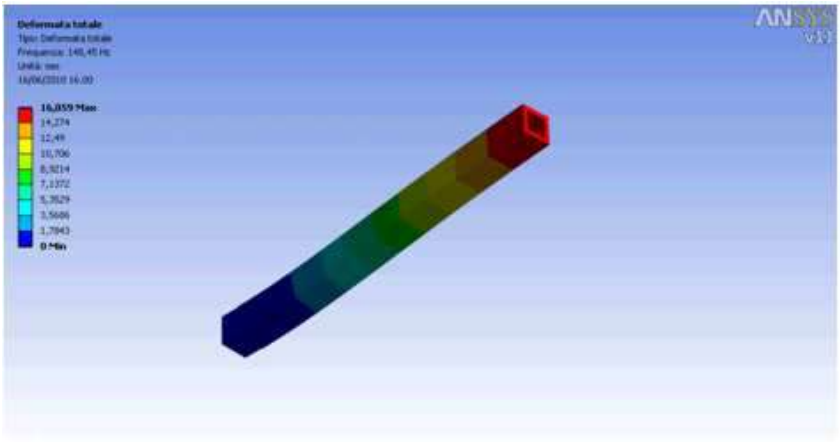

Mode	Frequency [Hz]
1	148
2	148
3	555
4	555
5	1166
6	1222

Figure 4-36: Modal analysis of the squared section collimator

4.7 Thermal Control

The CCD-based LED detector configuration requires active cooling in order to achieve the -80 ºC (goal is -60 ºC) operating temperature and this is achieved by use of a peltier cooler. Heat from the hot side of the cooler is conducted to the camera coldfinger interface on the rear of the camera via thermal links that are routed around the HED (see Figure 4-37). Based on experience of similar cooling requirements and interface temperatures, a two-stage peltier cooler is envisaged, with a power requirement of approximately 10 watts.

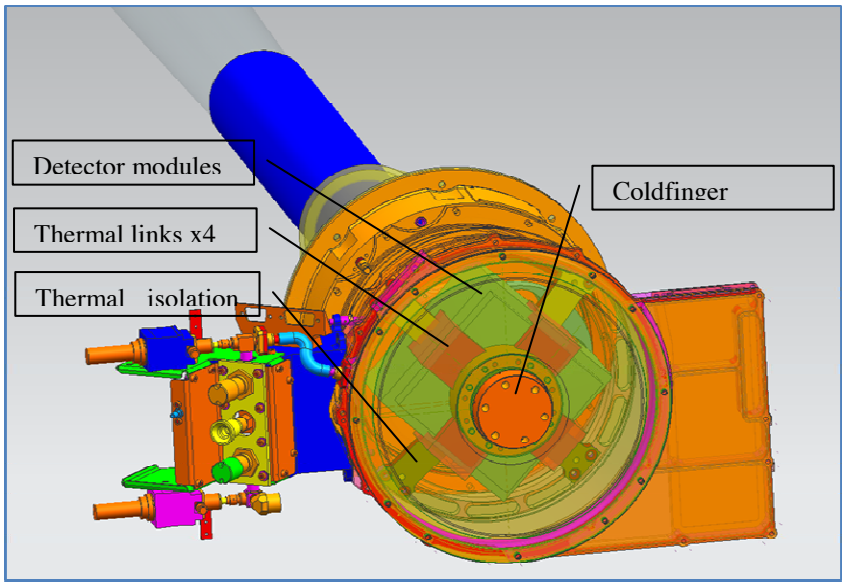

Figure 4-37 The camera coldfinger interface on the rear of the camera

The HED thermal interface will be made at the hot side of the TEC by attaching to the thermal links, or directly to the LED module. For a nominal cold finger temperature of -40 ºC, the HED operation temperature of -20 ºC will be easily achieved. A small amount of heater power (~1W) may be required to provide temperature stability of the HED.

4.8 Vacuum System

As shown in the Figure 4-3, Figure 4-4 and Figure 4-5 the camera design hosts the inlet/outlet connectors that act as escape-release gas filling valve. However, the complete operational mode and the vacuum system requirements have to be defined.

4.9 Filter Wheel

In order to select the X-ray transparency and UV-Visible light rejection appropriate to the various science cases, it is advisable, if compatible with the mission constraints, to have a focal plane filter wheel. If the baseline design configuration for the thermal shield is adopted, the filter wheel must have at least the following positions:

1 – open

2 – closed

3 – filter 1

4 – filter 2

5 – Calibration source

The structure of the filters may be the same as the thermal shield (i.e. Al coated polyimide) and the thickness is TBD on the science case base (see also section 3.4). It should be noted that an appropriate design of the filter wheel will probably allow us to allocate one more position with basically no increase in the wheel size. If this turns out to be the case, a 3rd filter will be allocated.

4.10 Main Simulation results

In this section the main results related to the *optimization studies of geometry and chemical composition of NHXM active and passive shielding* and the *background count rate and spectra evaluation* are reported.

In order to fully characterize the LEO radiation effects on the shielding and detector response, we developed 4 models, of increasing geometrical complexity from the simplified slab structure, through the box shaped shielding surrounding the detector plane, to a more realistic complex geometry that take into account all the hardware components of the detectors. We call these models: slab, box, NHXM001, NHXM003 geometries.

4.10.1 Sources of background

The sources of "prompt" (not due to delayed events) background expected in a LEO, low inclination orbit, and used as input in the Geant4 simulation, are:

- Cosmic X-ray Background (CXB);
- Earth X-ray Albedo;
- primary (Cosmic Rays) and albedo protons;
- albedo electrons;
- albedo positrons.

The spectral distribution of the particles used as input in the present background evaluation is plotted in Figure 4-39.

4.10.1.1 Photonic component

The CXB flux, with an energy density peaking in the 20-40 keV energy band, is simulated from 1 keV to 100 MeV, using the spectral shape of [1]. The CXB and Cosmic Rays (CR) flux is significantly shielded by the Earth, which, for a 550 km altitude spacecraft, covers about the 30% of the sky. The Earth atmosphere, on the other hand, emits in the X-ray band because of the CXB reflection by the atmospheric upper layers and as induced by CR interactions [2].

Figure 4-38 (left panel) shows a collection of the Earth X-ray albedo observations from literature (extended up to 1 MeV), expressed in terms of surface brightness: the continuous red and green lines model the INTEGRAL observation (*Churazov E. et al., "INTEGRAL observations of the cosmic X-ray background in the 5–100 keV range via occultation by the Earth", 2007, A&A, 467, 529; Turler M. et al., "INTEGRAL hard X-ray spectra of the cosmic X-ray background and Galactic ridge emission", 2010, A&A, 512, 49*), the blue line refers to the Swift/BAT observation (*Ajello M. et al., "Cosmic X-ray background and Earth albedo spectra with SWIFT BAT", 2008, ApJ, 689, 666*) while the black line shows the CXB flux for comparison.

Since the CXB flux is isotropic, the intensity of its reflection does not depend on the telescope point of view. The CR flux, instead, is energetically cut off by the Earth magnetic field, with a lower energy (geomagnetic rigidity) that depends on the field intensity. From high (~60 deg.) to low (~20 deg.) latitudes in the near-Earth region, the energy cut off ranges from ~100 MeV to ~10 GeV. As a result, the Earth X-ray albedo intensity decreases from polar to equatorial observations, as shown by the gap between the INTEGRAL (~50 deg. Inclination orbit) and the BAT (~20 deg. inclination orbit) albedo intensity in Figure 4-38 (left panel). The CR induced albedo equation developed by [6] can be used to model the Earth X-ray albedo as seen from NHXM, i.e. for an equatorial, 550 km high orbit. Figure 4-38 (right panel) shows the computed total X-ray albedo, for a minimum solar activity, as seen from a 0 deg. (NHXM, red line) and 20.6 deg. (Swift, blue line) inclination orbit, while the dotted black line refers to the modelled CXB reflection and the continuous black line to the Swift/BAT observation. Since the BAT model (blue line) reproduces with good accuracy the real spectrum (black line), the NHXM X-ray albedo (red line) can be assumed as model in the background simulation.

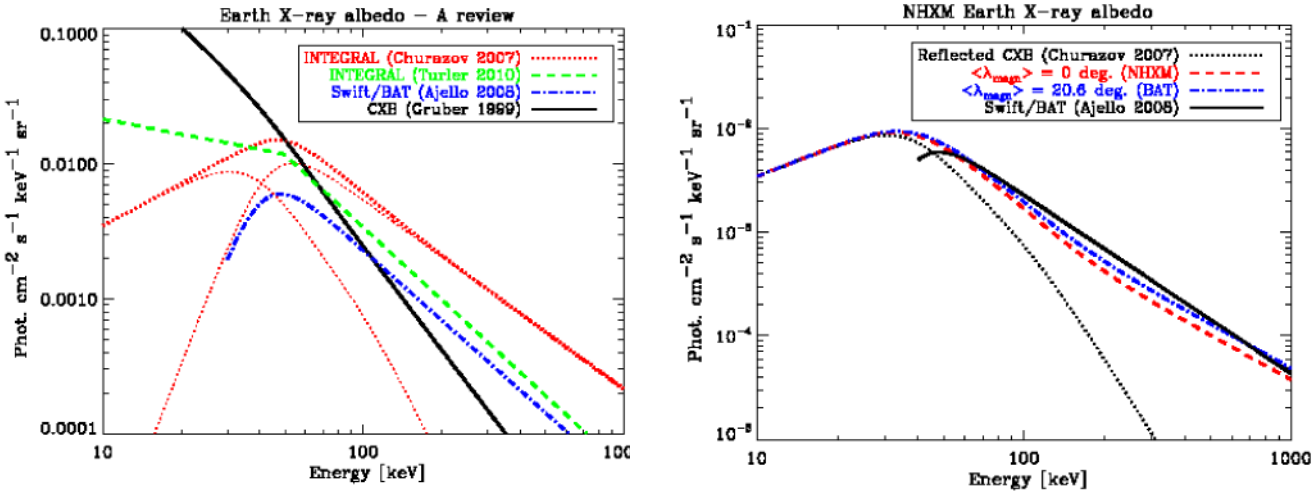

Figure 4-38: Left*: Earth X-ray albedo as observed by INTEGRAL (red [2] and green [3] line) and Swift/BAT [4], while the dotted red lines show the decomposition in CXB reflection and CR interactions for the [2] observation and the black line is the CXB flux for comparison.* Right*: total X-ray albedo computation for NHXM (red line) and Swift (blue line) orbit; the latter is shown in comparison with the real Swift/BAT observation (red line), while the dotted black line refers to the CXB reflection, which contributes to the total computed albedo.*

4.10.1.2 Charged particles component

Since the galactic CR flux is composed of about 98% nuclei (87% Hydrogen, 12% Helium and 1% heavier nuclei) and 2% leptons (>90% electrons) (*Simpson J. A., "Elemental and Isotopic Composition of the Galactic Cosmic Rays", 1983, Ann. Rev. Nucl. Part. Sci., 33, 323; Adriani O. et al., "Positrons and Electrons in Primary Cosmic Rays As Measured in the PAMELA Experiment", 2009, Bulletin of the Russian Academy of Sciences, 73, 568*), the contribution of primary electrons and positrons to the background is neglected.

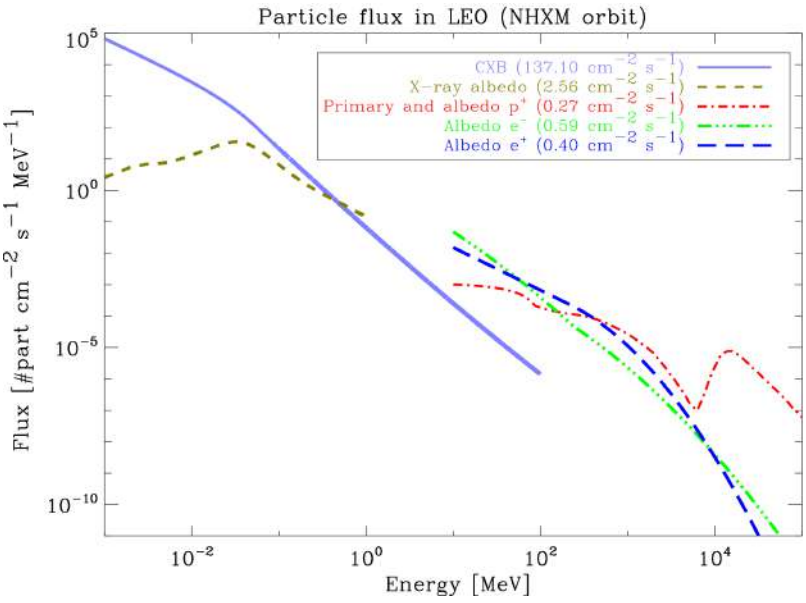

Figure 4-39 Overview of the simulated space radiation environment, normalized for the subtended solid angle. Light blue*: CXB (1 keV – 100 MeV);* Olive green*: Earth X-ray albedo (1 keV – 1 MeV);* red*: primary and secondary protons (10 MeV – 100 GeV);* light green*: albedo electrons (10 MeV – 80 GeV);* dark blue*: albedo positrons (10 MeV – 80 GeV).*

The simulated proton flux is the sum of the primary CR and the secondary albedo protons induced by CR interactions with the atmosphere, as observed by the AMS (*Alcaraz J. et al (AMS collaboration), "Protons in near Earth orbit", 2000, Phys. Lett. B, 472, 215)* in June 1998 during solar minimum (modulation parameter Φ = 400 MV according to *Wiedenbeck M.E. et al, "The Level of Solar Modulation of Galactic Cosmic Rays from 1997 to 2005 as Derived from ACE Measurements of Elemental Energy Spectra", 2005, International Cosmic Ray Conference Pune, 00, 101*). The geomagnetic rigidity for a magnetic latitude of 5 deg. (the Earth equator) and an altitude of 550 km is about 15 GV (at solar minimum), resulting, following the computation of *Gehrels N., "Instrumental background in gamma-ray spectrometers flown in low Earth orbit", 1992, NIM-A, 313, 513*, in a lower energy cut off of 14 GeV for protons. Below this energy, the albedo charged particles flux arises, as a consequence of CR interaction with air nuclei initiating nuclear interactions cascades with the final result of producing secondaries protons, electrons and positrons at relatively low energies.

These secondary charged particles are usually classified in splash, or leaking, albedo if emerging from the atmosphere, while the term reentrant albedo denotes downward moving particles below the geomagnetic cut off, travelling backward along the magnetic field line connected to the point of observation. There is also a fraction of secondary particles that can remain trapped for several years, bouncing several times in the magnetic field. The intensity of splash and reentrant albedo is expected to be of the same order (*Alcaraz J. et al (AMS collaboration), "Protons in near Earth orbit", 2000, Phys. Lett. B, 472, 215*), especially at low latitudes. For this reason, albedo protons, electrons and positrons are simulated isotropically from 4π sr. Since primary and

secondary protons are simulated as unified flux, the CR flux is simulated without taking into account the Earth shielding.

4.10.2 Slab geometry

Given the simplified set-up for the geometry and the input background distribution, the slab model is not conceived to represent the physical background at the detector but to provide a quick comparison of background rejection in different configurations. The model is designed as a multilayer slab where consecutive elements represent the passive and active shielding above the detector plane. Primary background particles normally illuminate the slab with planar angular distribution. Simulations have been carried out for all background components.

4.10.2.1 Model set-up

The slab geometry is modeled as follows and described in **Errore. L'origine riferimento non è stata trovata.**:

- Polystyrene layer (AC) of 3.8 mm thickness. Most simulations do not consider active rejection.
- Passive shielding graded with a main absorber made of Tantalum. The thickness and composition of each layer is listed inTable 4-5.
- Detector plane: the bottom layer of the model is occupied by LED and HED, separately. LED is designed as a Si layer of 0.45 mm thickness, HED is a CdTe slab of 1.5 mm. Both detectors are not-pixellated volumes of planar dimensions 57x57 mm.

Material	Z	Kα, Kβ [keV]	t [mm]
Tantalum (Ta)	73	57.5, 65.2	1.5
Tin (Sn)	50	23.5, 28.5	2.2
Copper (Cu)	29	8.1, 8.9	0.48
Aluminum (Al)	13	1.5, 1.6	0.27
Carbon (C)	6	0.28, /	0.1

Table 4-5: Materials and thicknesses of the graded passive shield.

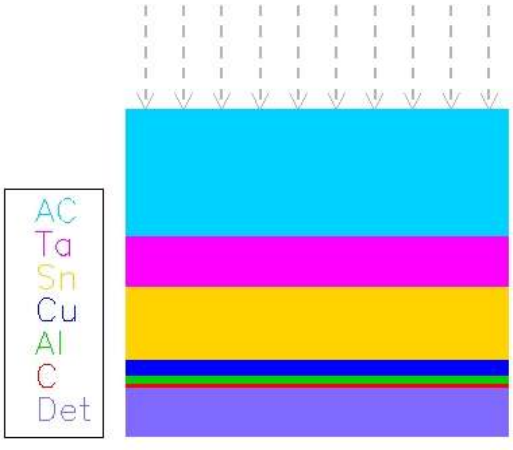

Figure 4-40: Slab geometry.

Simulations have been carried out for the following geometry configurations:

- case A: with respect to the incoming background the slab is ordered as AC + grading system + detector.
- case B: the AC layer is placed between the grading system and the detector plane.
- case C: same as case B without the Carbon layer in the grading module.
- case D: same as case C with the Tin layer reduced to 1.1 mm. At present the configuration D has been considered for CXB and proton input only.

An active background rejection has been switched on for simulations with HED in all but D geometrical cases for proton and electron input. The explored threshold levels are set to 10 keV, 100 keV and 1 MeV.

An event is rejected when an energy deposit at the detector corresponds to a deposit in the AC with energy above a selected threshold. Note that one single event in each slab is the total energy deposit, that is integrated over all secondary processes generated by the same primary event.

4.10.2.2 Total background

For each geometrical case and primary input source we collect the background counts at the detector in the operational energy range, defined as 0.2-10 keV for LED and 5-100 kev for HED.

The total background counts per input particle are given in Table 4-6.

Background counts				
	LED Energy range		HED Energy range	
	0.2-10 keV		5-100 keV	
Geom.	N input	Counts/inp	N input	Counts/inp
CXB				
A	$3.9\ 10^{8}$	$17.7+-\ 0.7\ 10^{-7}$	$5\ 10^{7}$	$5.0+-\ 0.1\ 10^{-5}$
B	$6\ 10^{8}$	$17.6+-\ 0.5\ 10^{-7}$	$5\ 10^{7}$	$4.9+-\ 0.1\ 10^{-5}$
C	10^{8}	$17.2+-\ 1.3\ 10^{-7}$	$5\ 10^{7}$	$5.0+-\ 0.1\ 10^{-5}$
D	$1\ 10^{8}$	$19.6+-\ 1.4\ 10^{-7}$	$5\ 10^{7}$	$5.4+-\ 0.1\ 10^{-5}$
Albedo				
A	$2\ 10^{8}$	$52.7+-\ 0.5\ 10^{-6}$	$2\ 10^{8}$	$126.7+-\ 0.2\ 10^{-5}$
B	$2\ 10^{8}$	$65.0+-\ 0.6\ 10^{-6}$	$2\ 10^{8}$	$154.4+-\ 0.3\ 10^{-5}$
C	$2\ 10^{8}$	$69.1+-\ 0.6\ 10^{-6}$	$2\ 10^{8}$	$165.2+-\ 0.3\ 10^{-5}$
Protons				
A	10^{6}	$4.6+-\ 0.7\ 10^{-5}$	10^{6}	$4.3+-\ 0.2\ 10^{-4}$
B	$3\ 10^{6}$	$3.9+-\ 0.4\ 10^{-5}$	10^{6}	$4.7+-\ 0.2\ 10^{-4}$
C	10^{6}	$5.0+-\ 0.7\ 10^{-5}$	$2\ 10^{6}$	$4.5+-\ 0.1\ 10^{-4}$
D	10^{6}	$3.5+-\ 0.6\ 10^{-5}$	10^{6}	$4.0+-\ 0.2\ 10^{-4}$
Electrons				
A	10^{6}	$10.6+-\ 0.3\ 10^{-4}$	$2\ 10^{6}$	$18.5+-\ 0.1\ 10^{-3}$
B	10^{6}	$10.8+-\ 0.3\ 10^{-4}$	$2\ 10^{6}$	$20.7+-\ 0.1\ 10^{-3}$
C	10^{6}	$11.3+-\ 0.3\ 10^{-4}$	$2\ 10^{6}$	$20.5+-\ 0.1\ 10^{-3}$
Positrons				
A	10^{6}	$7.6+-\ 0.3\ 10^{-4}$	$2\ 10^{6}$	$145.0+-\ 0.8\ 10^{-4}$
B	10^{6}	$8.5+-\ 0.3\ 10^{-4}$	$2\ 10^{6}$	$155.8+-\ 0.9\ 10^{-4}$
C	10^{6}	$8.8+-\ 0.3\ 10^{-4}$	$2\ 10^{6}$	$154.8+-\ 0.9\ 10^{-4}$

Table 4-6: Background counts normalized to the input particle number.

Results:

- with the exception of the X-ray albedo induced background, all geometrical configurations result in a comparable background level on the LED;
- the background simulated on the HED is slightly lower in case A for albedo, electrons and positrons input particles;
- cases B and C are always in accordance within errors (with exception for the albedo input).

4.10.2.3 Background spectra

The simplified geometry allows us to obtain spectra of deposits at the detector as well as at each slab. An example is given in Figure 4-41 showing the counts spectra for CXB prompt input for geometrical case A (left panel) and B (right panel).

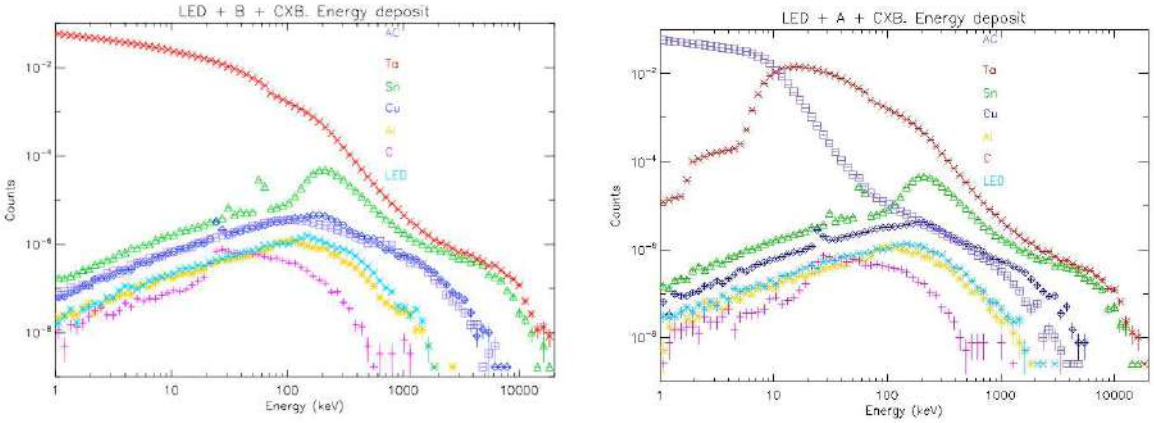

Figure 4-41 Deposit spectra in each layer for geometrical case A (left panel) and B (right panel).

The deposit spectrum at each slab for the CXB input shows fluorescence and/or escape lines of the previous material. The detailed spectrum at LED and HED is given in Figure 5. No appreciable features are visible in both detectors.

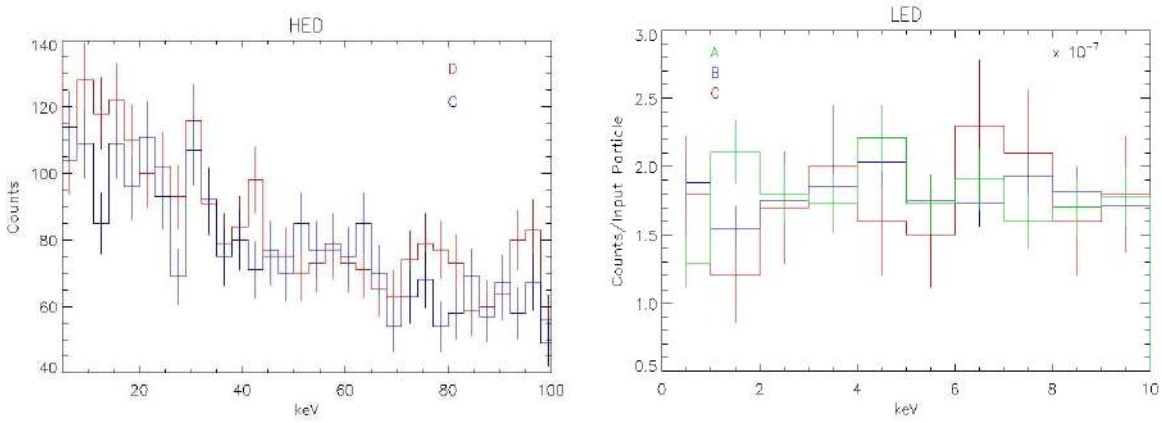

Figure 4-42: Deposit Spectra at LED (left panel) and HED (right panel) for CXB input background.

4.10.2.4 AC ON

The effect of the Anti-Coincidence activation on the spectrum at HED is given in Table 4-7 and Figure 4-43.

The activation of an external AC sensibly reduces the charged particles induced background. The total background decreases with threshold without substantial changes in the spectral shape.

HED – AC ON				
		Threshold		
		10 keV	100 keV	1 MeV
Geom.	N input	Counts/inp	Counts/inp	Counts/inp
Protons				
A	10^6	0.02+- 0.01 10^{-4}	0.02+- 0.01 10^{-4}	0.02+- 0.01 10^{-4}
B	10^6	1.87+- 0.14 10^{-4}	2.15+- 0.15 10^{-4}	3.31+- 0.18 10^{-4}
C	2 10^6	1.76+- 0.09 10^{-4}	2.06+- 0.10 10^{-4}	3.15+- 0.13 10^{-4}
Electrons				
A	2 10^6	< 10^{-6}	< 10^{-6}	162.2+- 0.9 10^{-4}
B	2 10^6	122.0+- 0.8 10^{-4}	132.9+- 0.8 10^{-4}	166.1+- 0.9 10^{-4}
C	2 10^6	121.6+- 0.8 10^{-4}	132.0+- 0.8 10^{-4}	164.9+- 0.9 10^{-4}

Table 4-7: effect of the Anti-Coincidence activation on the spectrum at HED

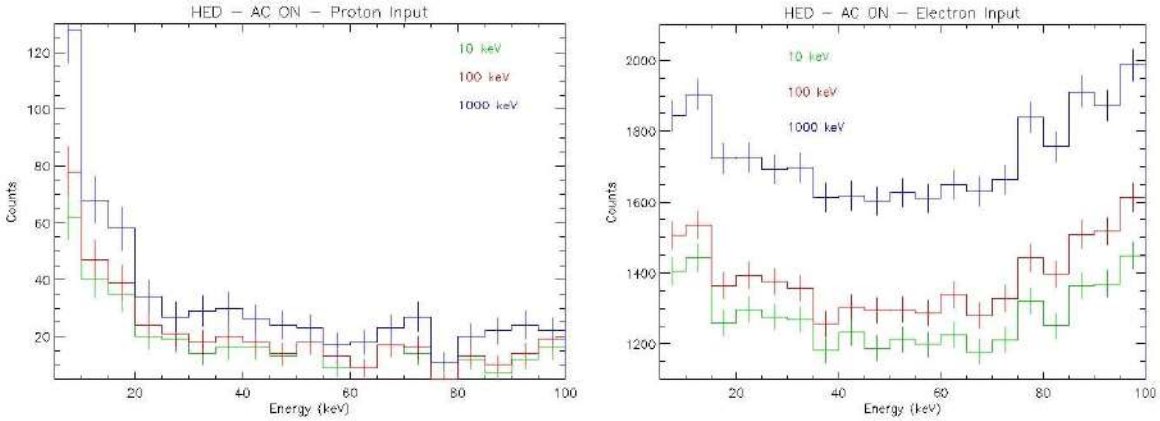

Figure 4-43: Deposit spectra at HED for proton (left panel) and electron (right panel) input with active anti-coincidence at different threshold levels.

4.10.3 Box geometry

The Geant4 camera geometry model is simplified as a box shaped shielding system surrounding a monolithic LED and HED assembly based on the NHXM focal plane design. Given the simplified geometry, the results presented here are not the expected NHXM background count rate but they represent a first, fundamental step to select the major sources of background and, consequently, to optimize the shielding system. In particular, the anticoincidence (AC) count rate strongly affects the observation dead time for a frame-by-frame detection read out. The baseline shielding concept, already employed in the NHXM001 Geant4 geometry release, is composed by a plastic scintillator (active shield) surrounding a graded passive shielding. In the present work, the background simulation is performed for three shielding configurations:

- Active shielding (plastic scintillator) surrounding the passive shielding (baseline design, defined as Case A);
- Active shielding (plastic scintillator) enclosed by the passive shielding (defined as Case B);
- Active shielding (inorganic scintillator) enclosed by the passive shielding (defined as Case C).

The use of organic scintillators as active shield allows to reduce the mass budget, thanks to the lighter components, with no secondary activation lines and an higher feasibility respect to inorganic (BGO, NaI) anticoincidence systems, which in turn ensure an higher absorption efficiency.

The choice between an organic and inorganic active shield should follow a detailed analysis of the background and AC count rate as a function of the AC threshold, with a parallel comparison of the background spectra. For this reason, the third configuration (Case C) uses an inorganic scintillator as active shield, to be compared to the Case B configuration..

The simulation results are compared with the aim of selecting the active shield design that ensures the best response in terms of background and active shield count rate, given the space radiation environment of the NHXM mission.

The box model is composed by:

- NXHM focal plane: a Silicon Low Energy Detector (LED), 0.45 mm thick, over a CdTe High Energy Detector (HED), 1.5 mm thick.
- Box-shaped active and passive shielding system totally surrounding the focal plane.

The LED and HED are simulated by single, not-pixellated volumes: a 57×57×0.45 mm thick Silicon (Si) layer, the LED, and a 50×50×1.5 mm thick Cadmium Telluride (CdTe) layer, the HED, separated by a 1.2 cm distance. The distance between the detectors and the shielding walls on top and bottom sides is 10 cm, so that the surrounding box height is 21.2 cm, with a side of 25 cm (see Figure 4-44).

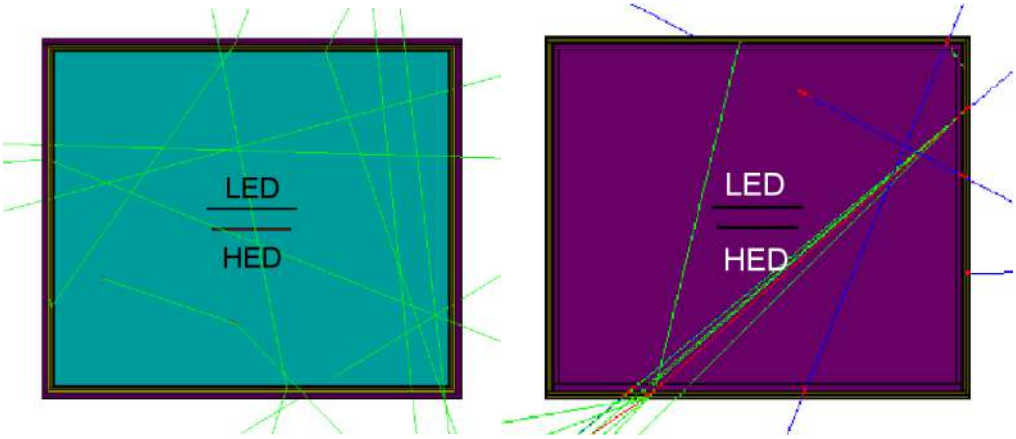

Figure 4-44: Cut view of the Geant4 mass model with the AC surrounding the passive shielding (left panel) and enclosed by the passive layers (right panel). The green, blue and red lines being the trajectories of the interacting photons, protons and electrons respectively.

The materials composing the plastic and inorganic active shielding are Polystyrene and NaI respectively, with a thickness of 3.8 mm for all the studied configurations.

The passive shielding is graded as described in the previous section.

An event is removed if the same primary particles generates an event in the active shield (an energy deposit above the lower energy threshold) and a LED (or HED) count within the detection energy range. All the results presented here refer to an AC threshold of 200 keV.

4.10.3.1 The background in a Box

Background spectra are produced in the 0.5 – 20 keV energy range for the LED and in the 5 – 100 keV energy range for the HED, while the background level is evaluated as the average level of counts per unit of detector area and time along the reported operative energy ranges.

Background levels

AC (plastic) surrounding the passive shield (baseline design):

Case A		Background count rate [cts cm^{-2} s^{-1} keV^{-1}]			
Input	Det.	AC + Passive shield		Triggered counts	AC rate [cts s^{-1}]
		AC off	AC on		
CXB	LED	(1.48±0.11)×10^{-5}	(1.43±0.11)×10^{-5}	3.1%	6.4
	HED	(5.09±0.10)×10^{-5}	(5.00±0.10)×10^{-5}	1.8%	
Protons	LED	(1.53±0.02)×10^{-4}	(0.30±0.10)×10^{-6}	99.8%	185.4
	HED	(2.36±0.01)×10^{-4}	(0.33±0.05)×10^{-6}	99.9%	
Electrons	LED	(1.81±0.04)×10^{-4}	0	100%	411.1
	HED	(4.21±0.03)×10^{-4}	0	100%	
Positrons	LED	(2.10±0.03)×10^{-4}	(0.18±0.09)×10^{-6}	99.9%	273.2
	HED	(4.70±0.02)×10^{-4}	(0.45±0.07)×10^{-6}	99.9%	
X-ray Albedo	LED	(1.14±0.03)×10^{-5}	(1.06±0.02)×10^{-5}	6.9%	5.4
	HED	(3.78±0.02)×10^{-5}	(3.53±0.02)×10^{-5}	6.6%	
Total	LED	(5.68±0.10)×10^{-4}	(0.25±0.09)×10^{-4}	/	881.5
	HED	(1.22±0.01)×10^{-3}	(0.86±0.01)×10^{-4}		

Table 4-8: Background level, in counts cm^{-2} s^{-1} keV^{-1}, the fraction of the triggered events, and the AC count rate, in counts s^{-1}, for the Case A geometry configuration.

Passive shield enclosing the AC (plastic):

Case B		Background count rate [cts cm^{-2} s^{-1} keV^{-1}]			
Input	Det.	AC + Passive shield		Triggered counts	AC rate [cts s^{-1}]
		AC off	AC on		
CXB	LED	$(1.58\pm0.11)\times10^{-5}$	$(1.30\pm0.10)\times10^{-5}$	17.9%	5.5
	HED	$(4.94\pm0.10)\times10^{-5}$	$(4.52\pm0.10)\times10^{-5}$	8.6%	
Protons	LED	$(2.14\pm0.03)\times10^{-4}$	$(0.36\pm0.10)\times10^{-6}$	99.8%	148.0
	HED	$(2.53\pm0.01)\times10^{-4}$	$(0.76\pm0.08)\times10^{-6}$	99.7%	
Electrons	LED	$(2.35\pm0.04)\times10^{-4}$	$(2.69\pm0.13)\times10^{-5}$	88.6%	177.1
	HED	$(4.88\pm0.03)\times10^{-4}$	$(8.77\pm0.12)\times10^{-5}$	82.0%	
Positrons	LED	$(2.69\pm0.03)\times10^{-4}$	$(1.50\pm0.08)\times10^{-5}$	94.5%	178.8
	HED	$(5.33\pm0.03)\times10^{-4}$	$(4.60\pm0.07)\times10^{-5}$	91.4%	
X-ray albedo	LED	$(1.29\pm0.03)\times10^{-5}$	$(1.04\pm0.02)\times10^{-5}$	19.4%	4.4
	HED	$(3.95\pm0.03)\times10^{-5}$	$(3.50\pm0.02)\times10^{-5}$	11.4%	
Total	LED	$(7.47\pm0.11)\times10^{-4}$	$(0.66\pm0.04)\times10^{-4}$	/	513.8
	HED	$(1.36\pm0.01)\times10^{-3}$	$(2.15\pm0.03)\times10^{-4}$		

Table 4-9: Background level, in counts cm^{-2} s^{-1} keV^{1}, the fraction of the triggered events, and the AC count rate, in counts s^{-1}, for the Case B geometry configuration.

Passive shield enclosing the AC (NaI):

Case C		Background count rate [cts cm^{-2} s^{-1} keV^{-1}]			
Input	Det.	Passive shield + AC		Triggered counts [%]	AC rate [cts s^{-1}]
		AC off	AC on		
CXB	LED	(1.71±0.16)×10^{-5}	(1.06±0.13)×10^{-5}	38.4%	35.0
	HED	(4.75±0.14)×10^{-5}	(3.38±0.12)×10^{-5}	28.8%	
Protons	LED	(1.80±0.04)×10^{-4}	(0.20±0.14)×10^{-6}	99.9%	148.1
	HED	(2.69±0.03)×10^{-4}	(0.64±0.13)×10^{-6}	99.8%	
Electrons	LED	(1.88±0.11)×10^{-4}	(0.66±0.21)×10^{-5}	96.5%	247.4
	HED	(4.41±0.09)×10^{-4}	(2.84±0.22)×10^{-5}	93.6%	
Positrons	LED	(2.49±0.10)×10^{-4}	(0.44±0.14)×10^{-5}	98.2%	216.0
	HED	(5.55±0.08)×10^{-4}	(1.71±0.14)×10^{-5}	96.9%	
X-ray albedo	LED	(1.19±0.04)×10^{-5}	(0.70±0.03)×10^{-5}	40.8%	25.6
	HED	(3.65±0.03)×10^{-5}	(2.35±0.03)×10^{-5}	35.7%	
Total	LED	(6.46±0.28)×10^{-4}	(0.29±0.05)×10^{-4}	/	672.1
	HED	(1.35±0.02)×10^{-3}	(1.03±0.05)×10^{-4}		

Table 4-10: Background level, in counts cm^{-2} s^{-1} keV^{-1}, the fraction of the triggered events, and the AC count rate, in counts s^{-1}, for the Case C geometry configuration.

Background spectra

The background spectra as obtained with a plastic AC placed inside the passive shielding (Case B) are presented in Figure 4-45. The total level, given by the sum of all the simulated sources, is shown in black. For a comparison of the three-tested configuration, see the following Section.

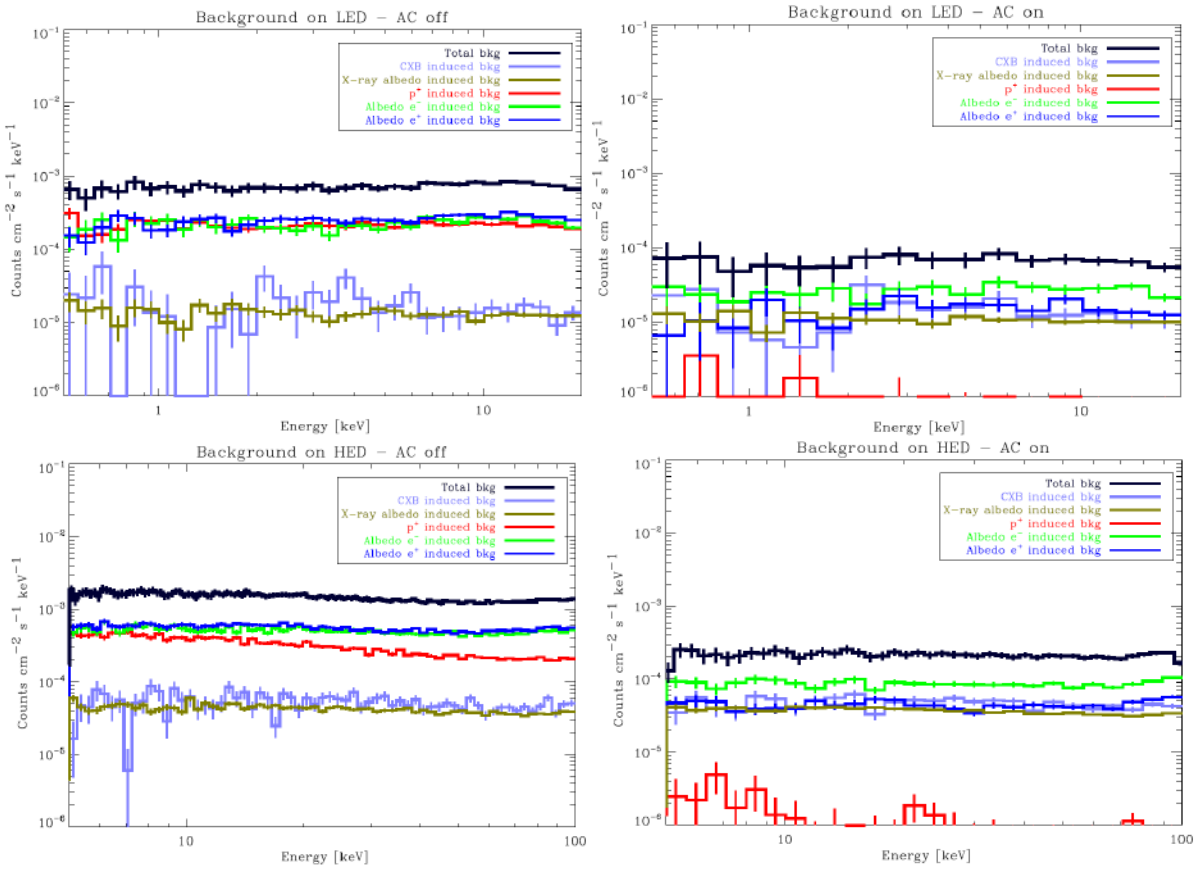

Figure 4-45: Simulated background spectra, in counts cm^{-2} s^{-1} keV^{-1}, for the Case B configuration. Top panels*: LED background, in the 0.5 – 20 keV energy range, in "AC off" (left) and "AC on" (right) mode;* bottom panels*: HED background, in the 5 – 100 keV energy range, in "AC off" (left) and "AC on" (right) mode.*

The background spectral distribution is dominated by the continuum, with no evidence for fluorescence lines, and the overall shape is constant. As expected, the photonic component is only slightly affected by the AC triggering, while the protons are efficiently removed. However, the charged particles induced background also dominates after the removal of the AC events because of the counts generated by the electrons and positrons, reaching a level close the requirement in the HED. This is not the case if the plastic AC is placed externally to the passive shielding: the background level induced by the charged particles, including electrons and positrons, is well below the requirement (see Figure 4-47, right panel). This result implies that the presence of passive, highly absorbing material outside the AC generates a cascade of secondaries that can not be efficiently removed by the internal AC.

If an inorganic, in this case NaI, active shield is placed within the passive shield, the efficiency on removing electrons and positrons induced events increases, with a related background level about half the Case B configuration (see, again, Figure 4-47, right panel).

The problem with the use of a NaI scintillator is that intense Iodium fluorescence lines arise, as shown in Figure 4-46 (the HED background spectra for the Case C). The bump below 6 keV visible in the "AC off" mode is the sum of escape peaks emission lines, also arising at 9 keV. It must pointed out that in the Case C configuration the NaI is placed close to the detectors without any passive shielding to absorb its fluorescence emission.

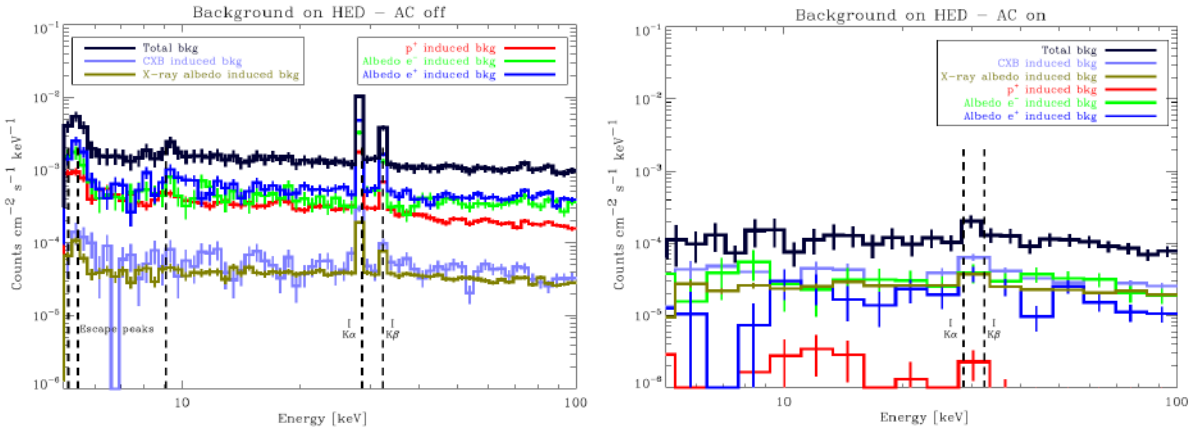

Figure 4-46: HED background spectra, in counts cm^{-2} s^{-1} keV^{-1}, for the Case C configuration in "AC off" (left panel) and "AC on" (right panel) mode.

4.10.3.2 Comparison of the tested configurations

The energy averaged background levels in the 0.5 -20 keV (LED) and 5 – 100 keV (HED) energy ranges are compared in Figure 4-47 for the three tested configurations. According to the present mission design, the LED count rate is not filtered by the AC triggering, so that the maximum background level, defined by the top scientific requirements, is 1×10^{-3} counts cm^{-2} s^{-1} keV^{-1} in "AC off" mode. The AC counts are instead removed from the HED detection, so that its maximum background level, 2×10^{-4} counts cm^{-2} s^{-1} keV^{-1}, must be intended in "AC on" mode. Both requirements are labelled by horizontal dashed lines.

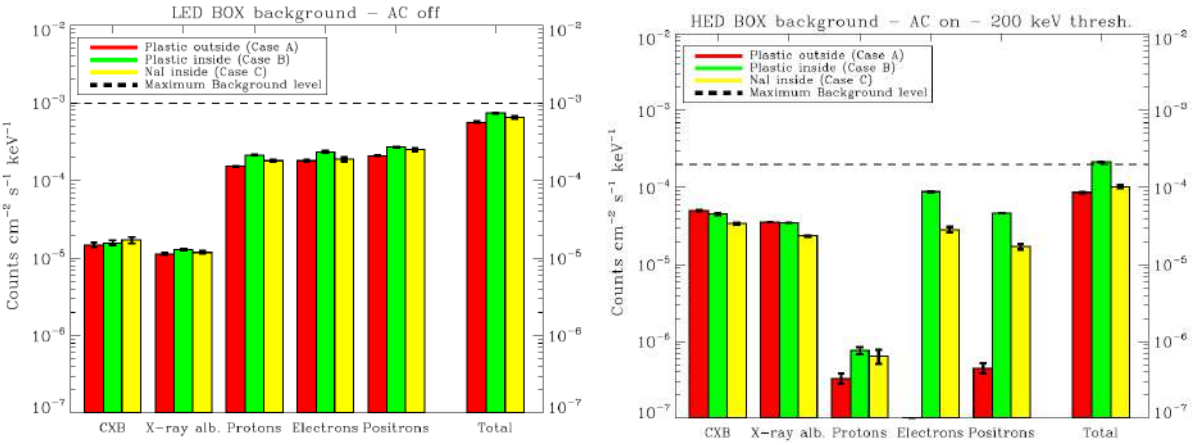

Figure 4-47: LED (left panel) and HED (right panel) background count rate in "AC off" and "AC on" mode respectively for a plastic active shield outside (red columns, Case A) and inside (green columns, Case B) the passive system. The yellow columns instead refer to the background level obtained by using an NaI scintillator as internal active shield (Case C). The horizontal line shows the NHXM accepted background level.

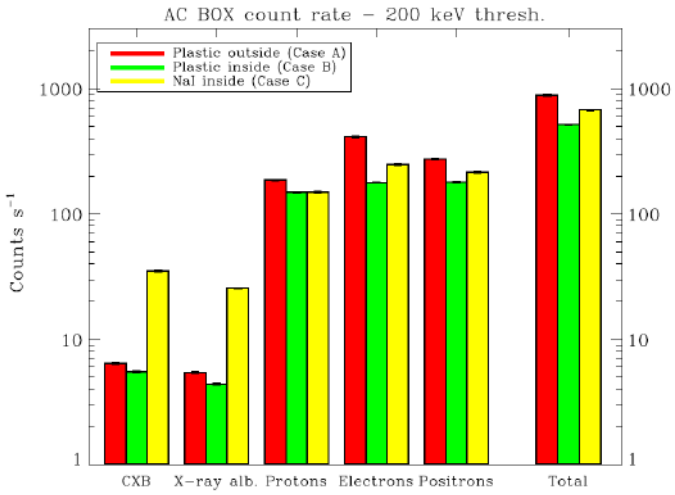

Figure 4-48: AC count rate induced by each class of input particle and the total value.

In the LED background results, the three configurations do not extremely affect the background level, since the AC triggering is not applied. The Case B, with the plastic AC inside, results in a background increase of about 50% respect to the Case A. The charged particles induced background is about an order of magnitude higher than the photonic background.

If we turn on the AC, the scenario changes, as visible in the HED plot of Figure 4-47, right panel. As previously noted, the external passive shielding decreases the AC efficiency to remove charged particles, an effect especially visible for the Case B, that results in a total background level about 2 times higher than the Case C, sharing the same geometry but using an inorganic AC. It must underlined that the AC, even if placed outside the passive shielding, would be surrounded by additional passive material due to the external case and the payload

itself, so that an increase in the electron and positron induced background should be expected in the Case A configuration.

The Case B design results in the highest background level, but also in the lowest total AC count rate, as shown in Figure 4-48, ranging between 880 (Case A) and 510 (Case B) counts s^{-1}. As expected, the NaI presents the highest efficiency in removing the photonic background, so that the induced AC count rate is higher.

The Case C design, with the NaI shield placed inside the passive material, results to be the best configuration in terms of background/AC count rate performances, but it also causes intense fluorescence lines in the HED background spectra, so that an additional layer of passive material, with high photoelectric cross section in the energy range of interest, is needed.

4.10.3.3 Conclusions about box geometry

1. Background spectral analysis:
   - The overall shape is constant for both LED and HED;
   - There is no evidence of fluorescence emission from the passive layers.

2. Plastic vs inorganic scintillator as active shield:
   - The NaI is more efficient in removing both photons and charged particles, resulting in a total background level 2 times lower while keeping a comparable AC count rate;
   - Intense fluorescence lines and escape peaks are detected by the HED if the NaI is applied.

– Effect of the passive shielding on the anticoincidence count rate:
   - The presence of external passive shielding generates a wealth of secondaries of lower energy to the AC decreasing its efficiency in removing the sources of background, in particular electrons and positrons;
   - As a direct consequence, the AC count rate is lower if the passive shield is placed outside.

4.10.4 NHXM complex geometries

In order to characterize the effect of the LEO space radiation environment on the total background level, two model of the NHXM camera shielding and focal plane has been developed: NHXM001 with a full simplified geometry and NHXM003 with a full complex geometry with pixellated detectors.

4.10.4.1 Geant4 output analysis

An IDL based software has been developed to analyze the Geant4 output (in FITS format).

The energy range of LED and HED are set respectively to [0.3 – 10] keV and [7 - 80] keV. A LED (HED) event is defined as the sum of the energy deposits, generated by the same primary particle, within the energy range. It is possible to flag coincidence events between LED and HED and group them in a separate class of events. In the present results, the removal of the LED-HED coincidence counts has no effect on the resulting background level. The analysis software is also designed to select the simulated counts according to the number of pixels detecting the event (PATTERN selection). The LED and HED are simulated in the NHXM001 model by a single volume (PATTERN = 1).

An anticoincidence event is defined as an energy deposit above the AC threshold, and the events generated by a single primary particle are considered as one single count. The AC thresholds used for the present results are different for the two geometries. In the analysis process, it is possible to set the AC threshold and to remove the AC – detectors coincidence events from the total background rate.

4.10.4.2 NHXM001 full simplified geometry

The simulation results presented here refer to this geometry model, composed by:

- NHXM focal plane;
- Passive shielding;
- Active shielding.

The implemented NHXM hybrid detection plane is dived into:

- LED: the Low Energy Detector is parameterized as a single volume (a box) with a side = 57 mm and thickness = 0.45 mm
- HED: the High Energy Detector is parameterized as a single volume (a box) with a side = 50 mm and thickness = 1.5 mm

The passive shielding system is composed of:

- a box surrounding LED and HED, with an height of 21.2 cm and a side of 25 cm;
- a passive collimator with an height of 1 m and a diameter of 10.5 cm

The collimator diameter is calculated for a detector diameter of 57 mm and a conservative lateral tolerance of ± 5 mm.

The main absorber, i.e. the high Z, high photoelectric cross section layer, is made of Tantalum. In order to absorb the Lα and Kα fluorescence lines, respectively at about 10 and 60 keV, a set of graded layers (Sn + Cu + Al+ C) is added to the main absorber.

The active shielding is made of Polystyrene, and it surrounds the passive shielding in the camera. If a particle is emitted towards the focal plane, it interacts respectively with the active and passive layers.

Materials, thickness and mass of the grading and AC system for collimator and box surrounding the detectors are reported in Table 4-5 and in the following table:

Mass [kg]	AC (Poly.)	Ta	Sn	Cu	Al	C	Tot.
Collimator	/	8.24	5.31	1.42	0.24	0.06	15.26
Box	1.22	7.55	4.86	1.3	0.22	0.05	15.20

Table 4-11: mass budget for NHXM001

In the following Figure is reported an overview of the simulated NHXM001 geometry.

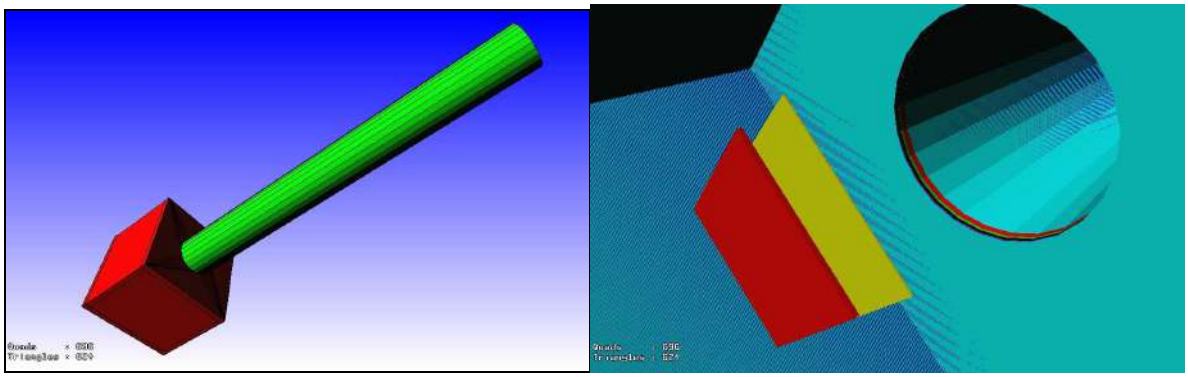

Figure 4-49: (Left panel) the simulated NHXM001 geometry; (Right panel): a detail of the detectors and collimator of the NHXM001 geometry.

In Figure 4-49 (right panel) is reported a detail of the geometry.

The results presented here are simulated with the NHXM001.1 version of the geometry.

4.10.4.3 Induced background

The resulting background level, averaged along the detecting energy range, is summarized in the following table with an AC threshold of 200 keV:

cts cm^{-2} s^{-1} keV^{-1}		AC off	AC on (200 keV)
Protons	LED	2.5×10^{-4} +/- 9×10^{-6}	
	HED		6.7×10^{-6} +/- 7×10^{-7}
Electrons	LED	2.3×10^{-4} +/- 9×10^{-6}	
	HED		2.6×10^{-5} +/- 1×10^{-6}
Positrons	LED	2.9×10^{-4} +/- 5×10^{-6}	
	HED		2.6×10^{-5} +/- 7×10^{-7}
CXB	LED	3.3×10^{-5} +/- 9×10^{-6}	
	HED		5.9×10^{-5} +/- 5×10^{-6}
Albedo	LED	1.3×10^{-5} +/- 5×10^{-6}	
	HED		2.7×10^{-5} +/- 3×10^{-6}
Sum	LED	**8.1×10^{-4}**	
	HED		**1.4×10^{-4}**

Table 4-12: the background level averaged along the detecting energy range [0.3 – 10] keV (LED) and [7 - 80] keV (HED) for NHXM001 geometry

The following Figure reports some induced simulated LED (in blue) and HED (in red) background spectrum:

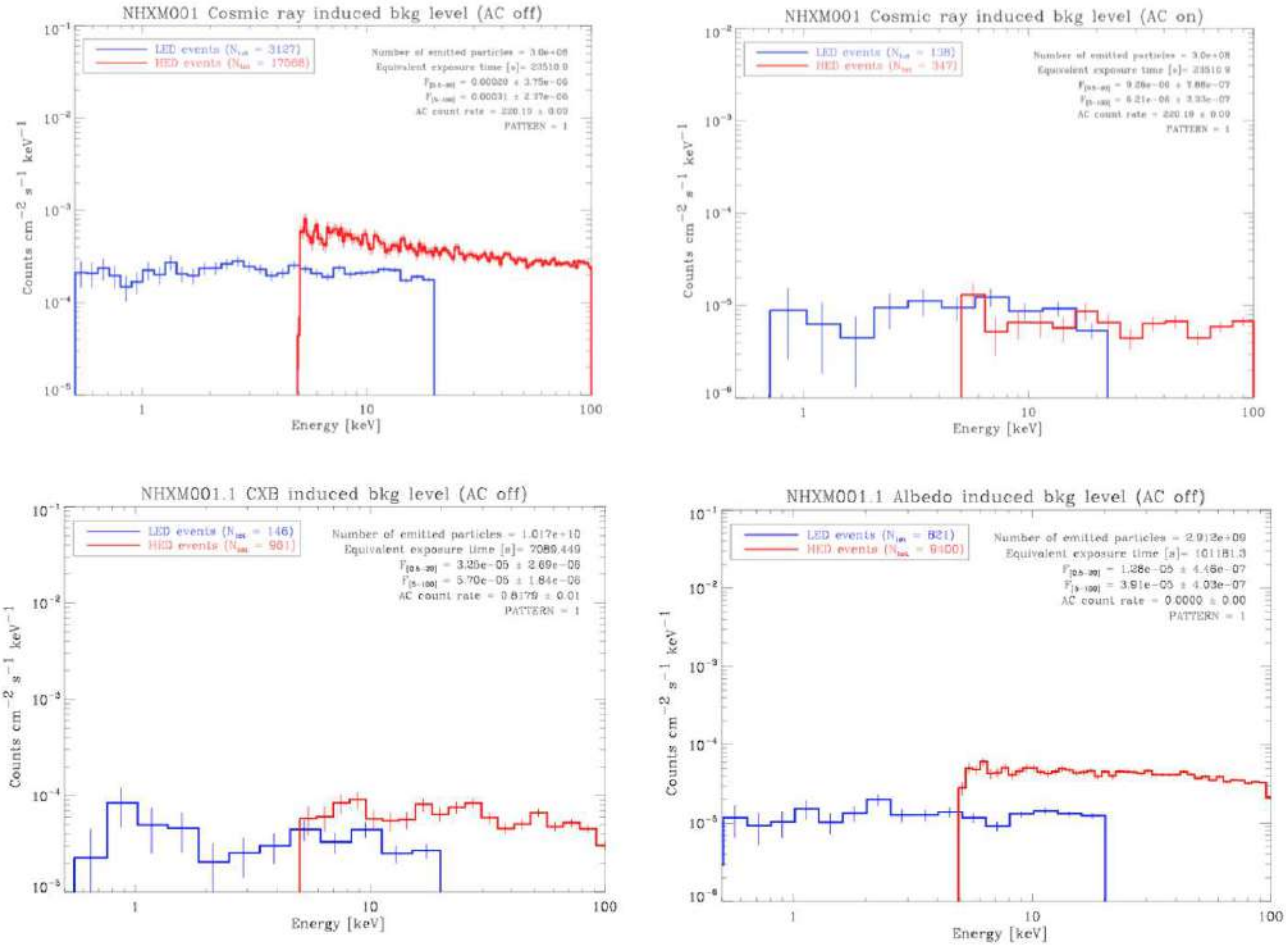

Figure 4-50: Some induced simulated LED (in blue) and HED (in red) background spectrum fro NHXM001 geometry.

4.10.4.4 Proton induced background

The background spectra presented here are generated by the sum of primary and secondary protons. The resulting AC count rate, induced by proton interactions, is 220.2 cts s^{-1}.

The induced proton background spectra are roughly constant, with no visible fluorescence lines. The anticoincidence triggering decreases more efficiently the HED background with respect to the LED background: while in AC off mode the HED count rate is about 50% higher than LED, the result is inverted after removing the coincidence events.

One of the main objectives of the present simulation is the evaluation of the impact of the spacecraft materials (e.g. shielding, structure) on the final background count rate. A simple approach is computing where the primary particle impacts before generating the count. The results, for both AC off and on, are shown respectively in Figure 4-50.

	AC off		AC on	
	LED	HED	LED	HED
Collimator external layer	13.7	11.2	93.1	85.6
Collimator internal layer	0.1	0.2	0	1.1
AC bottom panel	14.2	21.2	1.4	4.3
AC top panel	12.9	10.7	0	1.7
AC lateral panels	59.1	56.7	5.6	7.1
Direct LED hit	0	0	0	0
Others	0	0.03	0	0.3

Table 4-13: Percentage of detected counts generated by primary interactions with the listed volumes.

While in AC off mode, more than 50% of the detected events are generated by protons impacting on the lateral AC box panels, after removing the coincidence counts more than 85% of the simulated background is produced by protons directed to the collimator external layer.

However, it must be pointed out that the NHXM001 model does not account for the telescope structure (e.g. platform) or electronics, and the total background level is strictly related to the amount of mass. Further simulations on more complex NHXM models are needed to assess this result.

The higher impact of collimator-induced interactions on the LED count rate could explain in part the higher background level with respect to the HED.

4.10.5 NHXM003

The simulation results presented here refer to this geometry model, composed by:

- NHXM focal plane with two boxes configuration
- Passive shielding;
- Active shielding with BGO and Polystyrene
- Pixellated detectors

The LED detector is 4x4 cm^2, 150 μm tickness, 100x100 μm each pixel.

The LED-HED distance is 2 cm

The HED detector is composed by4 module of 2x2 cm^2 each with 0.2 mm spacing between them, 2 mm tickness, 50x50 pixel each module

The AC module is compound by two components: an AC of BGO (AC0) of thickness 20 mm and an AC of Polystirene (AC1) of 3 mm thickness.

The Al box has the following dimension: 120x120 cm^2 base, 106 cm height, tickness 6 mm

The graded collimator (see NHXM001 geometry description) is 900 mm length.

In addition, there is an external Al box to simulate the S/C.

The following Figure reports the NHXM003 geometry.

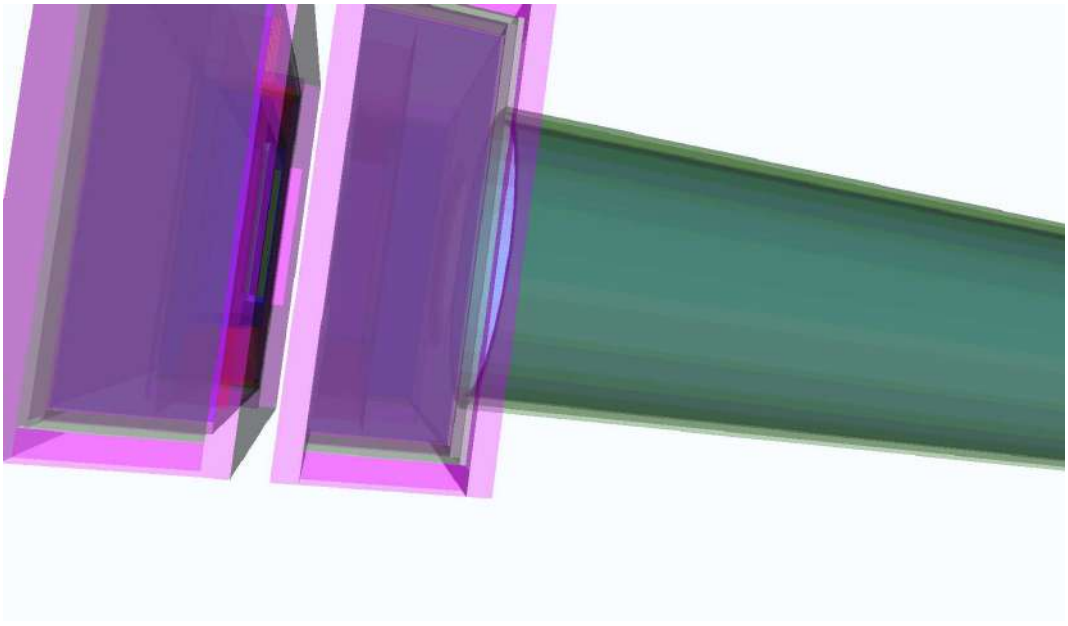

Figure 4-51: the simulated NHXM003 geometry

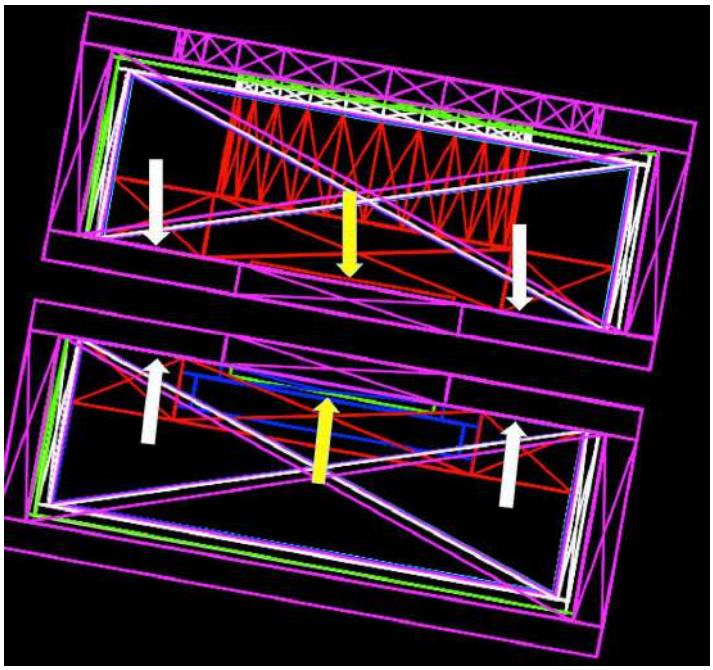

Figure 4-52: details of the NHXM003 geometry.

4.10.5.1 Induced background

The resulting background level, averaged along the detecting energy range, is summarized in the following table with an AC threshold of 10 keV fro BGO and 100 keV for Polystyrene.

cts cm^{-2} s^{-1} keV^{-1}		AC off	AC off (PAT = 1)	AC on
Protons	LED	2.0×10^{-4}	9.4×10^{-5}	
	HED			1.5×10^{-5}
Electrons	LED	1.4×10^{-4}	6.5×10^{-5}	
	HED			2.7×10^{-5}
Positrons	LED	1.4×10^{-4}	7.2×10^{-5}	
	HED			2.7×10^{-5}
CXB	LED	$\approx 6.0 \times 10^{-4}$	$\approx 5.2 \times 10^{-4}$	
	HED			$\approx 5.4 \times 10^{-5}$
Albedo	LED	$\approx 1.2 \times 10^{-4}$	$\approx 4.7 \times 10^{-5}$	
	HED			$\approx 2.7 \times 10^{-5}$
Sum	LED	**1.2×10^{-3}**	**8.0×10^{-4}**	
	HED			**$\approx 1.5\times 10^{-4}$**

Table 4-14: the background level averaged along the detecting energy range [0.3 – 10] keV (LED) and [7 - 80] keV (HED) for NHXM003 geometry

The following Figure reports the overall induced simulated LED and HED background spectrum:

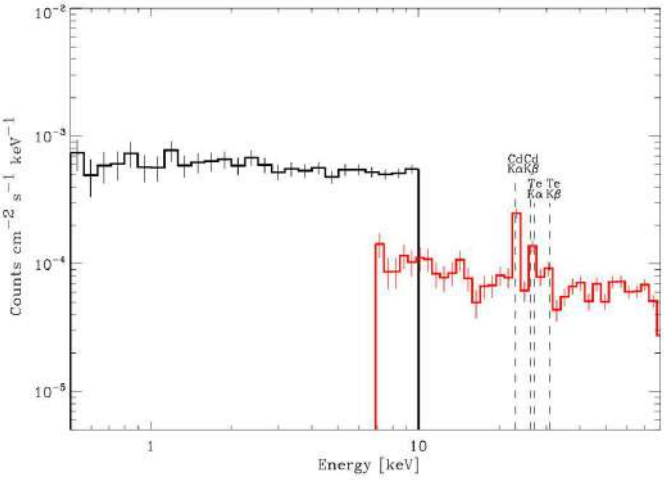

Figure 4-53: Overall induced simulated LED (in blue) and HED (in red) background spectrum fro NHXM003 geometry.

The level of induced background is compatible with the NHXM specification.

4.10.6 Background rejection with different AC configurations

The Anti-Coincidence (AC) system, completely surrounding the HED systems in the second configuration proposed for the SIC is composed by a passive shielding in the grated configuration presented in Table 4-9 coupled with an inorganic scintillator. Two scintillating materials are considered: Bismuth Germanate (BGO) and Cesium Iodides either doped with Sodium (CsI(Na)) or Thallium (CsI(Tl)). The BGO is a no-hygroscopic high density scintillation material, that emits 8-10 photons/keV with a peak at 480 nm. CsI(Tl) is one of the brightest scintillator (54 photons/keV) with the maximum of the emission situated at 550 nm. It is slightly hygroscopic with plastic mechanical properties, and as anticoincidence detector must be included in a teflon envelope 1 micron thick. CsI(Na) is as efficient as the CsI(Tl) with an emission peak at 420 nm and a light yield of 41 photons/keV and because of its hygroscopicity, it is provided with a 1 mm Al cage. The three different emission spectra are shown in *Figure 4-54* as function of the wavelength.

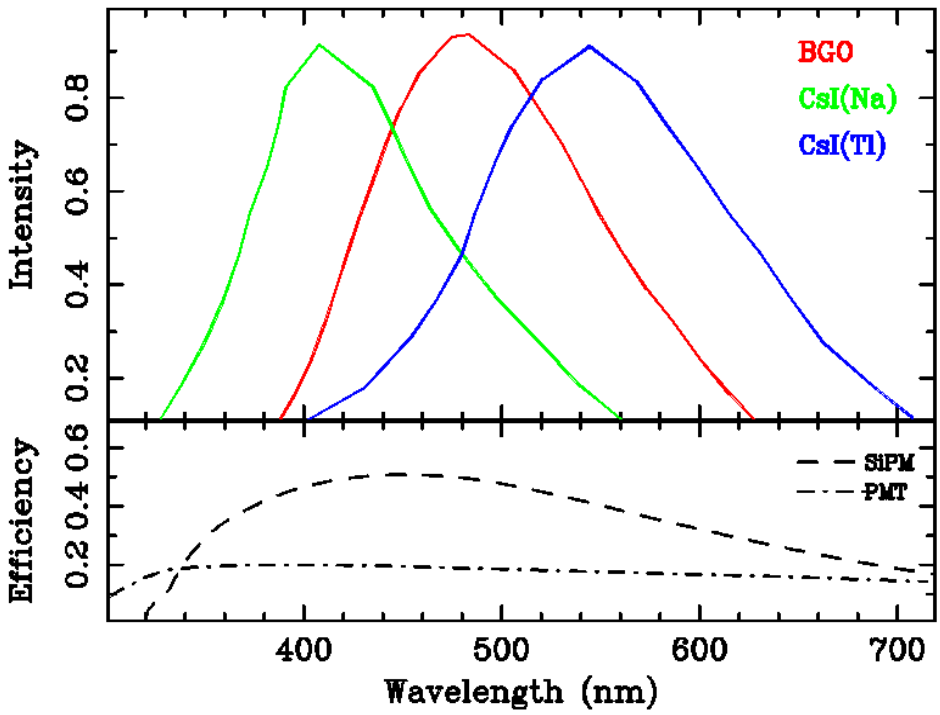

Figure 4-54: emission spectra of the BGO plotted with the red line, CsI(Na) plotted with the green line and CsI(Tl) plotted with the blue line. Superimosed to the spectra is the efficiency of the PMT and SiPM.

The light produced by the scintillator is usually collected by PMT, whose working range well matches the emitted spectra. Moreover, we investigated the possibility of using SiPM as light detector. The quantum efficiency of the two sensors are shown in the bottom panel of *Figure 4-54*.

The study of the efficiency of the AC detector with the proposed configurations has been performed with a GEANT4[1] simulator that includes the detailed description of the HED and AC geometry as showed in Figure 4-33; an empty Al box for the LED camera is also taken into account together with the cage for the for CsI(Tl) and for the CsI(Na). The light collection from the scintillator is performed with two PMT of size 35x1.6 mm^2 each and with 12 SiPMs with a similar collecting area.

GEANT4 simulator provides the amount of energy deposited in the scintillators and this is converted into UV photons with the factor relative to the considered scintillator.

To evaluate the fraction of light collected by the PMTs we performed an ad-hoc simulation that, assuming a reflection from the scintillator walls of 97%, follows photons randomly generated inside the scintillator up to their detection or absorption. We find that the fraction of collected light is proportional to the ratio of the PMT covered area to the total scintillator surface. The same factor is also applied for the SiPMs.

Charged particle, protons, electrons and positrons are generated in a 4π solid angle with isotropic angular distribution and in the energy range 30 MeV–100 GeV with the spectra presented in section 4.10.1.

The number of incident primary particle is $24x10^6$ for protons, $6x10^6$ for electrons and $7.2x10^6$ for positrons that allows for about 1500 events in the 7-100 keV range of the residual spectra. A threshold of 5 photoelectrons for the PMT and 15 for the SiPM is applied to trigger events in the AC; this converts in the thresholds for the energy deposited in the scintillator show in *Table 4-15*.

The total rate of residual rate in the range 7-100 keV, for the three scintillators and the two light detector considered, is shown in *Table 4-15*.

Scintillator	Threshold (keV)		Rate (10^{-5} ph cm^{-2} s^{-1} keV^{-1})	
	PMT	SiPM	PMT	SiPM
BGO	90	110	7.4±0.2-5 (2.4±0.1 protons; 2.1±0.1 electrons; 2.9±0.1 positrons)	7.5±0.2 (2.4±0.1 protons; 2.1±0.1 electrons; 3.0±0.1 positrons)
CsI(Tl)	20	25	6.6±0.2 (2.0±0.1 protons; 1.8±0.1 electrons; 2.8±0.1 positrons)	6.7±0.2 (2.1±0.1 protons; 1.8±0.1 electrons; 2.8±0.1positrons)
CsI(Na)	20	25	7.1±0.2 (2.3±0.1 protons; 1.9±0.1 electrons; 2.9±0.1 positrons)	7.0±0.2 (2.1±0.1 protons; 1.9±0.1 electrons; 3.0±0.1 positrons)

Table 4-15: residual HED rate in the range 7-100 keV

According to the simulations, the three type of scintillators we investigated give rejection efficiency equivalent for charged particle, even if the CsI is slightly more efficient. However, their different density (7.13 g/cm^3 for BGO and 4.51 g/cm^3 for CsI) can produce different rejection efficiency for photons and further simulations are required to evaluate these effects considering that in LEO orbit the contribution of photons to the residual background is not negligible.

The SiPM has a quantum efficiency higher that the PMT, however its high electronic background converts in a slightly higher energy threshold, with similar results for the particle residual background in the HED.

4.11 Interfaces

4.11.1 Electrical Interface

The power budget of the three SICs is summarized in Table 4-16.

Table 4-16 Power budget of the three SICs

Function	Power (W)
LED & FEE Assemblies	3
LED BEEs	12
LED Thermal Controls	30
HED & FEE Assemblies	18
HED BEEs	12
HED Thermal Controls	3
AC & FEE Assemblies	9
DPU	11
Total Secondary Power	**98**
Total Primary Power *(75% DC-DC efficiency)*	**130.0**

4.11.2 Mechanical Interface

The mass budget of one SIC is summarized in Table 4-16.

Table 4-17 The SIC mass budget

Camera Items	**Mass (kg)**
Graded baffles	45.0
Baffle supports	7.8
Door chamber assy	5.7
Filter wheel assy	6.3
Lower cameras body	5.1
Upper cameras body	6.0
LED assemblies	0.75
HED assemblies	1,05
Shielding	10.5
Valve modules	3.3
Thermal interfaces	3.6
Cabling, connectors	3.9
PCBs	0.9
Harness	0.3
BEEs	6.6
DPU	12
Total	**118.8**

5. X-ray Polarimeter

5.1 General Description

The X-ray Polarimeter is aimed to perform polarimetry in the band 2 – 80 keV of the same sources studied simultaneously with the Spectral Imaging Camera. It is positioned at the NHXM fourth telescope focal plane.

It is composed of three sensors that can be alternated at the focus: the Low Energy Polarimeter (LEP), the Medium Energy Polarimeter (MEP) and the High Energy Polarimeter (HEP, foresee as a goal, but not in the baseline). Each sensor is equipped with its Back End Electronics that powers and controls the front end electronics, resident on the sensor, while they all share a common Control Electronics, including a processor, the low energy power supplies, mass memories and the circuitry devoted to Housekeeping and Telecommands.

5.2 Low Energy Polarimeter

5.2.1 Electrical Design

ASIC CMOS Chip

We present here the architectural description of the ASIC.

The chip has 105,600 hexagonal pixels arranged at 50μm pitch in a 300X352 honeycomb matrix, corresponding to an active area of 15X15mm^2 with a pixel density of 470/ mm^2. Each pixel is connected to a charge-sensitive amplifier followed by a shaping circuit. The chip integrates more than 16.5 million transistors and it is subdivided in 16 identical clusters of 6600 pixels (22 rows of 300 pixels) or alternatively in 8 clusters of 13,200 pixels (44 rows of 300 pixels) each one with an independent differential analog output buffer.

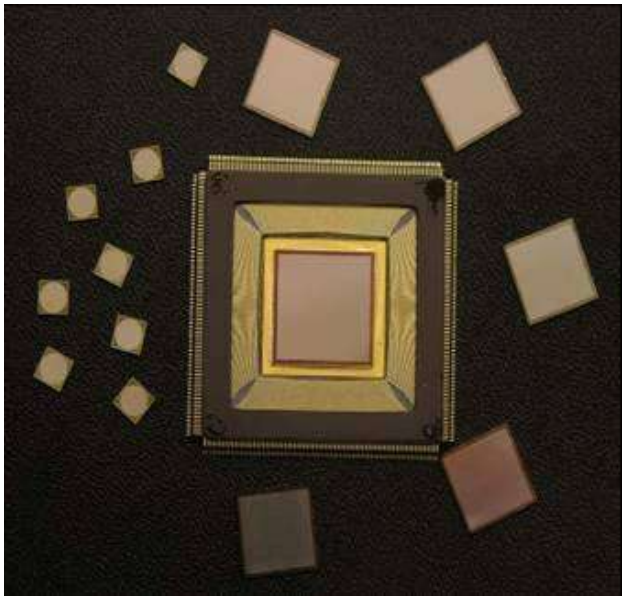

Figure 5-1: The actual ASIC version (center) with 105,600 pixels is shown bonded to its ceramic package (304pins).

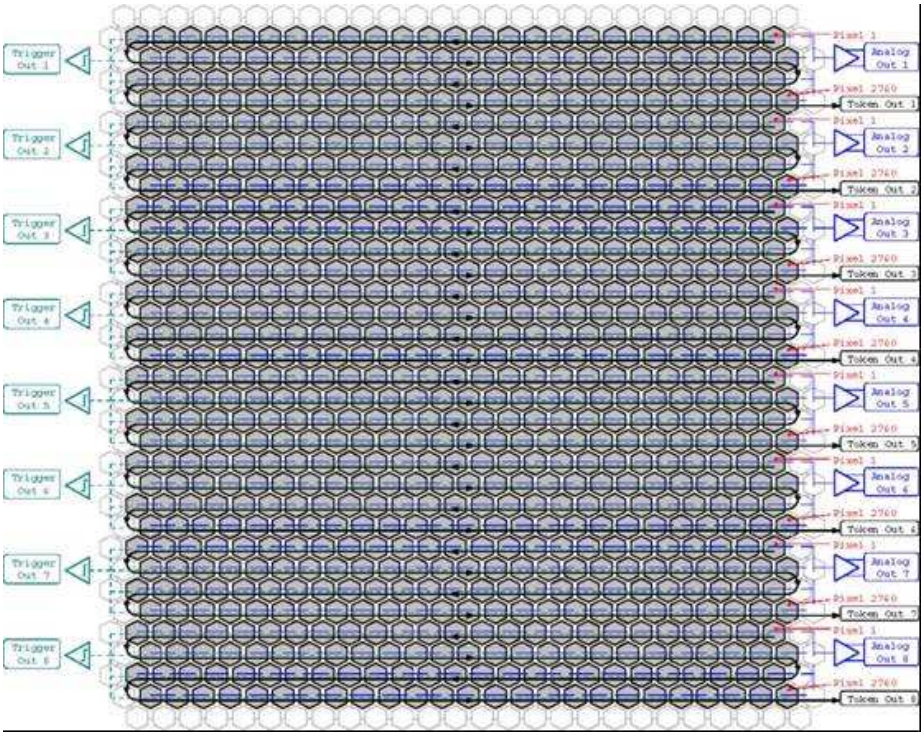

Figure 5-2: Simplified pixel layout

Each cluster has a customizable internal self-triggering capability with independently adjustable thresholds. Every 4 pixels (mini-cluster, see Figure 5-3) contribute to a local trigger with a dedicated amplifier whose shaping time (Tshaping~3 μs) is roughly a factor two faster than the shaping time of the analog charge signal.

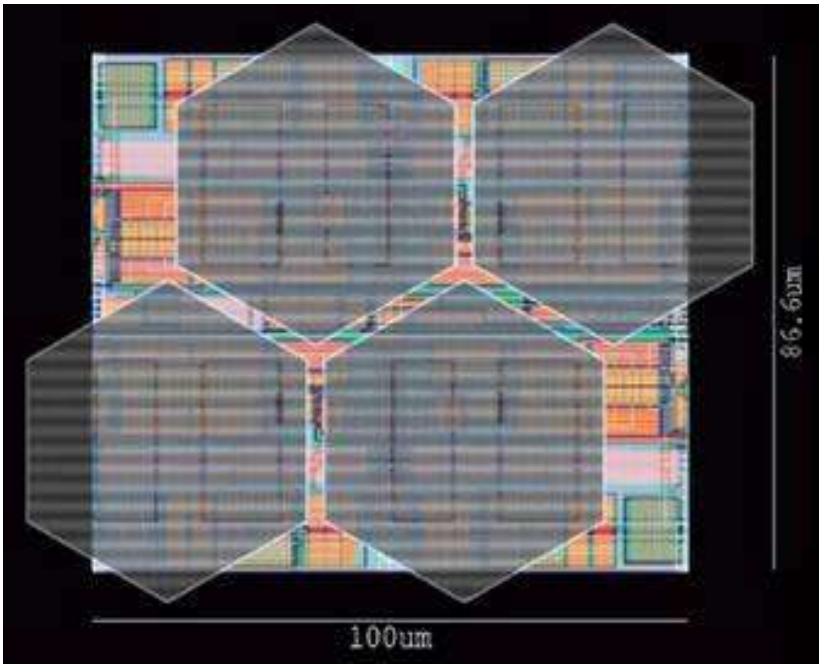

Figure 5-3: The 4-pixel self-trigger mini-cluster definition

The contribution of any pixel to the trigger can be disabled by directly addressing the pixel in question. An internal wired-OR combination of each mini-cluster self-triggering circuit holds the maximum of the shaped signal on each pixel. The event is localized in a rectangular area containing all the triggered miniclusters plus a user selectable margin of 3-4 pixels. The Xmin, Xmax and Ymin, Ymax rectangle coordinates are available as four 9-bit data output as soon as the data acquisition process following an internally triggered event has terminated, flagged by the DataReady output. The event window coordinates can be copied into a Serial-Parallel IO interface register (a 36stage FIFO) by applying an external command signal (ReadMinMax). Subsequently, clock pulses push out the analog data to a serial balanced output buffer compatible with the input stage of the Texas Instruments 12 bit flash ADC ADS572x.
In self-trigger operation the read-out time and the amount of data to be transferred result vastly reduced (at least a factor of 500) with respect to the standard sequential read-out mode of the full matrix (still available, anyway). This can be achieved thanks to the relatively small number of pixels (~200) within the region of interest.
Main characteristics of the new improved ASIC chip version wrt the actual version are:

Parameter	**Actual ASIC version**
peaking time:	3–10 ms, externally adjustable;
full-scale linear range:	30,000 electrons;
pixel noise:	50 electrons ENC;
read-out mode:	asynchronous or synchronous;
trigger mode:	internal, external or self-trigger;
read-out clock:	up to 10 MHz (readout time per pixel=100ns)
self-trigger threshold:	2300 e-
frame rate:	up to 10 kHz in self-trigger mode (event window);
parallel analog output buffers:	1, 8 or 16;
access to pixel content:	direct (single pixel) or serial (8–16 clusters, full matrix, region of interest).
fill fraction (ratio of metal area to active area):	92%.
ROI user-selectable margin	10 or 20 pixels
Other	--

Table 5-1: ASIC main parameters

The Back-End Electronics

The Back-End Electronics (BEE) is in charge of:

- Distribute and filter the low voltage power supply required to the ASIC;
- Supply the GPD with all the high voltages needed;
- Manage the ASIC analog and digital I/O;
- Implement a spectroscopy electronic chain for the GEM analog output;
- Digitally convert the analog output of the ASIC (ADC function);
- Store auxiliary information related to each event (e.g. X,Y coordinates of the ROI corner);
- Time-tag the events with at least 5μs of resolution;
- Digitally perform some basic processing (pedestal calculation, suppression of not-fired pixels)
- Temporarily store the converted data (both from ASIC and GEM);
- Transmit to the CE the science data to be processed;
- Integrate some HK and Science Ratemeters related to the GPD activity (e.g. good event, rejected events, temperature…);
- Provide Instrument HK to the CE for active monitoring and telemetries purposes.

For analog signal integrity reasons, this BEE unit should be placed close to the GPD, at less than 20 cm. The GPD is the core of the instrument since it carries the GEM and the readout ASIC.

It is provided with different electrical interfaces:

- Power: 2 x 1.8V (Analog and Digital ASIC core power supply) and 2 x 3.3V (Analog and Digital interface circuitry power supply)
- ASIC Analog Input Reference Voltages

- 16 Trigger thresholds (one for each cluster) referred to Vref0 (generated internally to the ASIC)
- Test Input Signal
- Common Mode Voltage for Analog Buffers (VCM)

- ASIC Analog Output
  - 16 differential outputs (referred to VCM)
  - Vref0
- Serial Digital Interface (dataIn, dataOut, clock, some Load/Read signals): LV-TTL
- Readout Digital Signals (trigger, dataReady, RO clock,…): LVDS
- Other Digital Signals: LV-TTL
- GEM analog spectroscopy signal

BEE - GPD Electronics Interface Description

The ASIC will be used in self-triggering mode in which the chip itself recognizes an event and prepares a rectangular area (Region Of Interest, ROI) to be read out by the Back-End electronics: the ASIC provides a differential analog output which shall be amplified and converted into an 16bit digital word by the BE Electronics.

As a baseline the BEE will use 5V CMOS/TTL digital levels, so a suitable buffer will adapt the TLL outputs of the Back-End to LV-TTL levels required by the ASIC.

Electrically, the BEE communicates with the GPD board with one or more flat cables for a total number of 60 lines, including power supplies and ground lines.

The GEM is connected to the BEE with an HV cable that carries the spectroscopic signal.

According to later development, a possible simplification of this interface can take place. In fact 14 analog signals can be kept on the ASIC if the only used readout mode of the ASIC is the self-triggered.

Moreover a further reduction of 15 lines is possible (trigger threshold) if all the 16 threshold lines are put together on the ASIC.

The detector also requires three high voltage power supply lines (HV) in the range 0.2-3KV and currents of a few nanoampères (see Table 5-2).

As a baseline this HVs shall be derived using resistive voltage divider, keeping the higher value programmable through a 16bit DAC.

The critical High Voltage requirements for the HVPS (board inside the BEE) are:

ΔV	Nominal Volts	Range Volts	Current μA	Regul. bits	Stability % in the whole T range	Ripple mV	Ramp Up Volt/s	Ramp Down Volt/s
$V_{drift} = V_w - V_{Gup}$	1000	2000÷700	20	4	2	500 pk to pk	100	200
$V_{multiplication} = V_{Gdown} - V_{Gup}$	500	350÷600	1	8	0.5	100 pk to pk	10	10
$V = V_{Gdown} - V_{pad}$	300	100÷400	20	8	0.5	100 pk to pk	10	10

Table 5-2: High Voltage power supply requirements

BEE - Digital Processing Functional Description

This section illustrates the core functions of the back-end, whose architecture is depicted in Figure 5-4.

The serial link with CE is used to configure the ASIC and the Back-End processing itself when the Instrument is in idle mode; during observation the same link is used by CE to read the science processed data. Also the digital HK are read by this link.

A dedicated logic implemented in FPGA will be in charge of the ASIC management for event readout: it is essentially a sequencer that moves, according to pre-defined steps, the ASIC signals dedicated to get ROI coordinates and get all the analog values of the detected charges.

In parallel with this action, the ADC manager will drive the 12-bit ADC to sequentially digitize the pixel charges and store them in a dedicated memory area.

At the end of the charge readout, another sequence take place to store two pedestal samples for each pixel of the ROI. It is mainly composed of a delay (4-500μs) followed by the same ROI readout sequence used to acquire the pixel charges.

In the actual ASIC version, after pedestal acquisition, the pixel-by-pixel average is calculated by the FPGA and then subtracted to the corresponding acquired pixel charge.

In the new improved AS IC version we require stable pedestal values, so that their values will be stored in a memory that will be refreshed every 2-4 hours (TBC). In this way there will be a reduction by a factor 2-3 of the dead time to satisfy the GPD performance requirement of 10μs dead time per event.

The last processing step is the so-called *zero-suppression*. Aim of this step is to reduce the data to be transferred to CE, discarding the pixels whose pedestal subtracted charge is below a threshold common to all the pixels. For example a typical ROI is made of 200 pixels (1000 in the existing version) but the average number of fired pixels is around 50, so this step is able reduce the event size by 4.

A DAC manager is in charge to set an analog threshold, common to all the chips, which fixes the chip triggering level.

The BEE will digitalize a mean of 200 signals per event at 20 MHz. The resulting dead time will be of 10μs allowing a max data rate of 5000 ev/s with a 5% overall dead time fraction.

The Back-End memory will implement the following main areas related to events data:

- Acquired charge (1kWord)
- First Pedestal Acquisition (1kWord)
- Second Pedestal Acquisition (1kWord)
- Calculated Pedestal (TBC, 1kWord)
- Pedestal Subtracted Data (TBC, 50kWord)
- Event Header Data (time-tag, aux info)
- Output Buffer (managed in a FIFO manner) of at least 16 zero-suppressed events (> 16 x 256 word = 4kword)

Memory size will be minimum 128k x 16bit.

The analog section depicted in the above picture is a differential amplifier because the ASIC output section is made of two complementary lines (out+ and out-) with a common mode Vcm of 1.5V.

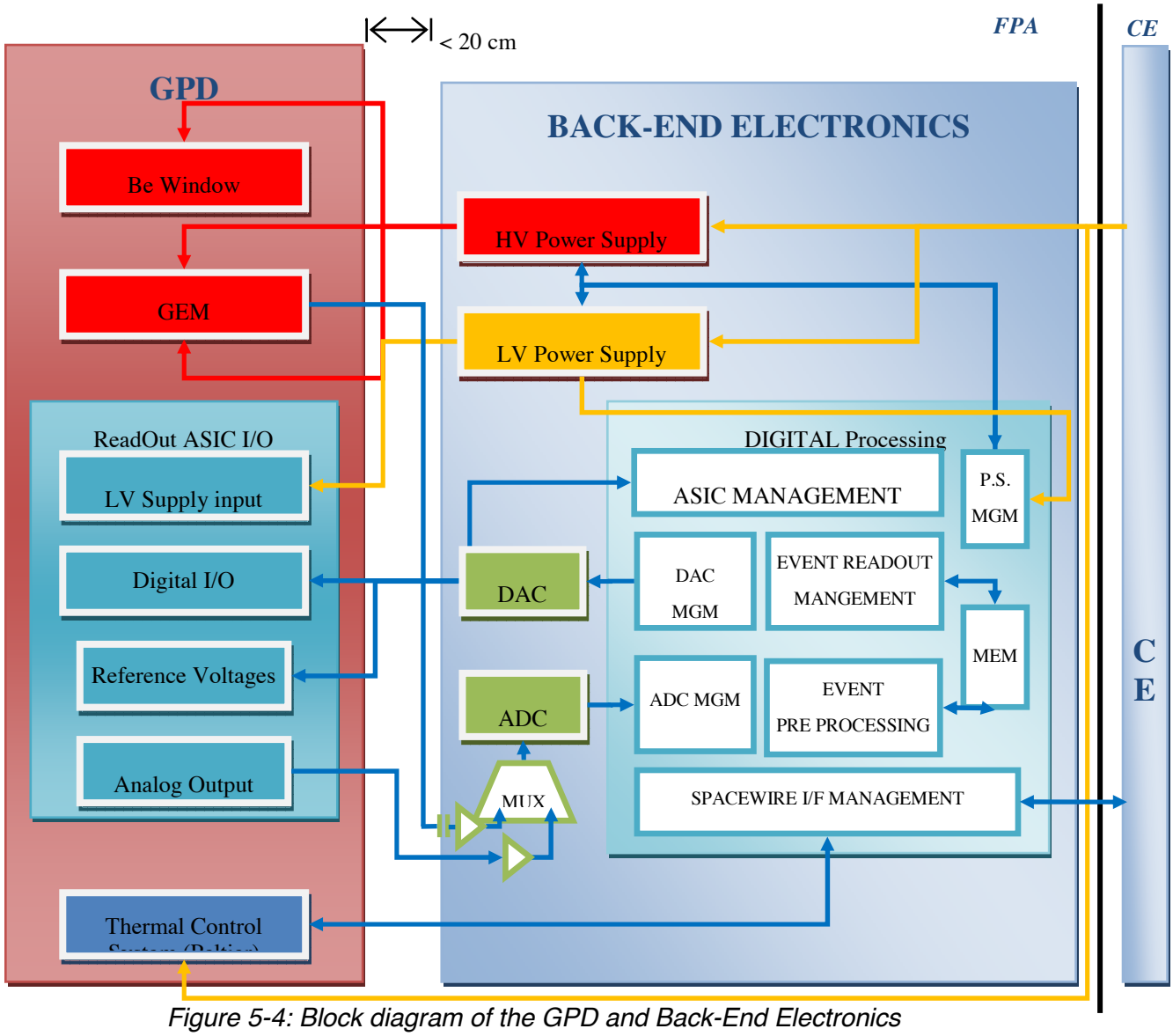

Figure 5-4: Block diagram of the GPD and Back-End Electronics

BEE – CE Interfaces Description

Three types of interfaces are present. First of all, a primary power bus from which all power supplies needed by the Back-End itself and the GPD are carried out.

It has been chosen to directly supply the Back-End with the primary power for two main reasons:

- In this way the "back-end" is a *stand-alone* unit/subsystem, that can be tested and integrated in parallel without the CE, which otherwise will become a bottleneck in the AIV flow
- The path of the high voltage cables is thus minimized (the solution with the HV DC/DC inside the detector assembly has been discarded due to noise and thermal considerations).

A serial digital LVDS data interface is then provided for science, command and digital housekeeping exchange with the CE.

Logically connected to this interface there is the clock line for the Back-End Electronics (20MHz, TBC, supplied by the CE) and the interrupt line used by BEE to prompt the processor that some data (e.g one or more event data) is ready to be read.

From the point of view of the data exchanges we list here a possible layout of the science data packets formatted by the BEE during the ASIC readout (Table 5-3) and pre-processed prior to be sent to the CE, at BEE level, by subtracting the pedestals and by suppressing all the not-fired pixels of the ROI. The BEE thus delivers to CE a data flow reduced by a factor of 2 and made of events whose average dimension is 50 fired-pixels (Table 5-4).

Considering a peak rate of 5000 ev/sec and assuming the average data size for a single photon of 1744bit, we get a peak data rate on this link of about 8.7Mbit/sec.

	16 bit word	word id
Header	Packet Type ID (RAW)	0
	Event Time (MSW)	1
	Event Time	2
	Event Time (LSW)	3
	ROI X width: ΔX	4
	ROI Y width: ΔY	5
	ROI corner: X0	6
	ROI corner: Y0	7
pixels data	Pix_0: charge (Q0)	8
	Pix_1: charge (Q1)	
	……	
	Pix_N-1: charge (QN-1)	7+N
	END MARKER	8+N

For a typical event of 12X16 ROI (in which 12*16=Δx*Δy=N): 3216 bit/ev

Table 5-3: Science Data Packet formatted by the BEE during the ASIC readout

	16 bit word	word id
Header	Packet Type ID (PROC)	0
	Event Time (MSW)	1
	Event Time	2
	Event Time (LSW)	3
	AUX info	4
	Nr of pixels (N)	5
	ROI corner: X0	6
	ROI corner: Y0	7
pixels data	Pix_0: Δx(8bit), Δy(8bit)	8
	Pix_0: charge (Q0)	9
	Pix_1: Δx(8bit), Δy(8bit)	
	Pix_1: charge (Q1)	
	……	
	Pix_N-1: Δx(8bit), Δy(8bit)	
	Pix_N-1: charge (QN-1)	7+N*2
	END MARKER	8+N*2

For a typical event of 50 zero suppressed pixels: 1744 bit/ev

Table 5-4: Science Data Packet sent from BEE to CE

The last interface is an analog differential line used to transmit to the CE the analog HK values to be periodically acquired.

The baseline foresees that this line is multiplexed on the Back-End in order to limit the harness between the two units.

5.2.2 Mechanical Design

Figure 5-5 shows the LEP Detector-FEE Assembly.

Figure 5-6 shows the complete LEP mechanical structure.

Figure 5-5:The LEP Detector-FEE Assembly

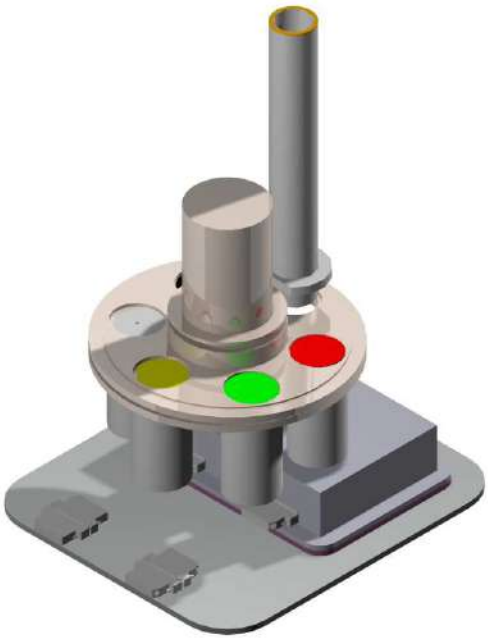

Figure 5-6: The complete LEP mechanical structure

5.3 Medium Energy Polarimeter

The MEP is based on the same design of the LEP with the following noticeable changes:

- a gas filling with a Argon based mixture (A 80%, DME 20% TBV)
- an increased pressure (3 Atm TBV)
- an increased absorption/drift gap thickness (30 mm TBV).

This new filling will make the MEP sensitive in the 5 – 35 keV range.

5.3.1 Electrical Design

Equivalent to the Low Energy Polarimeter.

5.3.2 Mechanical Design

The window is 150 μm (TBV) of Be in order to sustain the larger pressure. The detector bottom is equivalent to that of the LEP. The body is larger (TBD) to ensure the uniformity of the electric field with a thicker gap. A passive shield is to be designed.

5.4 High Energy Polarimeter

The photo-effect on s orbital electrons is an ideal analyzer of polarization but at higher energies the use of higher Z gases (mainly Xe) that have a larger scattering/stopping ratio and for which the multiplication in the GEM is critical, makes this technique less attractive. In order to exploit the feature of the telescopes, extended up to 80 keV, we evaluate the potentiality of a focal plane polarimeter based on Compton scattering. Many such instruments have been proposed in the past. One was a stage of the Stellar X-Ray Polarimeter built and qualified but never flown. In that case the scatterer was a lithium cylindric stick and Xe counters would detect the scattered photons1920. Due to the large area of the detectors the system was background limited even for relatively bright sources. In our case, since the lower energies are covered by LEP and MEP we want to build a polarimeter based on an active scatterer, namely a scatterer which is a detector itself, surrounded by a hollow detector for the final absorption of the scattered photons. A sketch of the instrument is given in fig. below.In such a device the coincidence of the two signals is a very effective background reducer, and the device should be source dominated even for faint sources.
The angular distribution of the Compton scattered photons is given by the Klein-Nishina cross section:

$$\frac{d\sigma}{d\Omega} = \frac{1}{2} r_0^2 \frac{E^2}{E_0^2} \left[\frac{E_0}{E} + \frac{E}{E_0} - 2 \sin^2 \theta_\gamma \cos^2 \phi_\gamma \right]$$

The Compton effect is a good analyzer of polarization for scattering angles close to 90 degrees and for relatively low energies. In our case (fig below) the scattering angles are limited to around π /2 by the geometry itself and can be further restricted with collimating disks around the scatterer. As scatterer we assume a stick of low-Z scintillator, read from the bottom with a PMT (or a SPAD or other). As final detector we assume a cylindrical hollow array of high Z detectors (CsI or LaBr3 or CdTe: the choice is not relevant at this stage). The most critical parameter to define the functionality of this device is the low energy threshold, namely the minimum

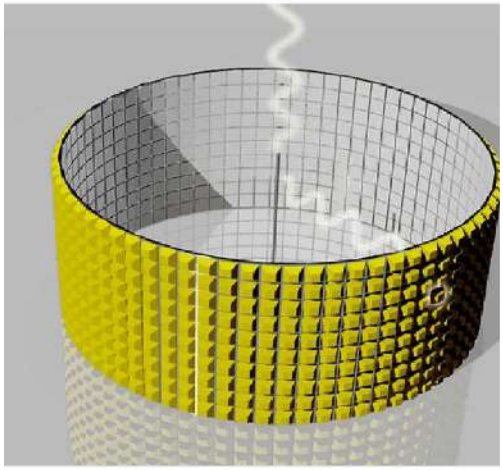

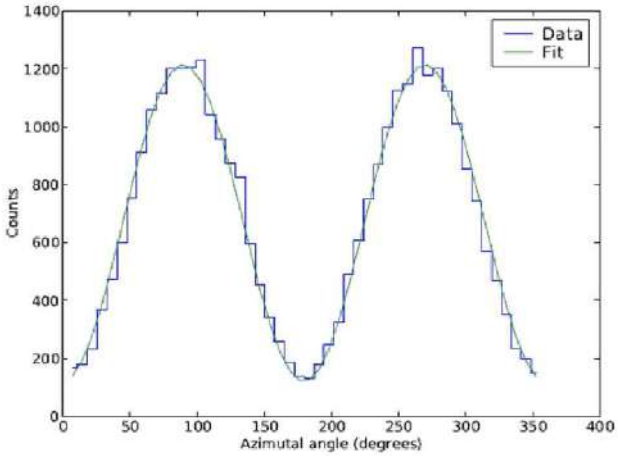

Figure 5-7: (Left) The sketch of the High Energy Detector based on Compton scattering. (Right) Modulation curve evaluated with GEANT 4 for the HEP. The configuration used in the simulation is the following: the scatterer is the plastic organic scintillator BC404 with a length of 10 cm and a diameter of 5 mm, the absorber is distant 5 cm from the scatterer and is LaBr3 with 2 mm of thickness. The height of the absorber is 10 cm. The simulation is performed at 35 keV.

energy of the impinging photons that can be detected in the scatterer. By assuming the (ambitious) value of 25 keV we derive an excellent modulation curve (see fig.8). If the hypothesis of negligible background holds, E can derive a very good factor of merit and thence a sensitivity extremely interesting from the point of view of the astrophysical targets. A worthwhile complement of LEP and MEP at higher energies. For these reasons, even though the design is extremely rear, we will go on exploring this as an interesting options. Also because, except the scatterer set up, the whole experiment can be built on the basis of very established technology.
A procurement activity has already started with the acquisition as a scatterer of doped crystal p-terphenyl from Cryos-Beta (Ukraine) and BC-404 plastic scintillator from Saint Gobain (France) read by a procured high Quantum Efficiency Photomultiplier (selected Super-Bialkali) from Hamamatsu (Japan). The absorber procured (from Saint Gobain) by us is $LaBr_3$ crystal completely assembled with a Hamamatsu PMT. Preliminary results of measurement of coincidence tagging efficiency at 22 keV and 59.5 keV show that the simulated configuration has similar performances of a real design.

5.5 Shielding System

The finalization of Shielding System configuration will require additional simulations and calculation of the background.

5.5.1 Active Shielding

BGO or CsI possibly for MEP and HEP.

5.5.2 Passive Shielding

Graded shielding possibly for LEP, MEP and HEP.

5.5.3 Collimator

To prevent X-rays entering from the side of the telescopes into the polarimeter area. Its length depends on the skirt of the optics, the composition is a trade-off between weight and shielding capability (if necessary, it will be evry similar to that one of the SIC camera).

5.6 Thermal Control

To drive the Peltier on the LEP and MEP body.

5.7 External Mechanical Box

To protect mechanically an thermally the polarimeters.

5.8 Electrostatic Grid

To reject charge particles from impinging on the Beryllium window that is at high voltage. To be considered in place the possible use of a magnetic diverter.

5.9 Sliding Device

To accommodate on one side the LEP/HEP and to the other side the MEP that are alternated according to scientific observation at the focus of the fourth X-ray telescope.

5.10 Filter Wheel

Filter wheels are now successfully flying on board of XMM-Newton and Swift. We intend to use the same design (which has been developed by Max Planck) to build a safe and reliable filter wheel. Each position of the filter wheel corresponds to an observation mode.

The relevant position are:

- Closed.
- Open .
- Grey filter .
- Calibration source LE
- Calibration source ME
- Polarized source LE
- Polarized source ME

The calibration sources will be described in the following. The filter wheel is equipped with a stepper motor.

For the stepper motor the type ZSS43 from PHYTRON has been selected which is available with a low outgassing rate and provides sufficient torque margin.

The bearing is manufactured by ADR S.A. Thomery in France, about 20.000 cycles (full rotations) of the filter wheel have been assumed for an orbital life of 10 years. Abrasive material from the gear should not be able to reach the bearing and the interior of the camera. This is achieved by a labyrinth.

For the position control redundant Hall sensors with a stop magnet for every position are used.

The filter identification number is determined for the HK by a set of 3 Hall sensors with magnets in coded locations. Data sheets for the sensors and a test report for the radiation hardness are available. For a redundant position determination a potentiometer is foreseen for the HK.

The position closed will be used either for protection from debris and during launch. Moreover it will be used for gathering internal (particle) background verifying that is negligible in measurements of polarization.

Calibration Sources

Calibration sources will be mounted in four positions of the filter wheel. The calibration will be done either with unpolarized source and with polarized source to monitor and control the behaviour of the experiment. Some of the data gathered from the polarized source can be used also in the Monte Carlo simulation to extract the best parameter for optimum signal/noise. Below we describe how polarized source and unpolarized source can fit into the filter wheel.

Polarized calibration source LE.

The modulation factor of the polarimeter is not constant with energy but it monotonically increases with it because the tracks becomes longer, since the energy loss decreases due to the effect of the Rutherford scattering. Moreover even if the first laboratory tests do not show any degradation of the gas mixture with time, we may foresee the use of a getter on board. However, we want to monitor the characteristics of the gas mixture in two ways. One is the monitoring of the gas gain stability and the evaluation of the calibration line. The other one is the monitoring of the modulation curve which reflects the drift properties of the gas. At the present time the modulation curve can be measured by the polarimeter with a Bragg crystal tuned at nearly 45° with the line characteristic of the anode of the X-ray tube itself. The reflected radiation is therefore polarized at a high level. With a lower efficiency the perfect crystal can reflect, also, the continuum. In space is not possible to foresee the use of an X-ray tube, however we can use an x-ray fluorescence source of adequate intensity such as Fe^{55}. Mn K-lines from Fe^{55} can excite 2.6 keV line from a PVC thin sheet. Graphite crystals at 45° can reflect those 2.6-keV lines polarizing them nearly at 100 %. Moreover LiF crystal reflects k_α lines close 47.6 degree polarizing them at 88 %. We can device, therefore, a composite X-ray calibration source. A thin graphite crystal is attached to a LiF thick crystal to polarize simultaneously 2.6 keV and 5.9 keV. A sheet of 40 μm thick PVC crystal is placed in front of the Fe^{55} source to convert part of the X-ray photons into 2.6 Chlorine photons. The unabsorbed Fe^{55} X-ray photons will cross the graphite crystal to be reflected by the LiF. The source will be compact (small volume and weight) to allow a safe use in space. The monitoring of the modulation into space will allow for the first time to fine tune the measured modulation of celestial source and to check whether some pollution have altered the drift (and therefore the diffusion coefficient) in the gas mixture. Due to the changing of the modulation with energy we consider that a simultaneous measurement at two energy is highly desirable to monitor the behaviour of the polarimeter in space. The counting rate for this double source will be such to allow an adequate measure of polarization within a reasonable time.

Polarized calibration source ME.

The polarized source for MEP will be based on Cd_{109} radioactive source. The diffraction crystal is TBD.

Unpolarized calibration source LE.

The gas gain of the detector is a function of the voltage difference across the GEM. Pollution of the gas due to outgassing and aging of the gas mixture can require higher voltage difference to reach the same gas gain. We want to monitor the gas gain using two radioactive sources. One radioactive source will be Fe^{55} . The Fe^{55} photons will impinge into the whole detector surface to monitor the gain across it. The counting rate will be 20 c/s (TBC). Fe^{55} can be a point source or a source diffused in a circular surface.

Unpolarized calibration source ME.

The second X-ray sources will be a radioactive Cd^{109} source which 22-25 keV X-rays do not reach the detector. This second X-ray source will be used to monitor the linearity of the gas gain with time. The counting rate of this second source will be (10 c/s TBC)

5.11 Main Simulation results

We report here the results of calculation and simulations based on configuration that are at the moment the baseline. We show the efficiency of the modulation factor and the Figure of Merit (QF). Also we show estimation of the sensitivity (Minimum Detectable Polarization) for these baseline configurations.

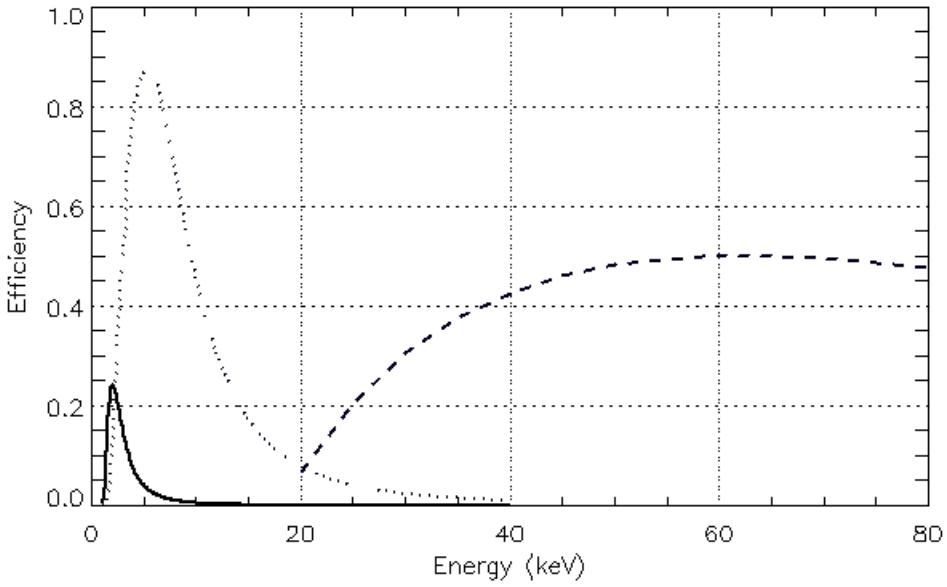

Figure 5-8: Efficiency for (solid) LEP, (dotted) MEP and (dashed) HEP

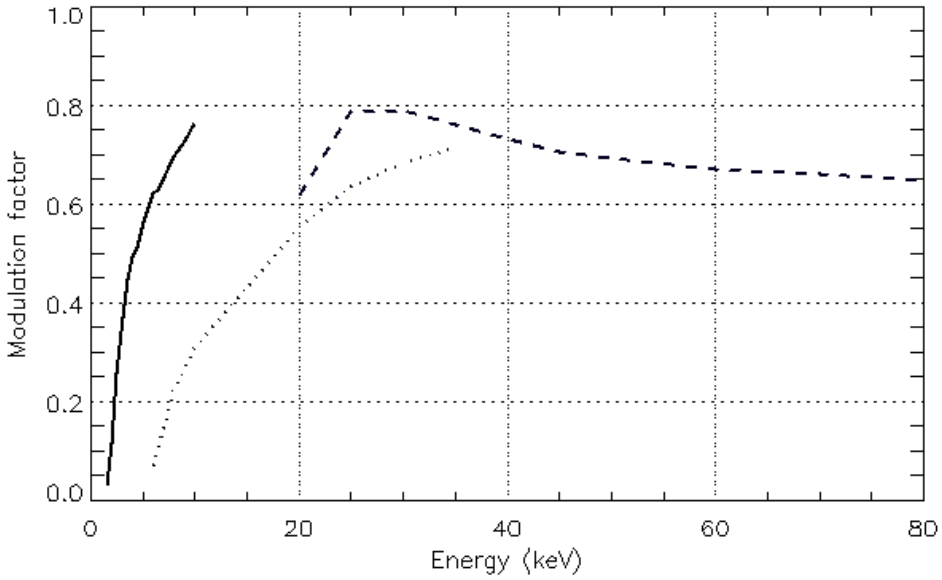

Figure 5-9: Modulation factor for (solid) LEP, (dotted) MEP and (dashed) HEP

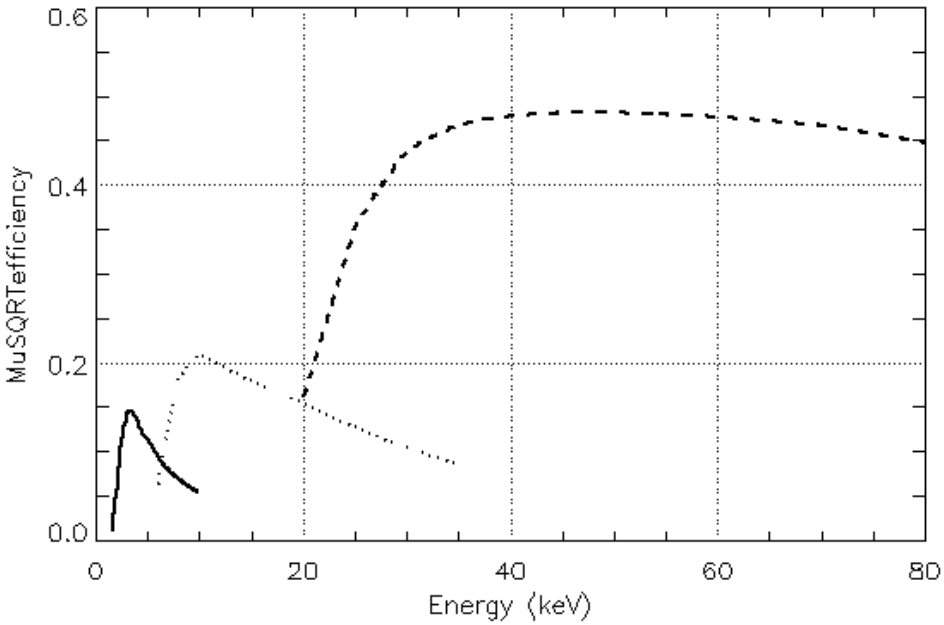

Figure 5-10: Merit factor for (solid) LEP, (dotted) MEP and (dashed) HEP

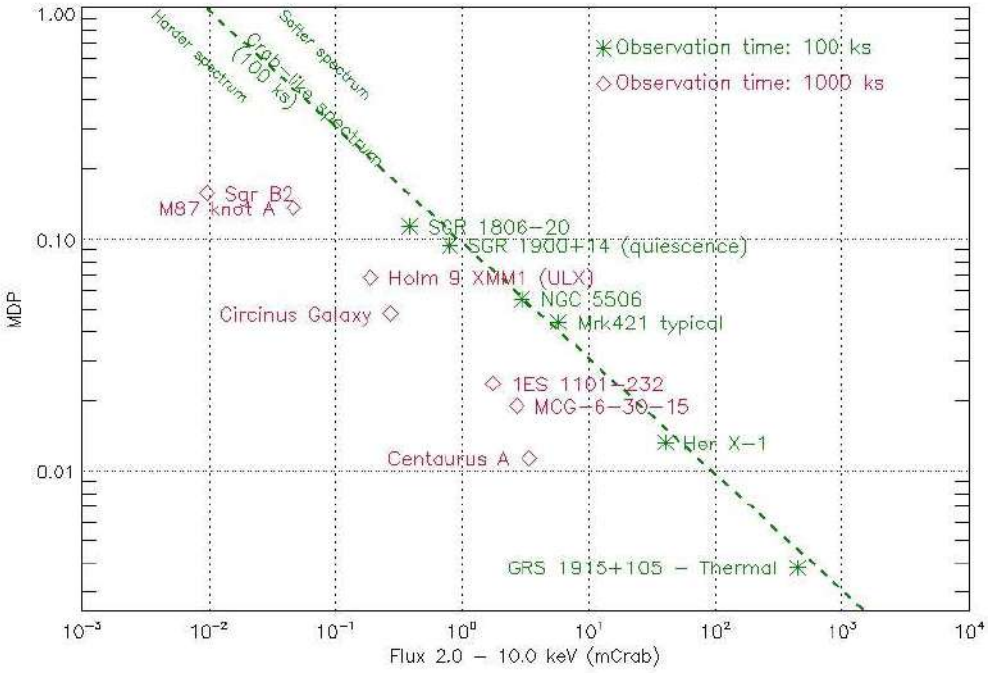

Figure 5-11: Minimum Detectable polarization for the LEP

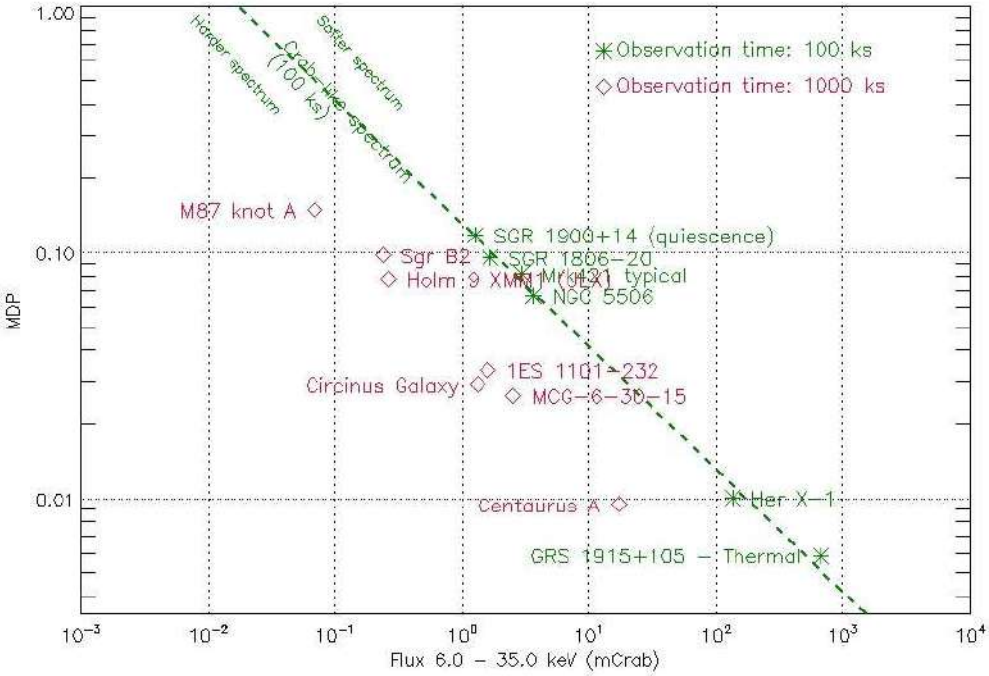

Figure 5-12: Minimum Detectable polarization for the MEP

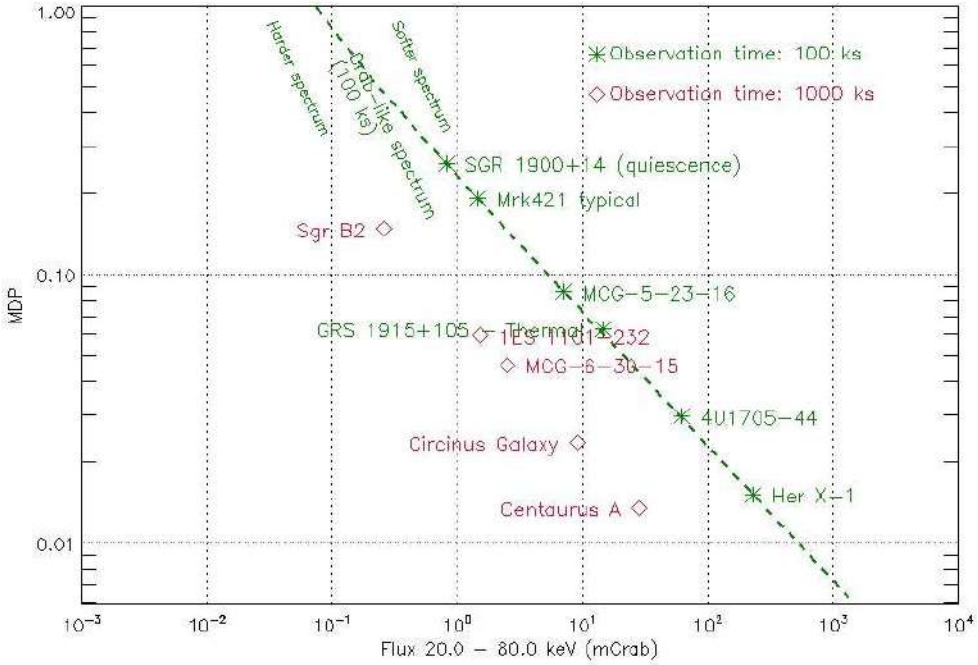

Figure 5-13: Minimum Detectable Polarization for the HEP

6. Ground Support Equipment

6.1 General Description

This section identifies the mechanical, electrical and optical tools required to support the Assembly, Integration, and Verification (AIV) and Calibration of the NHXM telescope at system and sub-system level presented in the Calibration Plan document (RD 7).

We remind here that these activities will follow the following flow:

1. **Subsystem functional tests**: these will take place during the development phases of the various subsystems (LED, HED, AC, optics shells), and will concern the verification of their functionality, with no reference to the scientific performance measurement and characterization.
2. **Subsystem scientific characterization**: After the functional tests, the subsystems will undergo a measurement campaign in order to quantify the subsystem parameters with the required accuracy, including both statistical and systematics effects.
3. **Payload AIV**: The two payloads, FPA on one side and MU on the other, are separetely integrated and functionally tested.
4. **Payload calibrations**: FPA and MU are separately calibrated to assess their scientific performances and verify the compliancy against the requirements.
5. **End-to-end tests**: The NHXM telescope, FPA + MU, is integrated, functionally tested and scientifically characterized.

The following GSE equipment are envisaged:

- **Electrical GSE (EGSE)** are essential to support the instrument integration and test campaigns which foresee:
  - A first set of functional tests to verify the system functionalities in terms of "operational mode" only. These tests verify requirements on Electrical I/F, Power consumption, Command execution, Housekeeping acquisition.
  - A second set of functional tests to verify the functions of the digital part of the electronic chains related to the processing of the scientific data. Digital pattern of data are generated at the beginning of the chain. These tests verify requirements on data acquisition, data processing, data packaging, data transmission.
  - Performance tests to be carried out for the scientific modes of operation. These tests verify the capability of the System to reach the scientific goal.
- **Mechanical and Optical GSE (MOGSE)** are required to mechanically handle the instrument components during the various integration and test stages, and to accomplish the optical alignments.
- **Thermal GSE (TGSE)** items are foreseen to provide the thermal interfaces required to operate the instrument. Some of this equipment are interfaced to the thermal/vibration/vacuum/EMC and calibration facilities required to carry out the environmental test and calibration of the instrument.

Reusability of the GSE items throughout the various AIV/AIT level is a driver for the GSE design and architectural choices. Furthermore, commonalities are envisaged among the EGSE s/w and the Ground Segment s/w.

The design concept of the relevant NHXM GSE equipment are presented in the following sections.

6.2 SIC GSE

The SIC test configuration at detector level and at camera level is depicted in Figure 6-1, and Figura 6-2, respectively.

The following GSE items are required:

- Cryo GSE to test the camera at operating temperature.
- SIC Detector Test Equipment (TE)
- SIC Camera Test Equipment (TE).

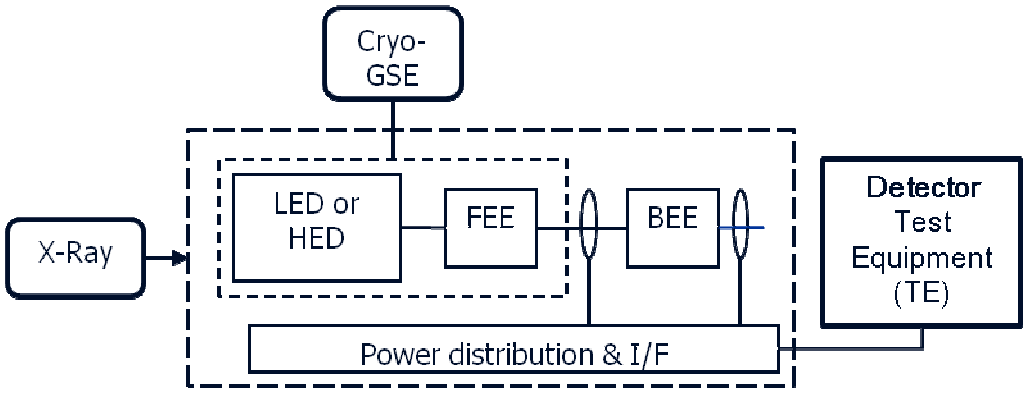

Figure 6-1:SIC Test Configuration for AIT and Calibration at Detector Level

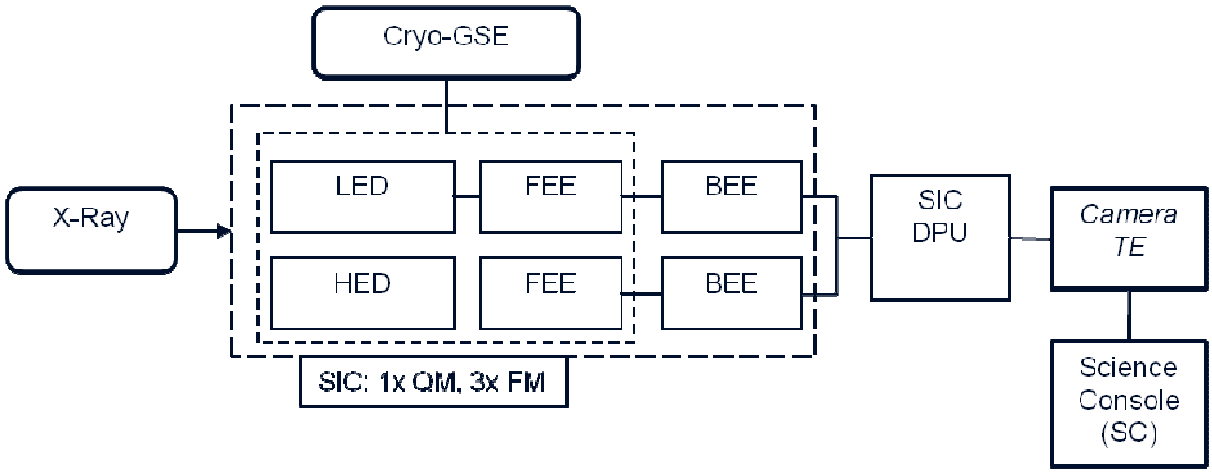

Figura 6-2: IC Test Configuration for AIT and Calibration at Camera Level

The Detector TE interfaces the detector either at the level of the FEE or at the level of BEE.

This TE provides the functionalities needed in order to gather, process and display image data from the detector, namely:

- Real time data acquisition, filing/archiving and quick look

- Commanding

The Camera TE is incorporates:

- the DPU functions;
- all the other functions needed in order to command and control the Detector Subsystem under test (LED/HED) and to gather the spectra, images and HK Data from the DPU, namely:
  - Real time data acquisition, filing/archiving
  - Near real time Quick Look of the HK data
  - Commanding

In addition, the Camera TE will buffer and forward in real time to the Science Console all the data acquired from the DPU. The buffer function will include the addition of a suitable header to the acquired data. The resulting pseudo TM packets of data will be sent to the Science Console through a TCP/IP connection established on the LAN.

This approach allows to limit the DPU TE to the commanding and HK data processing.

Additional functionalities required to support AIT and Calibration activities at Camera level will be provided by the Science Console, namely:

- Near real time data acquisition and archiving of the pseudo TM packets received from the Camera TE
- Near real time processing and quick look of the archived engineering and scientific data
- Off-line processing and quick look of the archived engineering and scientific data.

Unit Level activities on the DPU will be provided by the Payload EGSE described hereafter.

6.3 PIC GSE

The PIC test configuration at detector level and at camera level is depicted in Figure 6-3, and Figure 6-4, respectively.

The following GSE items are required:

- PIC Detector Test Equipment (TE)
- PIC Camera Test Equipment (TE).

The functionalities of the Test Equipment are similar to those presented above for the SIC.

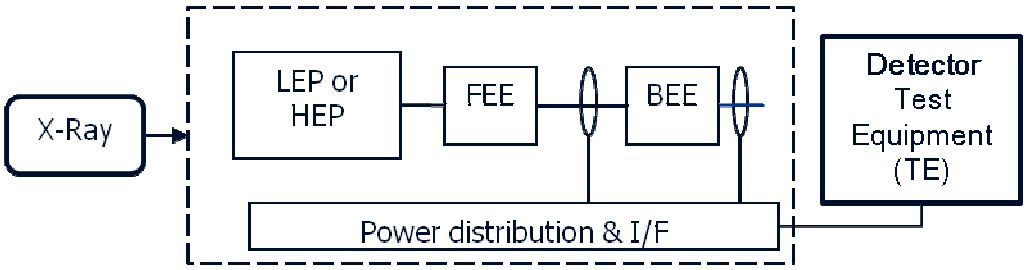

Figure 6-3: IC Test Configuration for AIT and Calibration at Detector Level

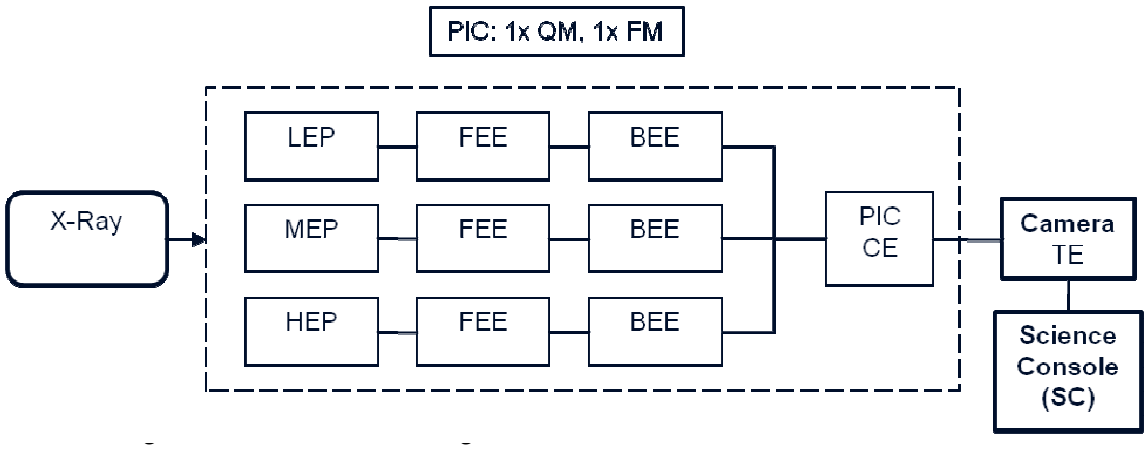

6.4 WFXRM GSE

The WFXRM test configuration at detector level and at camera level is depicted in Figure 6-5, and Figure 6-6, respectively.

The following GSE items are required:

- WFXRM Detector Test Equipment (TE)
- WFXRM Camera Test Equipment (TE).

The functionalities of the Test Equipment are similar to those presented above for the SIC.

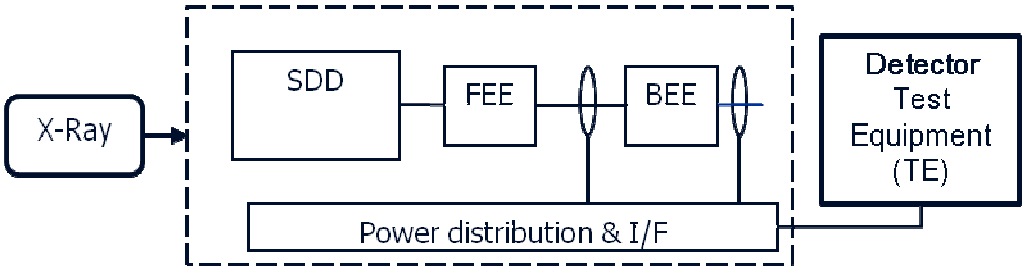

Figure 6-5: Test Configuration for AIT and Calibration at Detector Level

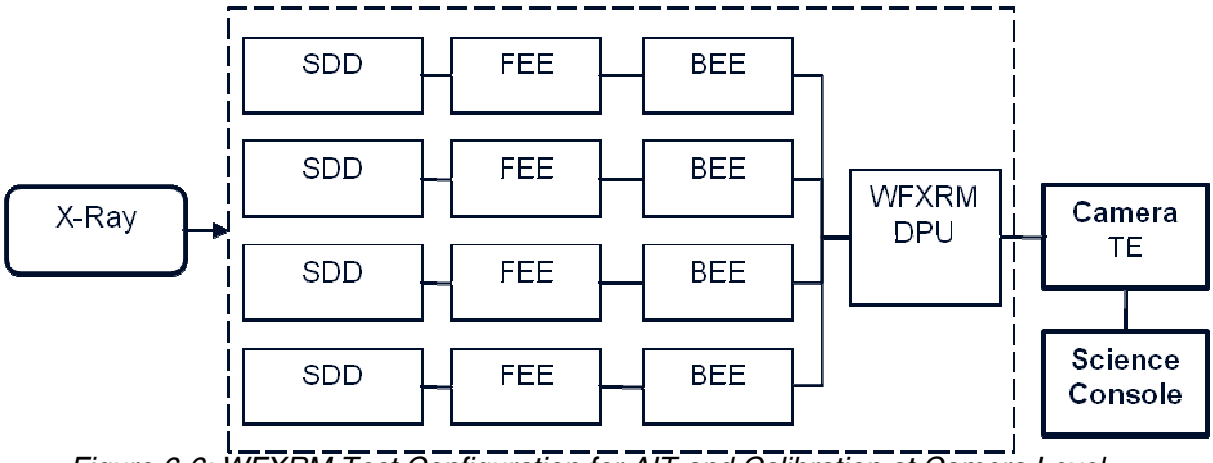

Figure 6-6: WFXRM Test Configuration for AIT and Calibration at Camera Level

6.5 Focal Plane Payload EGSE

As mentioned above, the Focal Plane Payload (FPP) EGSE will be exploited starting with the development and AIV activities of the SIC DPU and the PIC CE.

Hence, in conjunction with the Science Console, it will support all the AIV and Calibration activities at Focal Plane payload level.

As sketched in

Figure 6-7, the FPP EGSE will consist mainly of:

- Power SCOE
- Satellite Interface Simulator (SIS)
- Central Checkout Equipment (CCOE)

The Power SCOE will provide to the Payload the missing Spacecraft elements related to the electrical power supply.

The SIS will simulate the On Board Data Handling Bus. In near real time, it will:

- forward to the Payload the commands received from the CCOE
- forward to the Science Console the echo of the commands received from the CCOE
- forward to both the CCOE and to the Science Console the TM packets received from the Payload.

The CCOE will be the operator console which will:

- sequence the test operations by sending the Telecommand packets to the instrument
- archive all the Telemetry packets
- monitor the instrument HK data

Additional functionalities required to support the Payload level activities will be provided by the Science Console, namely:

- Near real time data acquisition and archiving of the pseudo TM packets received from the SIS
- Near real time processing and quick look of the archived engineering and scientific data
- On-line processing and quick look of the archived engineering and scientific data.

In some case (e.g. Calibration), additional computers shall be exploited to perform on-site some specific off-line scientific analysis.

Time to time, the Science Console shall transfer via Internet the data to a remote central archive from where the test data will be accessible to the rest of the NHXM collaboration for further analysis.

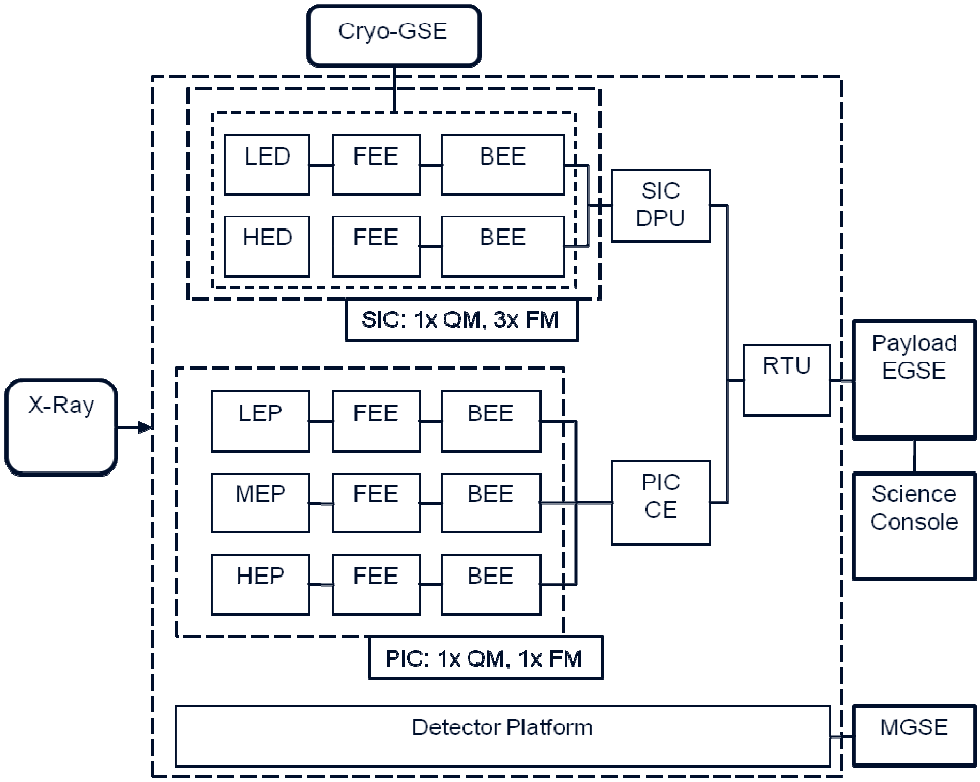

Figure 6-7 Test Configuration for Focal Plane AIT and Calibration

6.6 Science Console concept

The Test Equipment and in the EGSE presented envisage the use of a workstations named Science Console devoted to the archive, the pre-processing, and the quick look of the instrument data.

The proposed design concept foresees a common design for the Science Console, thus allowing the developing and testing of its software components since the early stages of the instrument development: first, it is exploited at camera level, then at payload level, and at satellite level. Eventually it could be reused also in the Ground Segment to support the Commissioning and the Performance Verification phases. Part of the Science Console s/w modules could also be reused in the pre-processing pipelines (L0 and L1 archiving) running in the Ground Segment.

The Science Console provides all the s/w tools required to perform, either in near real time or off-line, the archiving, processing, quick-look and analysis of the instrument data, with particular regards to the science data contained in the Science TM packets. It is assumed that, according to the mentioned ESA standard, each Source Packet consists of a Packet Header, a Data Field Header, a Data Field, and a trailing error control field. The Packet Header contains application identification (APID), sequence control and length information. The Data Field is the basic data unit and contains a meaningful quantity of related measurements. Its layout is identified by the Type/Subtype fields contained in the Data Field header.

The Engineering TM layouts are devoted to command receipt status information, housekeeping and diagnostic data reporting. These layouts are very simple structures of fixed length. Each raw value within the Data Field is easily identified by the bits and bytes offsets, and by its length in bits. The Science TM layouts foresee more complex variable length structures and compressed data format in order to minimize the TM bandwidth.

As sketched in Figure 6-8, the Science Console architecture foresees three main tasks: the Level 0 (L0) Archiving, the Level 1 (L1) Archiving, the Quick Look (QL).

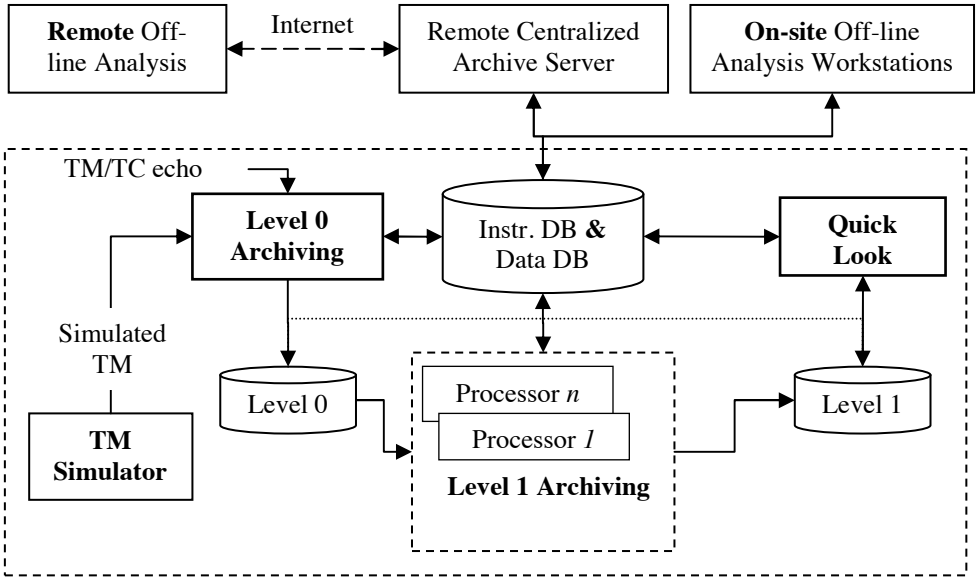

Figure 6-8: Science Console Design concept

The L0 Archiving task is in charge of interfacing the SIS to acquire and store, in near-real time, the raw TM and TC packets. The L0 archive is organized by measurement. The IWS exploits the Enter Observation / Enter Idle TCs to set automatically the L0 file boundaries. The incoming packets of the current measurement are checked to verify the Source Sequence Counter (SSC) for missing or out-of-sequence packets, and the Cyclic Redundancy Check (CRC) for quality assessment. The verification results are recorded in a log DB table together with the APID/Type/SubType packet statistics.

The L1 Archiving task, in near real time, sorts the packets by APID/Type/SubType and makes them available to the Processors modules. Each Processor module is aimed at decoding and archiving in one FITS file all the input Source packets identified by a specific combination of the APID/Type/SubType parameters. It extracts from each packet the individual fields and writes them into the corresponding L1 FITS file.

Each Processor is highly configurable. The module parameters and the main configuration file define all environment dependencies and address configuration files that describe the supported TM layouts. The recursive structure of the complex layouts is specified by a hierarchy of ASCII configuration files, one for each block composing the layout. The simple layouts require only the basic configuration file describing each field in terms of label, bit offset, bit length. These configuration files, that in some case specify hundreds of TM parameters, are generated automatically from the Instrument Data Base tables.

The Level-1 (L1) Archiving task interfaces the L0 Archive. For each L0 file it creates a set of FITS L1 files. These files are accessed by the Quick Look (QL) task to provide either in near real time or in playback mode a comprehensive and detailed view on the various data produced by the instrument components during the various levels of integration and calibration.

The Quick Look (QL) task involves both HK data and science data and is performed both in batch mode and interactively. HKs monitoring addresses instrumental health status and other auxiliary components performance.

The science data QL monitors primarily the detectors behaviour by performing spectral and images statistical analysis. The results of these analyses are stored in a DB log table that can then be used together with the HK data for cross check. Anomalies and not nominal values are detected automatically producing a feedback to the operator and rising flags in the QL log table. The QL component also includes a graphical user interface accessible from the web.

Finally, it is worth noticing that the proposed design concept allows implementing the instrument calibration flow concept depicted in

Figure 6-9.

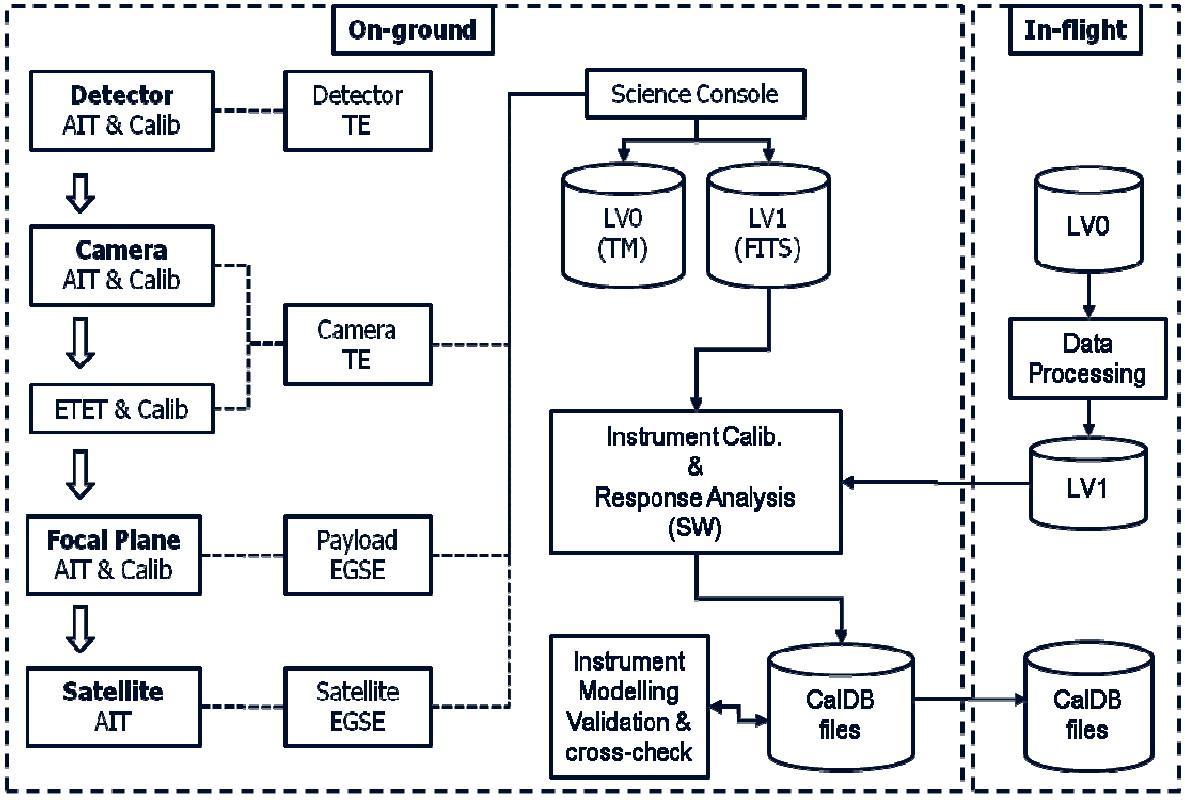

Figure 6-9: Instrument calibration flow concept

6.7 MOGSE

The NHXM Mechanical and Optical GSE (MOGSE) will be include:

- the reusable instrument and EGSE transport containers required for the Payload AIV, included the delivery to the NHXM satellite Contractor premises;
- the mechanical items required in order to handle the instrument during the level unit and subsystem level AIV, included the specific jigs (e.g.: lifting devices) to be delivered to the NHXM satellite Contractor premises to support the Payload AIV at satellite level.
- the calibration Jig GSE required for the calibration with the pencil beam setup.

6.7.1 Calibration Jig GSE

The scope of the jig is the calibration with the pencil beam setup of the prototype of NHXM (TDM3, Telescope Demonstrator Module 3, developed by Medialario) and of the final mirror module with some interface modifications. With the pencil beam the parabolic surface will be tested for >90%, while with the fully illumination setup the parabolic surface is tested only for 50%. The distance of the telescope from the detector

will be around 10 m and therefore the position of the jig and the optics will be in the zone between the main vacuum chamber of the PANTER facility and the tube with a diameter of 1m that link the X-ray source with the chamber. The same guide structure used so far for the previous prototype of NHXM will be used for the positioning. The interface structure of the jig should be the same of the jig used for the fully illumination.

The divergence of the X-ray beam is defined from the aperture that will be adopted. The alignment of the telescope will be performed with 2 tilts.

It has been verified that only 2 window are needed for the TDM2 to test 94% of the parabolic surface. A radial width of 55 mm will be able to measure the S297 and the shell S350. The second window will be narrow and it will be used to measure alone the 100% of the innermost shell (S185). The possibility to measure separately the three shells remains open and that means that a third aperture should be machined in the window mask. The amplitude in the azimuthal direction is fixed at 40°: the loss of area due to the aperture in this direction is 4% only in the two points that are far from the symmetry plane of the aperture.

For the final mirror module of NHXM 3 windows are needed considering a minimum diameter of 150mm and a maximum diameter of 390 mm. Also in this case the azimutal aperture should be 40°.

A mask minimizing the movements has been studied. In particular, a rotating mask has been designed. The possible configuration with this rotation will be:

- Obscuration of the whole telescope
- Direct beam configuration through a central hole of 15 mm.
- Selection of the first set of shells (for a azimuthal aperture of 40°)
- Selection of the second set of shell (for a azimuthal aperture of 40°)
- Selection of the third set of shell (for a azimuthal aperture of 40°)
- Selection of all the shells (for a azimuthal aperture of 40°).

These movements are realized by the rotation of a window mask along an axis that is shifted respect of the optical axis of the telescope and by a fixed mask (Figure 6-10).

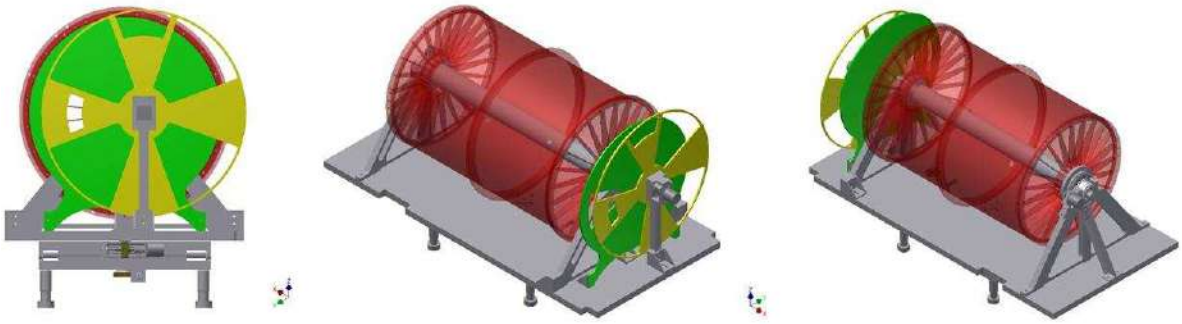

Figure 6-10: 3D model: mask for selecting the desired configuration (Yellow and green parts)

Besides this mask rotation other movements are:

- Tilt along X axis
- Tilt along Y axis
- Rotation of the telescope along its axis

The two tilts permit the alignment of the telescope, while the rotation of the telescope along its axis permits to measure the whole telescope. The image reconstruction will be realized by software over-imposing the single

detected images and correcting the telescope unpredictable movements with the use of 4 micrometric linear gages. The telescope is supported with a central shaft coupled with a gear and a step-to-step motor.

The two configurations for the supporting system are:

1. Support with 3 points on the external surface of the spiders
2. Couple with a central shaft

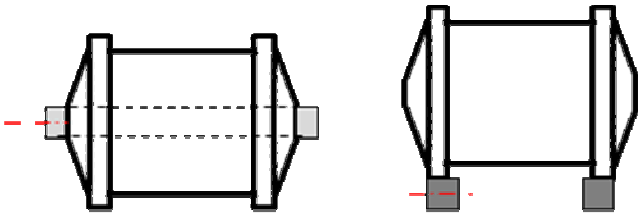

Figure6-11: Analyzed supporting configuration

A static FEM analysis has been performed to select the better choice that minimize the deformation (Figure 6-12).

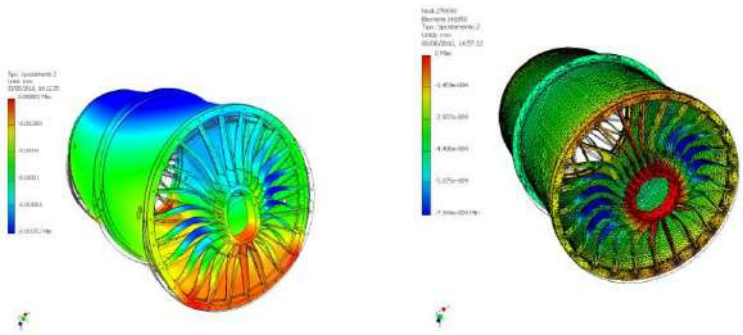

Figure 6-12: FEM analysis for the supporting system design

The support of the telescope is realized with a large lightening base to guarantee the stability of the mounting. (Figure 6-13). The entire jig mass is about 39 kg within the two stainless steel mask. All the mechanical parts have been mounted (Figure 6-14) and some details are presented hereafter in the sub-assembly figures (Figure 6-15).

The two stainless steel masks depend on the mirror shell that will be integrated in the prototype that will be manufactured just before the PANTER test campaign.

Figure 6-13: bottom view of the jig

Figure 6-14:assembled jig

Orizontal tilt
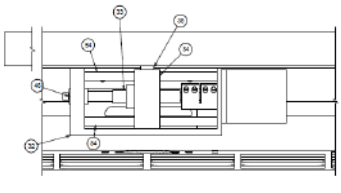 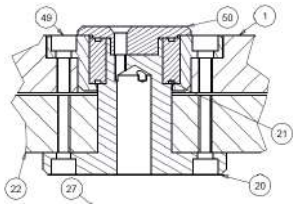 
Vertical tilt
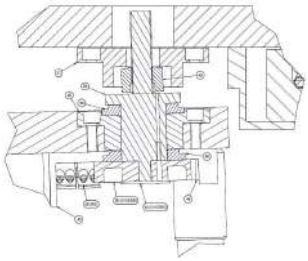 
Telescope rotation
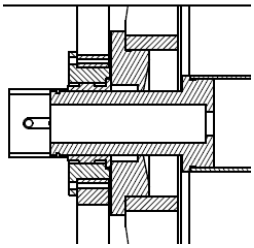 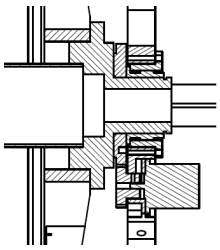 
Disk rotation
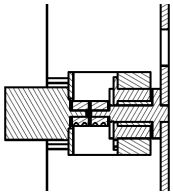 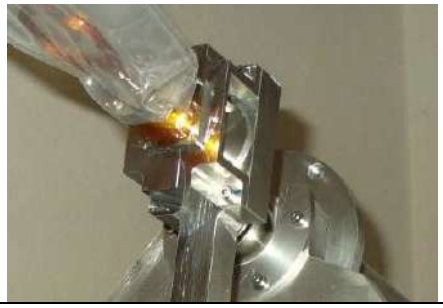

Figure 6-15: jig details

Besides the mechanical and transmission parts of the jig, the main electronic components (Figure 6-16) are:

- 4 step-step motors
- 4 proximity sensor
- 2 linear micrometers to record the two tilts for the alignment of the telescope.
- 2 zero sensor to record the zero position of the telescope and the window mask.

Figure 6-16: Some electronic components of the jig under test: linear encoder and proximity sensor are visible on the electronic box. The control is made by computer.

Respect the preliminary design the two angular encoder has been removed and replaced with two zero sensor because the step resolution of the stepper motor is enough to guarantee the knowledge of the position in the rotation of the telescope and the rotation of the mask. The 4 linear micrometers to record the position of the telescope during its rotation will be considered as a possibility, but they are not necessary in the vacuum chamber. The calibration of the telescope rotation can be done off-line not in the vacuum in the laboratory with only two heidenhain sensor (Figure 6-17).

Figure 6-17: Heidenhein sensor for the rotation calibration

A dedicated PANTER flange has been manufactured to make available a redundant number of connectors and pins in order to permit future improvements of the system (Figure 6-18).

Figure 6-18: PANTER flange with dedicated connectors

The geometrical constrains at PANTER facility has been also verified and the design is compliant with the detector movements of the PSPC and Tropic instruments that are currently available at PANTER. In fact the position of the focal spot according to the current design should be 27mm upward with respect to the axis of the tube of the PANTER facility and 14 mm (maximum) toward the “Pantolsky” side as shown in Figure 6-19.

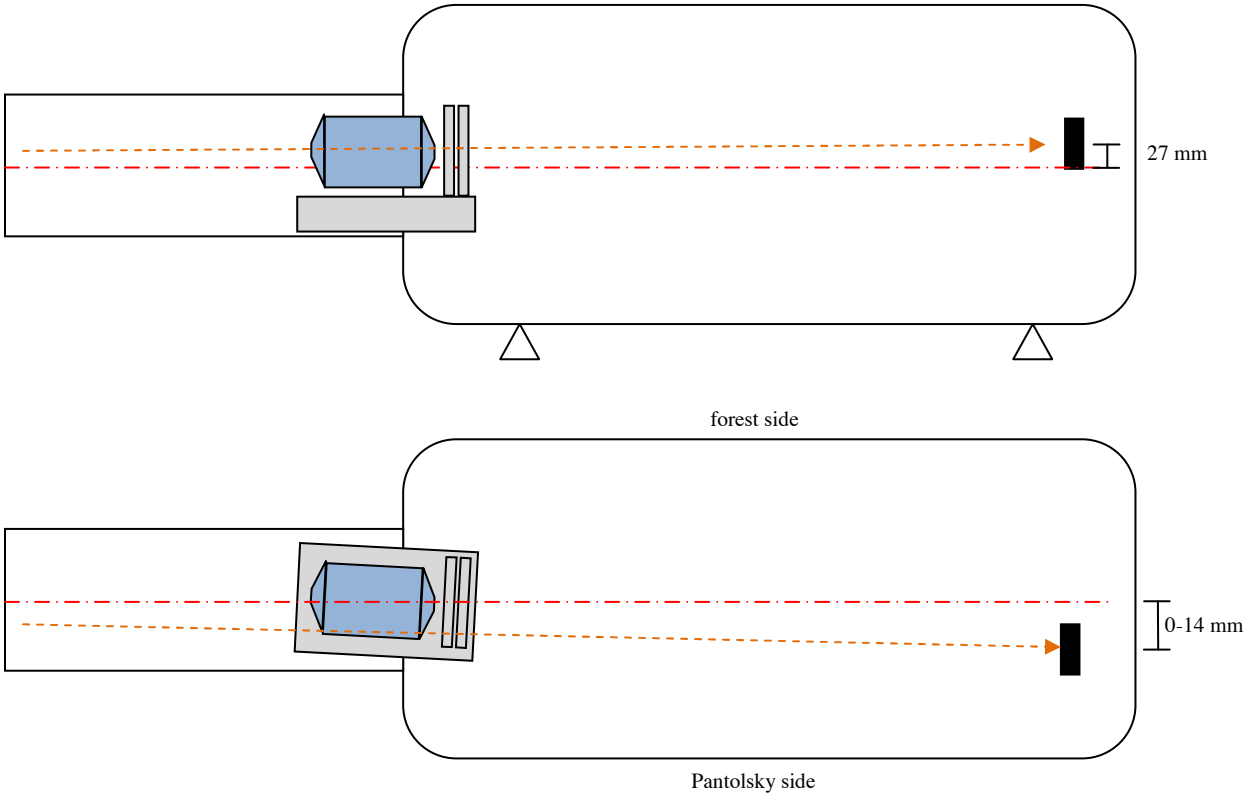

Figure 6-19: configuration of the jig at PANTER facility during the calibration of NHXM